nature synthesis

Supplementary information

https://doi.org/10.1038/s44160-026-01004-9

Click-locking strategy enables automated synthesis of single-atom catalysts with industrial compatibility

In the format provided by the authors and unedited

Table of Contents

Supplementary Methods

Photocatalytic CO_2 reduction reactions

The photocatalytic reduction of CO_2 was conducted in a 500 mL homemade gas-closed system, operating at ambient temperature and atmospheric pressure. For optimal performance, 50 mg of catalyst was dispersed on a petri dish and positioned within the reaction cell. A 300 W Xe-lamp (*Microsolar 300 Xenon lamp source*) was utilized as the primary light source. To ensure an effective reaction, the reactor was sealed and subjected to vacuum treatment, eliminating all air prior to light irradiation. The CO_2 and H_2O vapour were generated by combining 1.5 g of $NaHCO_3$ with 5.0 mL of a 4.0 M H_2SO_4 solution, introduced into the reactor post-vacuum treatment. Throughout the irradiation process, 2 mL gas samples were extracted from the reactor at one-hour intervals using a syringe, followed by analysis using a gas chromatograph (*GC-2030, Shimadzu Corp.*), equipped with a BID detector and a 5 Å molecular sieve column.

Photocatalytic H_2 evolution reactions

A Pyrex top irradiation reaction vessel was connected to a glass closed gas circulation system to measure photocatalytic hydrogen evolution. In a standard procedure, 30 mg of the photocatalyst was evenly dispersed in 30 mL of H_2O containing 10% vol triethanolamine (TEOA) as a sacrificial agent. This mixture was subjected to ultrasonication for 30 minutes to achieve a uniform dispersion. A 300 W Xe-lamp (*Microsolar 300 Xenon lamp source*) was employed as the light source, while the mixture was evacuated several times to remove any air prior to commencing irradiation. The resulting gas products were analyzed using a gas chromatograph (*GC-2030, Shimadzu Corp*) equipped with a TCD detector and a 5 Å molecular sieve column, ensuring precise and reliable measurements of hydrogen production.

Photocatalytic NO reduction reactions

The photocatalytic reduction of NO is a process conducted at room temperature utilizing a 300 W Xe lamp (*Microsolar 300 Xenon lamp source*), placed about 10 cm from the sample. By uniformly applying 0.1 g of photocatalyst onto a fiberglass membrane and positioning it within a Pyrex glass cell with a quartz window. To begin, high-purity NO gas is introduced at a flow rate of 25 mL min^{-1} for 30 minutes, purging any residual air. The subsequent activation of the ultrasonic

nebulizer produces aqueous microdroplets, paving the way for an efficient photocatalytic reaction once the light source is engaged. The resulting water-soluble product, NH_3, is collected and analyzed through ion chromatography via sample injection. Every hour, we withdraw 1 mL of reaction solution, filter out solid particles with a 0.22 μm filter, and dilute the resultant solution threefold to ensure accuracy. The concentration of NH_4^+ is monitored using ion chromatography (*Dionex Aquion, Thermo Scientific*).

CO oxidation activity evaluation

The catalytic activity for CO oxidation was evaluated in a fixed-bed quartz reactor system. A total of 100 mg of powdered catalyst was loaded into a quartz tube with an internal diameter of 10 mm. The feed gas, consisting of 0.5 vol.% CO and 12 vol.% O_2 balanced with high-purity N_2, was introduced at a total flow rate of 100 mL/min, corresponding to a weight hourly space velocity (WHSV) of 60,000 mL h^{-1} g_{cat}^{-1}. Reaction temperatures were systematically increased from 30 ℃ to 390 ℃ in 30 ℃ increments. Outlet gas concentrations of CO, CO_2, and O_2 were continuously monitored using a flue gas analyzer (*FGA10*). The CO conversion was calculated using the following equation:

$$\text{CO Conversion (\%)} = \frac{[CO]_{inlet} - [CO]_{outlet}}{[CO]_{inlet}} \times 100\% \quad (1)$$

Here, $[CO]_{inlet}$ and $[CO]_{outlet}$ represent the CO concentrations at the reactor inlet and outlet, respectively. To simulate realistic conditions, water vapor was introduced into the system via a temperature-controlled vapor generator, with the vapor stream blended uniformly with the feed gases in a mixing tank. The water vapor concentration was precisely maintained at 5 vol.% to evaluate the catalyst's performance and stability under humid conditions.

NO_x removal and NH_3 oxidation catalytic activity measurement

The catalytic performance for NH_3-SCR reactions, including activity and N_2 selectivity, was evaluated using a custom-designed fixed-bed reactor. Prepared catalyst powders were pressed into tablets, sieved to 60–100 mesh, and loaded into a reaction tube with an inner diameter of 8 mm. A thermocouple was inserted to monitor the reaction temperature, while gas concentrations were precisely controlled using flow meters. The feed gas contained 500 ppm NO, 500 ppm NH_3, 5 vol.%

O_2, 100 ppm SO_2 (when used) and 10 vol% H_2O (when used), and N_2 as the balance gas, with a gas hourly space velocity (GHSV) of 50,000 h^{-1}. Once steady-state conditions were achieved, inlet and outlet concentrations of NO, NO_2, N_2O, and NH_3 were measured using an infrared gas analyzer (*GASMET FTIR DX4000*). SCR performance was evaluated over a temperature range of 90–300 ℃, with NO conversion and N_2 selectivity calculated as follows:

$$\text{NO Conversion (\%)} = \frac{[NO_x]_{inlet} - [NO_x]_{outlet}}{[NO_x]_{inlet}} \times 100\% \quad (2)$$

$$NO_x = NO + NO_2 \quad (3)$$

$$\text{N}_2\text{ Selectivity (\%)} = 1 - \frac{2 \times [N_2O]_{outlet}}{[NO_x]_{inlet} + [NH_3]_{inlet} - [NO_x]_{outlet} - [NH_3]_{outlet}} \times 100\% \quad (4)$$

CO_2 thermal catalytic evaluation

The catalytic performance for CO_2 hydrogenation was evaluated in a high-pressure fixed-bed reactor. A specified amount of catalyst (40–60 mesh), with the exact sample mass and testing conditions detailed in the corresponding figure captions, was thoroughly mixed with 2 g of quartz sand (40-60 mesh, when applicable) and loaded into the reactor. Prior to testing, the catalyst underwent an in-situ activation process under a controlled hydrogen flow, with precise flow rates and temperatures provided in the captions, using a mass flow controller. This activation step was critical for removing surface impurities and stabilizing active sites. Following activation, the reactor temperature was adjusted to the designated reaction temperature, and a gas mixture of CO_2, H_2, and Ar, with specific flow rates also detailed in the captions, was introduced. The gas flow and reactor pressure were accurately controlled using mass flow controllers and a backpressure regulator. The effluent gases were continuously analyzed using an online gas chromatograph (*Agilent 8890*), equipped with a thermal conductivity detector (TCD) for non-hydrocarbon species (e.g., CO, H_2, CO_2) and a flame ionization detector (FID) with a methanizer for hydrocarbons and oxygenates, ensuring enhanced sensitivity. The CO_2 conversion rate and product selectivity for CH_3OH, CO, CH_4, and hydrocarbons were calculated based on gas chromatographic data using standard equations.

$$CO_2 \text{ Conversion (\%)} = \frac{CO_{2_{in}} - CO_{2_{out}}}{CO_{2_{in}}} \times 100\% \quad (5)$$

$$CO \text{ Selectivity (\%)} = \frac{CO_{out}}{CO_{2_{in}} - CO_{2_{out}}} \times 100\% \quad (6)$$

$$C_xH_\gamma \text{ Selectivity (\%)} = (1\text{-}S_{CO}) \times \frac{M_{C_xH_\gamma} \times x}{\sum_i \left(M_{C_xH_\gamma} + M_{C_i\ alcohol}\right)} \quad (7)$$

$$C_{i\ alcohol} \text{ Selectivity (\%)} = \frac{1\text{-}S_{CO}}{CO_{2_{in}} - CO_{2_{out}}} \times \frac{M_{C_i\ alcohol} \times i}{\sum_i \left(M_{C_i\ hydrocarbon} + M_{C_i\ alcohol}\right)} \quad (8)$$

Here, $CO_{2_{in}}$ represent the molar amounts of CO_2 in the feed and effluent, respectively. $CO_{2_{out}}$ indicates the molar amount of CO in the effluent. CO_{out} denotes selectivity toward CO in the effluent. S_{CO} denotes selectivity toward CO, while $M_{C_xH_\gamma}$ and $M_{C_i\ alcohol}$ represent the molar amounts of hydrocarbons and alcohols with x carbon atoms, respectively.

LCA & TEA methods

We performed a comprehensive LCA to systematically evaluate the environmental impacts of the Cu_1/CeO_2-(111)-L catalyst ("L" denotes large-scale synthesis) specifically designed for selective catalytic reduction of NO_x with NH_3 (NH_3-SCR). Comparisons were made against commercially available NH_3-SCR V–W–Ti catalysts, using 1 kg of active catalyst as the functional unit. We applied the CML baseline (2020) methodology[1] and adhered to the four distinct phases outlined in ISO 14040/14044 standards: goal and scope definition, inventory analysis, impact assessment, and interpretation[2]. We utilized *eChemstore® Intelligence* software to perform the analysis, incorporating activity and emission factor data from experimental results, scholarly literature, and the ecoinvent 3.9 database. For materials not cataloged in the ecoinvent 3.9 database, we retraced their preparation processes to identify raw materials that could be mapped within the database. By systematically integrating these data sources, we ensured the assessment's accuracy and provided a reliable comparison of the catalysts' environmental profiles.

The economic feasibility of Cu_1/CeO_2-(111)-L catalyst production for the NH_3-SCR was assessed through an annuity-based TEA[3] benchmarked against commercially available V–W–Ti catalysts. This assessment assumes an annual catalyst production capacity of 800 tons

(approximately 0.1 ton per hour of active catalyst) and incorporates a comprehensive evaluation of material and energy flows throughout the entire synthesis process. The overall system cost comprises capital expenditures (including equipment acquisition, construction, and contingency costs) and operational expenses (including labor, maintenance, materials, utilities, and administrative overheads). The cost-analysis framework applied here adheres to established methodologies reported in the literature[4,5].

Supplementary Notes

Supplementary Note 1: Criteria for the Clicking Single Atom Catalysts.

1.Click Driving Force: A high driving force, inherent in click chemistry, ensures the formation of functionally irreversible bonds between single atoms and supports. This prevents agglomeration and deactivation, particularly under catalytic conditions.

2. High-Throughput Synthesis: The synthesis process must be amenable to automation, enabling high-throughput production within short timeframes to accelerate discovery.

3.Scalability: The synthesis process must be straightforward and scalable to kilogram levels.

4.Cost-Effective Materials: The process should rely on readily available, inexpensive materials, such as inert oxides and metal salts, to ensure economic feasibility.

Supplementary Note 2: Evidence for enhanced metal anchoring via VC-to-CeO_2 electron transfer

Initially, vitamin C (VC) absorb onto the CeO_2 surface, donating electrons and consequently transforming into its oxidized form (dehydroascorbic acid, DHA). Afterward, we thoroughly wash the CeO_2 to completely remove any residual VC and DHA. Only following this washing step are metal ions (such as copper ions) introduced.

We further evaluated the effect of electron transfer on metal ions anchoring using additional computational and experimental approaches (**Fig. S12**). Individual VC molecules have limited affinity for Cu^{2+} ions due to significant solvation energy and the requirement to break stable C-O bonds (**Fig. S12a**). Conversely, pristine CeO_2 offers favorable adsorption sites through its three-coordinated oxygen atoms, forming Cu-O interactions. When CeO_2 is electron-enriched through VC treatment, its enhanced negative surface charge significantly strengthens Cu^{2+} adsorption (E_{ads} = –3.82 eV, **Fig. S12c**), attributed to intensified electrostatic interactions and improved orbital hybridization. Experimental validation via inductively coupled plasma-optical emission spectroscopy (ICP-OES) corroborated these computational findings. Without VC modification, Cu loading on Cu_x/CeO_2-2 was merely 0.82 wt%. However, CeO_2 modified by VC (Cu_1/CeO_2-(111) catalyst) exhibited Cu loading as high as 4.31 wt%, highlighting the substantial positive effect of electron transfer on metal ion anchoring.

Supplementary Note 3: Why anchoring single atoms on the inert CeO_2-(111) facet is challenging?

As shown in **Fig. S14**, Cu^{2+} is two-coordinated with a nonlinear ML_2 configuration, deviated from $D_{\infty h}$ symmetry to C_{2v}, under which Cu 3d 4s orbitals split into $3A_1+A_2+2B_1$ in terms of the symmetry. To obtain stable Cu-SAC, Cu^{2+} needs to be reduced with external electrons filling into empty valence orbitals $3d^94s^0$. Following such analysis, d_{z^2}, $d_{x^2-y^2}$ and 4s have been identified to interact with A_1-symmetry symmetry-adapted linear combinations (SALCs) based on symmetry-matching principle when Cu^{2+} is adsorbed on (110)/(100) surface, as shown in **Fig. S15**–**16**. However, such interaction is not approachable on (111) surface. As shown in **Fig. S17,** Cu is three coordinated and presented as ML_3 crystal field. For Cu^{2+}, d_{z^2} orbital along the z-axis is of A1 symmetry, which may interact with A_1-SALC, but the overlap should be small due to Cu outward movement. The other four d-orbitals split into two doubly degenerated groups (E'+E"), including $d_{x^2-y^2}$&d_{xy} set and d_{xz} &d_{yz} set, respectively. As illustrated in **Fig. S22**, Cu 4s atomic orbital presents a high energy level; as a result, MO associated with Cu 4s-L(A_1) is overwhelmingly dominated by O 2p ligands. Although d_{z^2} also shows A_1 symmetry and presents a smaller gap with O 2p, it can hardly overlap with L(A_1) due to structural deviation.

Based on the analysis of Cu orbitals and O-ligands SALC, symmetry-matched combinations have been identified to generate molecular orbitals for Cu/CeO_2 (100) surface (Cu/S100) or Cu/CeO_2 (110) surface (Cu/S110) in **Fig. S18** and Cu/CeO_2-(111) surface (Cu/S111) in **Fig. S19**, from which three features can be summarized: (i) more Cu orbitals can effectively interact with O-ligands on S100 and S110 than that on S111; (ii) both Cu 3d and Cu 4s have been involved in Cu-O σ-bonding, with bonding MOs dominated by O-ligands; (iii) electron transfer from O 2p to empty Cu 4s is critical for Cu 4s-O 2p bonding. Clearly, effective filling into these bonding states directly affect the adsorption of Cu ions; as a result, negatively charged surfaces can offer stronger adsorption capacity than neutral one, as demonstrated above. Such acceptance of external electrons is beneficial for the full filling of bonding MOs associated with Cu_{4s}-O_{2p} and $Cu_{3d_{x^2-y^2}}$-O_{2p}, as illustrated in **Fig. S20** for Cu/S111.

In terms of symmetry matching, several atomic orbitals from Cu^{2+}, such as $3d_{z^2}$, $3d_{x^2-y^2}$ and 4s, can interact with ligands SALCs; however, the interaction has also been affected by the effective orbital overlap. For all three surfaces of study, d_{z^2} can match well with ligand SALCs with a

symmetry A_1, but the overlap can be different, as determined by the distance and orientation of Cu-O pairs. For ideal linear ML_2 or planar ML_3 crystal field, d_{z^2}-L(A_1) can achieve the maximum overlap, while Cu-adsorption shows slight deviation from such ideal case due to outward movement, which can be indicated by the parameter d, as shown in **Fig. S13a** and **b** for Cu/S111 and in **Fig. S21** for Cu/S110 and Cu/S100. For S110 and S100, the deviation from ideal ML_2 is small and does not generate strong impact on the bonding between $d_{x^2-y^2}$ and L(π), as illustrated in **Fig. S21a**–**c**. Specifically, calculated d for Cu/S110 (0.15 Å) and for Cu/S100 (0.37 Å) is notably smaller than that for Cu/S111 (0.78 Å). In **Fig. S13a** and **b**, the effect of large deviation d on Cu-O bonding has been illustrated, as supported by calculated large Cu-O bond length b. As a result, d_{z^2} and $d_{x^2-y^2}$ orbitals, with a symmetry of E' and E", can hardly overlap with the ligands SALCs, as shown in **Fig. S21d**–**f and Fig. S13c** and **d**. Such poor adsorption by (111), however, can be mediated with electron-donating agents. In fact, the deviation *d* has been remarkably reduced from 0.78 Å to 0.42 Å after VC adsorption (see **Fig. S13b** and **f**), indicating that Cu adsorption on the electron-rich S111 surface has been strengthened. Associated with smaller deviation d, the overlap between Cu 3d and O 2p orbitals has been improved, particularly for d_{z^2} and $d_{x^2-y^2}$ as shown in **Fig. S13g** and **h.**

Supplementary Note 4: Characterization of the Cu_1/CeO_2-(111) C-SACs

In order to study whether there is Cu-related phase formation, Rietveld refinement was first performed on the X-ray diffraction (XRD) spectra of CeO_2 support, CeO_2-(111)-VC and Cu-doped CeO_2 catalysts, as shown in **Fig. S7**. In the XRD spectra of Cu-doped CeO_2, only the diffraction peak of cubic fluorite structure CeO_2 appeared, and no other diffraction peaks were found, indicating that there was no formation of nanoparticles related to Cu. **Table S2** shows the grain size, unit cell parameters and microstructure parameters of each catalyst. For the Cu_1/CeO_2-(111) C-SACs, no severe lattice distortion was found, which ruled out the formation of Cu-Ce solid solution and the formation of Cu-doped CeO_2. In contrast, the unit cell parameters of the Cu-doped CeO_2 catalyst synthesized are significantly reduced, which is due to the shrinkage of the unit cell caused by the doping of Cu in the CeO_2 bulk phase.

In both bright-field Transmission electron microscopy (TEM) and high-resolution TEM images, Cu_1/CeO_2-(111) C-SACs appeared to be indistinguishable from pristine CeO_2, and no Cu-related nanoclusters or nanoparticles were observed (**Fig. S23a** and **b**). Combined with the XRD characterization results, Cu_1/CeO_2-(111) C-SACs maintain the structure of cubic fluorite ceria and no new peaks appear, which indicates that Cu is highly dispersed on the surface of CeO_2. Higher resolution high angle annular dark field-scanning transmission electron microscopy (HAADF-STEM) images do not reveal nanoclusters or particles of Cu species. As shown in **Fig. S23c**, in the orderly array of atoms, spots with higher brightness appear randomly. These brighter spots may be Cu atoms loaded on the surface. The energy dispersive X-ray spectroscopy (EDS) element distribution map also confirmed the uniform distribution of Cu and Ce elements (**Fig. S23d**–**g**).

Supplementary Note 5: Ruling out direct Cu–VC coordination and M–N–C-type SAC formation

To explicitly address and experimentally rule out the possibility of direct coordination between metal ions and VC, we performed additional control experiments. Specifically, we directly mixed VC with copper nitrate solution (without the presence of CeO_2) to prepare a copper–VC complex (Cu-VC). Extended X-ray absorption fine structure (EXAFS) spectroscopy provided clear experimental evidence (**Fig. S25**). For the Cu_1/CeO_2-(111) catalyst, EXAFS spectra confirmed the atomic dispersion of copper atoms, showing no Cu–Cu scattering paths. In contrast, the Cu-VC samples exhibited pronounced peaks at approximately 2.1-2.5 Å, indicative of metal–metal coordination resembling metallic copper foil[6-8]. These observations demonstrate unequivocally that although VC molecules contain hydroxyl groups capable of coordination, isolated VC alone cannot stabilize copper in the single-atom form. Instead, direct coordination between VC and copper ions leads to cluster or particle formation.

To explicitly address and experimentally rule out the possibility of forming metal oxide-supported M–N–C type single-atom catalysts (SACs), we constructed theoretical models representing metal oxide-supported M–N–C structures and simulated their corresponding X-ray absorption near edge structure (XANES) spectra via first-principles calculations (**Fig. S26**). Clearly, the simulated XANES spectrum of this hypothetical metal oxide-supported M–N–C catalyst configuration significantly deviates from our experimental data for Cu_1/CeO_2-(111). This unambiguously excludes the possibility that our synthesized catalysts resemble metal oxide-supported M–N–C SACs.

Supplementary Note 6: Batch-to-Batch consistency of the robotic system

We conducted ten independent batch syntheses of two representative electrode-based catalysts—Pt_1/CeO_2-VC@NF-80 and CeO_2-VC@NF. All batches were evaluated using our automated high-throughput electrochemical platform at –100 mA cm^{-2} for hydrogen evolution reaction (HER), with the results presented in **Fig. S35**. The corresponding statistical results are now explicitly summarized in **Table S4**. For Pt_1/CeO_2-VC@NF-80, the average overpotential was 101.1 mV, with a standard deviation of 3.2 mV and a relative standard deviation (RSD) of 3.2%, across a range of 97.4–106.6 mV, indicating all batches fell within a narrow ±5 mV window. For CeO_2-VC@NF, the average overpotential was 432.1 mV, with a standard deviation of 3.9 mV and an RSD of 0.89%, across a span of 423.9–439.2 mV. This confirms excellent reproducibility. The low variation further confirms the high reproducibility achieved through our robotic platform.

Supplementary Note 7: Mechanistic Analysis of the Urea Oxidation Reaction (UOR)

Density functional theory (DFT) simulations were conducted to elucidate the mechanism of UOR on Ni_1/CeO_2, providing comprehensive thermodynamic insights into the reaction pathway. The computed free energy changes and corresponding intermediate structures are illustrated in **Fig. S37**. The complete UOR mechanism involves nine sequential steps: urea initially adsorbs onto the Ni single-atom site on CeO_2 with an adsorption energy of 0.25 eV, followed by the first hydrogen desorption to form $^*CONHNH_2$ (energy barrier: 1.23 eV). The rate-determining step (RDS) occurs at the second deprotonation, converting $^*CONHNH_2$ to $^*CONHNH$ with an energy barrier of 2.18 eV. Subsequent deprotonation steps yield $^*CONHN$ (barrier: 1.27 eV) and then $^*CONN$ (barrier: 0.77 eV). The $^*CONN$ intermediate spontaneously releases nitrogen to yield $^*CO$, which is subsequently converted to $^*COOH$ (barrier: 1.15 eV), followed by transformation into $^*COO$. Finally, spontaneous CO_2 desorption completes the UOR process.

To facilitate comparative analysis, additional DFT calculations were performed for UOR pathways on pristine CeO_2 and the commercial noble-metal catalyst RuO_2. For CeO_2, the RDS occurs at the initial hydrogen desorption step ($^*CO(NH_2)_2 \rightarrow ^*CONHNH_2$), requiring a high energy barrier of 3.32 eV. In contrast, for RuO_2, the RDS occurs at the third hydrogen desorption step. Remarkably, the introduction of Ni single atoms significantly alters the UOR mechanism on CeO_2, shifting the RDS to the second hydrogen desorption step ($^*CONHNH_2 \rightarrow ^*CONHNH$) and substantially reducing the barrier to 2.18 eV, closely approaching RuO_2 (2.15 eV).

Supplementary Note 8: The details of the computational screening process

For the purpose of element screening, we selected 18 readily available, inexpensive, and non-toxic metal elements as single atoms on the CeO_2 surface, as shown in **Fig. 5a**. In order to rationally construct CeO_2-based C-SACs, DFT calculations are initially used to predict the most stable structure of M_1/CeO_2 and to identify the optimal anchor sites for the single metal atoms. The construction of the CeO_2-(111) surface is illustrated in **Fig. S41**. To ascertain the optimal configuration, we examined the anchoring of these single atoms onto the CeO_2 surface, exploring different possible surface sites for binding the metal atoms and determining the most stable arrangement (**Fig. S42**).

Utilizing the above-mentioned most stable structures, we assessed the thermodynamic stability of these single metal atoms on CeO_2 substrates, as it is a prerequisite for their practical application as efficient selective catalytic reduction (SCR) catalysts. This is achieved by strong binding between the metal atoms and the CeO_2 support to prevent their aggregation. Our results suggest that their binding energies ranged from 0.6076 eV to −6.174 eV (**Fig. S43**), where a negative binding energy indicates an exothermic process of the binding of the metal atom onto the CeO_2 surface. Based on this analysis, we excluded two elements, including K and Na, for SACs due to their observed instability. We designed our catalyst to screen for common pollutant removal reactions (e.g., CO, NH_3, NO). Our previous research indicated that the catalytic performance was predominantly limited by NH_3 adsorption and O_2 activation on its surface. Therefore, we identified NH_3 adsorption and the O_2 activation ability of the C-SACs as two crucial criteria for screening single-atom elements. We calculated the NH_3 adsorption energies for each single-atom system to indicate the activation capacity for NH_3, as depicted on the vertical axis of panel (A) in **Fig. 5a**. Additionally, we determined the –ICOHP value of the O_2 dimer adsorbed on the oxygen vacancies of these single-atom systems, serving as a measure of the degree of activation towards O_2 dimers, as shown on the horizontal axis of panel (B) in **Fig. 5a**. In the figure, a position closer to the lower right corner represents a single-atom catalyst with improved NH_3 adsorption and oxygen activation capabilities. Consequently, the Cu_1/CeO_2 C-SACs was selected for large-scale synthesis, detailed characterization, and performance evaluation in NO_x/CO removal.

Supplementary Note 9: Proposed CO oxidation catalytic mechanism

The main mechanisms proposed for CO oxidation are the Langmuir-Hinshelwood (L-H) mechanism and the Mars-van Krevelen-type (M-vK) mechanism. The L-H mechanism considers the reaction between adsorbed CO and adsorbed O_2 on the surface of the catalyst to form CO_2, and is commonly used to explore CO oxidation on single-crystal noble metal catalysts, such as Au, Pt, Pd, Rh, and Ir, while M-vK mechanism can be the interpretation of CO oxidation reaction over metal oxide catalysts, with the participation of lattice oxygen. Thus, we adopted the CO oxidation via the M-vK mechanism for the Cu_1/CeO_2 catalyst.

DFT simulations are used to further explore the CO oxidation reaction mechanism on the Cu_1/CeO_2-(110) surface and Cu_1/CeO_2-(111) surface, providing both thermodynamic and kinetic information regarding the reaction pathway. The free energy change of the CO_2 formation reaction pathway on the Cu_1/CeO_2-(110) surface and the corresponding structures of the intermediates and transition states are shown in **Fig. S44a**. Step 1: CO molecule was adsorbed on the Cu single atom at CeO_2-(110) with the adsorption energy of −1.20 eV. Step 2: one adjacent lattice oxygen was drawn to the first CO molecule, leading to an adsorbed bent CO_2 species formation with a barrier energy of 0.90 eV. Step 3: the desorption energy of CO_2 is discovered to be 1.44 eV, accompanying two Ce^{4+} transformed into Ce^{3+} and simultaneously O vacancy formed, which is the rate-limiting step of the whole reaction path. Step 4: after CO_2 desorption, the formed oxygen vacancy sites can be strongly filled up by O_2 molecules with the relatively high adsorption energy of −1.95 eV. Meanwhile, the second CO molecule can be co-adsorbed on the Cu atom with an adsorption energy of −0.81 eV. Step 5: following the adsorption, the CO species reacts with one O atom from adsorbed O species, which drives the desorption of CO_2 molecule and regeneration of the single-atom catalyst, overcoming a relatively low barrier of 0.10 eV.

Similarly, CO oxidation at Cu_1/CeO_2-(111) also follows the M-vK mechanism. **Fig. S44b** exhibited the free energy change of the CO_2 formation reaction pathway and the corresponding structures of the intermediates and transition states. The CO molecule adsorbs on the Cu single atom with an adsorption energy of −1.69 eV, indicating for Cu_1/CeO_2-(111) CO molecule is adsorbed strongly compared to Cu_1/CeO_2-(110). The rate-limiting step is the desorption of first CO_2, requiring the high energy barrier of 1.15 eV. The interaction between CO and Cu is the weaker and the CO adsorbate is more likely to activate the subsurface oxygen on the CeO_2-(110) surface.

Supplementary Note 10: Proposed SCR catalytic mechanism

Given the coexistence of three different reactants: NH_3, NO, and O_2, in the NH_3-SCR reaction, the adsorption behavior of these unimolecular gases on the catalyst surface is studied. The structural model of the Cu_1/CeO_2-(111) C-SACs used for adsorption and reaction simulations is shown in **Fig. S46**. In this study, multiple configurations and adsorption sites of a single molecule on the Cu_1/CeO_2 C-SAC surface is explored, and the most stable adsorption structure is determined based on the principle of minimum energy. **Fig. S47** depicts the most stable adsorption configuration of reactant molecules (NH_3, NO, and O_2) on the Cu_1/CeO_2-(111) surface. The calculated adsorption configuration reveals that O_2 molecules exhibited a greater tendency to chemisorb and activate in the end-bridge mode on isolated Cu sites. This observation is reasonable because O_2, with its lower $2\pi^*$ orbital energy, acts as an electron acceptor and is more likely to adsorb on the electron-rich Cu single atom. The adsorption energy of O_2 is measured to be –0.6 eV, while the adsorption energy of O_2 on the pure CeO_2 surface is only –0.01 eV, indicating the enhancement of the adsorption strength of O_2 using Cu single atom. In addition, the presence of Cu single atoms enhances the adsorption strength of NH_3 molecules, as evidenced by adsorption energy of –0.91 eV on Cu single atom sites, in contrast to only 0.06 eV on the CeO_2-(111) surface, as shown in **Fig. S48**. Moreover, the computational results also show that NO adsorption on the Cu_1/CeO_2-(111) surface is endothermic, with an energy of 0.56 eV, while it could not achieve stable adsorption on the CeO_2-(111) surface. Therefore, the presence of Cu single atoms enhanced the adsorption strength of the three reactant molecules on the catalyst surface. Notably, the adsorption of NH_3 on Cu single atoms is thermodynamically more favorable than that of NO/O_2 (−0.91 eV for NH_3 and –0.56/–0.60 eV for NO/O_2). In the typical calculation of the SCR reaction mechanism of Cu_1/CeO_2, the chemical adsorption of NH_3 is considered the first step of the reaction. The single atomic site on the surface of Cu_1/CeO_2-(111) adsorbs and activates NH_3, simultaneously activating the activity of lattice oxygen in the vicinity of the Cu site. This dual activation further causes the efficient dehydrogenation of NH_3, as obtained in the subsequent calculation of the reaction pathway.

The oxygen vacancy formation energy is a measure of the external energy required to create an oxygen vacancy, whereby a lower value implies the easier formation of oxygen vacancies within the system. In the case of the Cu_1/CeO_2-(111) surface, various oxygen positions were first considered to select the most stable site for oxygen vacancy generation. Furthermore, the

calculation findings showed that the most stable oxygen vacancy formation site was identified as the next nearest neighbor lattice oxygen site to the Cu single atom, as depicted in **Fig. S49c**. The oxygen vacancy formation energy at this site was measured to be 2.64 eV, which was lower than that on the pure CeO_2-(111) surface (2.88 eV). Hence, the support of Cu single atoms also facilitated the formation of surface oxygen vacancies.

DFT simulations are used to thoroughly explore the SCR reaction mechanism on the Cu_1/CeO_2-(111) surface, providing both thermodynamic and kinetic information regarding the reaction pathway. Additionally, these simulations aimed to confirm whether the construction of Cu single atoms can effectively surmount the thermodynamic and kinetic constraints associated with the surface SCR reaction pathway of pure CeO_2. Considering the NH_3 adsorption at the Cu sites on the Cu_1/CeO_2-(111) surface prior to NO, we focused on investigating the dehydrogenation process of NH_3 on the Cu_1/CeO_2-(111) surface at 500 K, starting from the stable adsorption configuration of NH_3. As presented in **Fig. S50**, the NH_3 molecule underwent direct decomposition, wherein one of the N-H bonds in the NH_3 molecule is broken, and the hydrogen atom migrates towards the oxygen atom surrounding the Cu atom, forming a hydroxyl group while leaving behind an $^*NH_2$ group. The computed reaction free energy change for NH_3 activation ($NH_3^* \rightarrow NH_2^*/H^*$) is determined to be 0.4 eV, signifying the lowest kinetic barrier of 0.95 eV. Thus, it is evident that not only does NH_3 exhibit higher adsorption strength on the Cu_1/CeO_2-(111) surface compared to the CeO_2-(111) surface (-0.61 eV vs. 0.06 eV), but the kinetic barrier for NH_3 activation on the Cu_1/CeO_2-(111) surface is also lower than that on the CeO_2-(111) surface (0.58 eV vs. 0.95 eV). This implies that the Cu_1/CeO_2-(111) surface can easily activate the adsorbed NH_3, leading to the formation of $NH_2^* + H^*$ species after the loading of single-atom Cu on the Cu_1/CeO_2-(111) surface (where ***** denotes the adsorbed species).

Furthermore, theoretical calculations demonstrate that the kinetic barrier for the oxidative dehydrogenation of NH_2^* ($NH_2^* \rightarrow NH^* + H^*$) is significantly high, measuring 1.3 eV (as shown in **Fig. S51**). As a result, the Cu_1/CeO_2-(111) surface effectively prevents the overoxidation of NH_3 due to this barrier. In addition, as shown in the NH_2NO^* formation stage in **Fig. S50**, NO is adsorbed onto the lattice oxygen sites in proximity to NH_2^* species, representing an exothermic process. NH_2^* further reacts with NO to form $^*NH_2NO$, with a computed reaction free energy change of merely 0.09 eV and a kinetic barrier of 0.69 eV. Thus, the reaction of NH_2 with NO to form $^*NH_2NO$ is favored over further dehydrogenation (0.69 eV vs. 1.3 eV). This suggests that the

Cu_1/CeO_2-(111) surface is less prone to NH_3 overoxidation, indicating that the Cu_1/CeO_2 SAC should display excellent N_2 selectivity.

Based on the DFT calculations described above, after the adsorption and oxidative dehydrogenation of the NH_3 molecule, it reacts with NO and forms an N-N bond. Subsequently, the $^*NH_2NO$ group decomposes to form an N_2 molecule and an H_2O molecule. The detailed reaction pathway for the NH_2NO decomposition stage is displayed in **Fig. S50**. The NH_2NO^* undergoes dehydrogenation to form $NHNO^*$ with a low kinetic barrier of only 0.13 eV and a free energy change of 0.12 eV. Thereafter, the chemisorbed $NHNO^*$ on the surface undergoes a rotational transformation to a more stable $NHNO^*$ configuration with a free energy change of 0.12 eV. In assessing the N_2 selectivity of the Cu_1/CeO_2-(111) surface, we determined the energy change involved in the dehydrogenation reaction of $NHNO^*$ on the Cu_1/CeO_2-(111) surface, leading to the formation of N_2O (**Fig. S52**), as well as the reaction pathway of N_2 formation (**Fig. S50**). Notably, the reaction of $NHNO^*$ to N_2^* + OH^* is a highly exothermic process, exhibiting a significant free energy change of –2.57 eV, while the dehydrogenation of $NHNO^*$ to N_2O is an endothermic reaction with a free energy change of 0.11 eV. Moreover, the kinetic barrier for the $NHNO^*$ reaction to N_2^* + OH^* is 0.92 eV, which is lower compared to the barrier for $NHNO^*$ dehydrogenation to N_2O (1.35 eV). Therefore, the formation of N_2 and OH^* from $NHNO^*$ on the Cu_1/CeO_2-(111) surface is both thermodynamically and kinetically more favorable than the formation of N_2O and H^* from $NHNO^*$. This result aligns with observations of lower N_2O generation and higher N_2 selectivity on the Cu_1/CeO_2 surface during the subsequent SCR catalytic performance test. Lastly, the reaction of OH^* and H^* to form H_2O releases the energy of 0.14 eV and requires only a low kinetic barrier of 0.23 eV, as indicated by transition state 5 (TS5) in **Fig. S50**. As H_2O and N_2 molecules are released from the single-atom sites, one H^* remains on the catalyst surface during this process, leading to the reduction of one Ce^{4+} to Ce^{3+}, as depicted in **Fig. S50**. The coverage of H^* on the surface can lead to the deactivation of the catalyst; thus, it is crucial to remove the residual H^* from the surface in order to restore the catalyst surface. Therefore, the introduction of oxidizing species is required to remove H^* and oxidize Ce^{3+} to Ce^{4+}. For the standard-SCR reaction, there are several potential species that can participate in the removal of H^*, including surface lattice oxygen, gas-phase O_2, and O_2 activated by surface oxygen vacancies. In our DFT calculations, we consider these species to explore the pathways for H^* removal. In this process, firstly, the possible pathways of H^* removal via gas-phase O_2 and lattice oxygen are

calculated, as shown in **Fig. S53**. Notably, the kinetic barrier for the H^* removal catalyzed by O_2 is found to be as high as 1.84 eV, while it is determined to be 3.64 eV for the lattice oxygen catalyzed pathway. Hence, the O_2-catalyzed H^* removal pathway activated by oxygen vacancies is being considered for further studies. Meanwhile, we examine the most stable position of oxygen vacancies on the catalyst surface when the surface is covered with two H^* species (**Fig. S54a**). By considering all possible structures (**Fig. S54b**–**i**), it is found that the formation energy of the oxygen vacancy is the lowest when it is in the nearest neighbor position to H^* (**Fig. S54b**). The structure depicted in **Fig. S54b** is utilized for the calculation of the H^* removal reaction pathway. The configurations and corresponding energies of catalytic intermediates and TS in the O_2-catalyzed H^* removal pathway activated by oxygen vacancies are shown in **Fig. S55**. Initially, gaseous O_2 molecules are adsorbed on the oxygen vacancies present on the Cu_1/CeO_2-(111) surface with an adsorption energy of –2.9 eV. Among them, one oxygen atom from O_2^{2-} fills the oxygen vacancy, whereas the other oxygen atom remains on the catalyst surface, referred to as the O^* species. Subsequently, the H atoms of the two hydroxyl groups on the catalyst surface react with the O^* species, resulting in the cleavage of the O-O bond and the formation of H_2O. The activation energy for this process is observed to be 0.70 eV, as indicated by the TS in **Fig. S55**. The H_2O molecules subsequently desorb, and the catalyst surface returns to its initial state, completing the entire SCR catalytic cycle. The theoretical calculation results demonstrate that the presence of Cu single atoms supported on the CeO_2-(111) surface enhances the kinetics of both the NH_3 dissociation step and the H^* removal step.

Supplementary Note 11: Characterization of the Cu_1/CeO_2-(111)-L

XANES and EXAFS spectra further confirm that Cu exists as single atoms. Analysis of the near-edge data of the Cu element (**Fig. S56a**) shows that the Cu in Cu_1/CeO_2-(111)-L remains in the oxidation state. As shown in **Fig. S56b** and **c**, the main peak position of the Cu_1/CeO_2-(111)-L catalyst, found between 1–2 Å, is attributed to the absorption oscillation of the first shell of the Cu-O bond. Wavelet transform was carried out, and Cu Foil, Cu_2O, and CuO were also analyzed as control groups (**Fig. S56d**–**g**). In the wavelet transform map, red represents high intensity, and green and blue represent low intensity. It can be seen from the figure that the strongest oscillation of Cu_1/CeO_2-(111)-L appears at about 5 $Å^{-1}$, while Cu Foil exhibits the largest oscillation intensity at about 8 $Å^{-1}$, which proves that the Cu in Cu_1/CeO_2-(111)-L sample exists in the coordination mode of Cu-O. Quantitative EXAFS fitting results are provided in **Fig. S57** and **Table S11**.

Supplementary Note 12: LCA and TEA for C-SACs

Early-stage life cycle assessments (LCA) and techno-economic analyses (TEA) are essential tools to quantitatively link fundamental material innovations to practical, process-level implementations by evaluating the environmental impacts and economic feasibility of catalytic systems. These assessments comprehensively account for emissions, energy consumption, and material waste, providing critical insights into the sustainability of emerging technologies and highlighting areas for potential optimization.

Fig. S59a and **Fig. S59b** illustrate the environmental impact distribution associated with the production of commercial V-W-Ti catalysts and our Cu_1/CeO_2-(111)-L catalyst, respectively. As shown in **Fig. S59c**, Cu_1/CeO_2-(111)-L exhibits markedly lower environmental impacts across all 11 assessed sustainability indicators. These improvements are primarily due to our energy-efficient synthesis process, which eliminates the need for high-temperature treatments (e.g., calcination above 400 °C), utilizes low-cost and readily available precursors, and ensures nearly complete utilization of metal species—thereby minimizing waste generation. **Fig. S59d** further highlights the environmental advantages by comparing the global warming potential over a 100-year horizon (GWP_{100}) for Cu_1/CeO_2-(111)-L and V–W–Ti catalysts across a range of reaction temperatures. While the GWP_{100} of V–W–Ti catalysts show a moderate decline with increasing temperature, Cu_1/CeO_2-(111)-L consistently maintains a significantly lower GWP_{100} throughout. This stable and reduced carbon footprint underscores the robustness and suitability of Cu_1/CeO_2-(111)-L for industrial operations, particularly in systems subject to thermal variation.

We employed the annualized cost method to compare the economic performance of Cu_1/CeO_2-(111)-L with commercial catalysts using industrial-scale process simulations. As shown in **Fig. S59e**, Cu_1/CeO_2-(111)-L exhibits significantly lower overall production costs. While fixed capital investment and fixed costs of production are comparable between the two systems, Cu_1/CeO_2-(111)-L benefits from notably lower material costs—primarily due to a simpler synthesis pathway and near-complete utilization of raw materials, which reduce waste and improve yield. These results confirm the strong technical and economic viability of Cu_1/CeO_2-(111)-L for industrial-scale application.

Supplementary Note 13: Ni_1/CeO_2-L for Efficient C_4 Fraction Hydrogenation

Reaction principles and requirements: The hydrogenation process involves converting olefins (e.g., trans- and cis-butene, isobutene, and 1-butene), along with minor diolefins, into butane. This exothermic reaction proceeds under controlled conditions of temperature, pressure, and catalyst activity. By significantly reducing the concentration of reactive olefins and diolefins, hydrogenation produces stable alkanes suitable for subsequent cracking or further chemical processing. Stabilizing these intermediates lowers the risk of coking and other side reactions downstream, thus improving both operational efficiency and reliability.

Experimental validation: We used C_4 fractions from the *Fushun Petrochemical Olefin Plant* as the hydrogenation feedstock. **Table S12** details the feed composition, which contains substantial olefins and diolefins, posing challenges for sintering resistance and catalyst deactivation. **Fig. S60** illustrates the product distribution and olefin conversion efficiency of Ni_1/CeO_2-L C-SACs during the C_4 hydrogenation process. Throughout the continuous 570-hour testing period, Ni_1/CeO_2-L exhibited exceptional catalytic stability, consistently maintaining olefin conversion levels above 95%.

Supplementary Figures

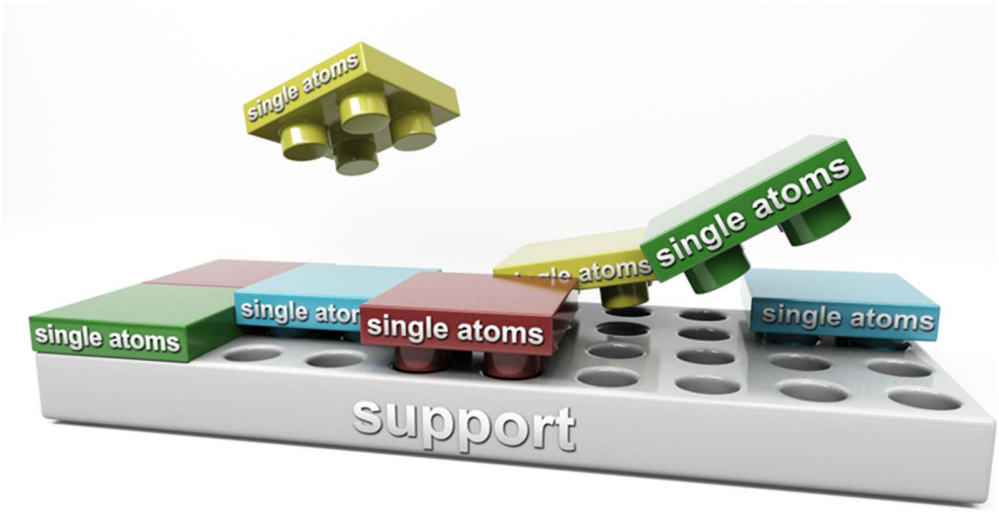

Fig. S1 Inspiration for the design of C-SACs. The design of C-SACs is inspired by the modular assembly of building blocks. By transforming supports into "clicking blocks" with anchoring sites, single atoms can be precisely and stably anchored, mimicking the simplicity and precision of click chemistry.

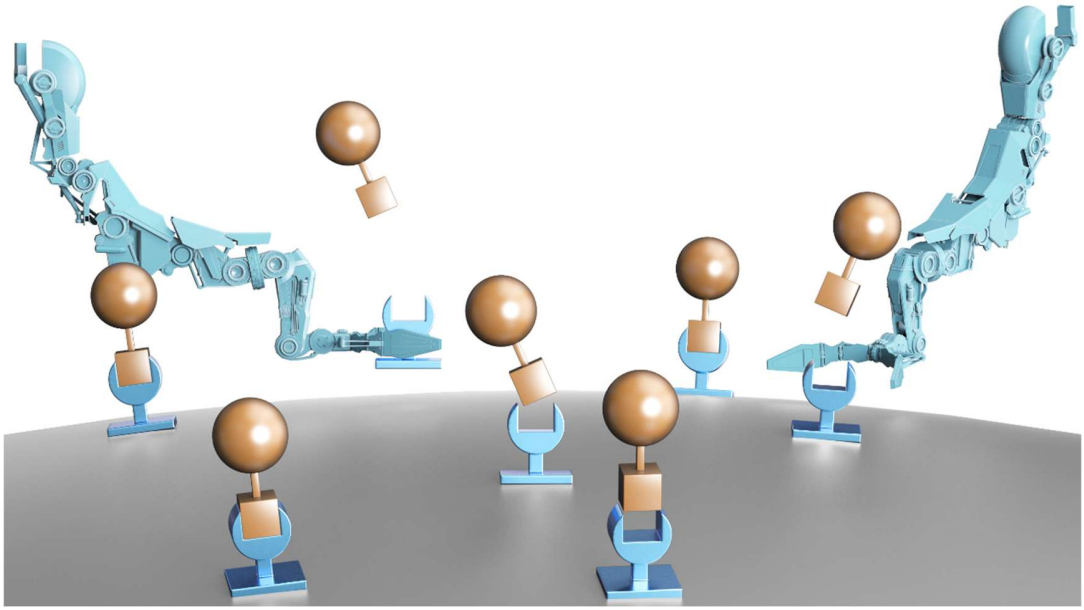

Fig. S2 Surface-engineered supports as "clicking blocks" for single-atom anchoring. Supports are converted into "clicking blocks" via surface modifications that introduce anchoring sites for single metal atoms. This transformation ensures precise and stable atomic anchoring, enhancing catalyst durability and performance.

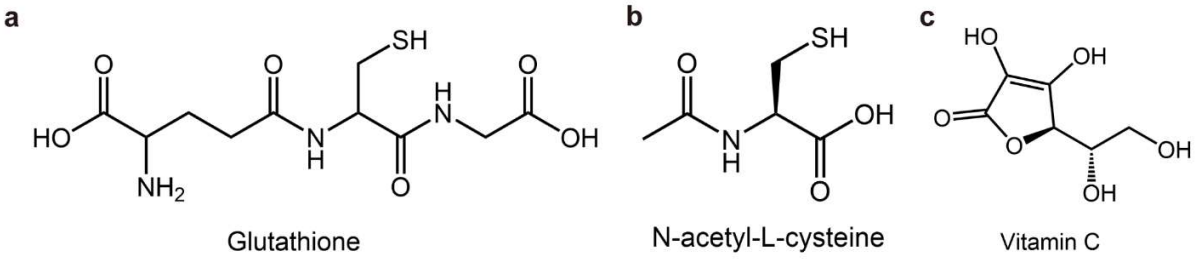

Fig. S3 Optimized geometries of potential clicking-auxiliaries for single-atom anchoring. Shown are the optimized geometries of representative clicking-auxiliaries that function as electron-donating agents to stabilize single atoms on supports. **a**, Glutathione (GSH). **b**, N-acetyl-L-cysteine (NAC). **c**, Vitamin C (VC).

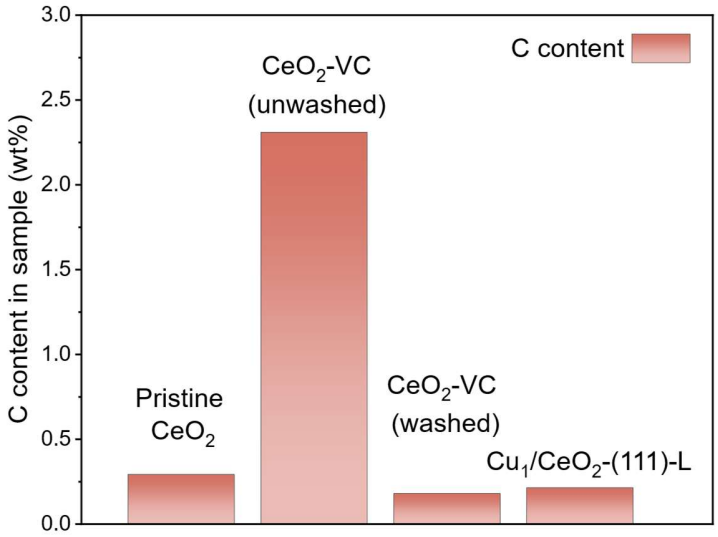

Fig. S4 Elemental analysis of carbon content in samples at various synthesis stages. From left to right: pristine CeO_2; CeO_2-VC (unwashed), prepared by reacting CeO_2 with VC for 2 minutes without subsequent washing; CeO_2-VC (washed), obtained by sequentially washing the unwashed sample with ethanol, 20 mM sodium carbonate solution, and deionized water; and the final catalyst sample, Cu_1/CeO_2-(111)-L.

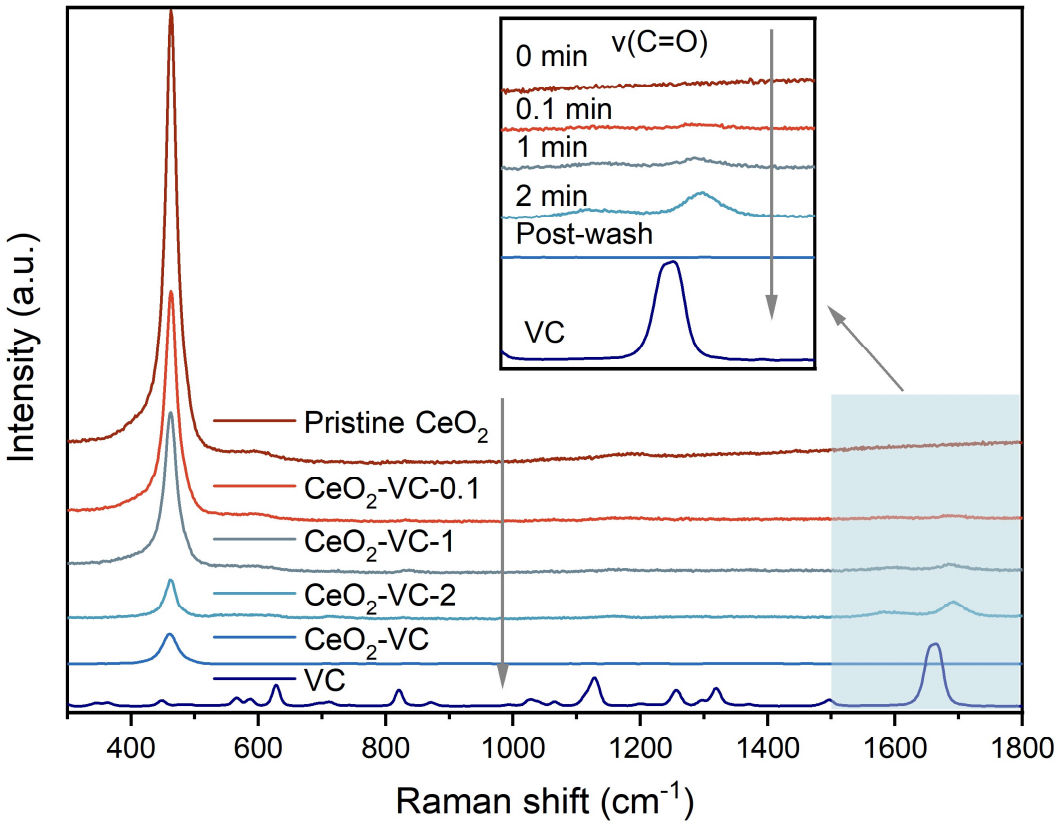

Fig. S5 In situ Raman spectra of CeO_2 samples before and after interaction with VC. Spectra are shown for pristine CeO_2 (no VC interaction), CeO_2 samples at various intervals following VC addition (0.1 min, 1 min, and 2 min, labeled as CeO_2-VC-0.1, CeO_2-VC-1, and CeO_2-VC-2, respectively), and the CeO_2-VC sample (CeO_2-VC-2 after washing). The spectrum labeled "VC" represents pure VC without CeO_2 as a reference, exhibiting a distinct carbonyl vibration peak at approximately 1700 cm^{-1}. Inset: Enlarged view of the carbonyl vibration region.

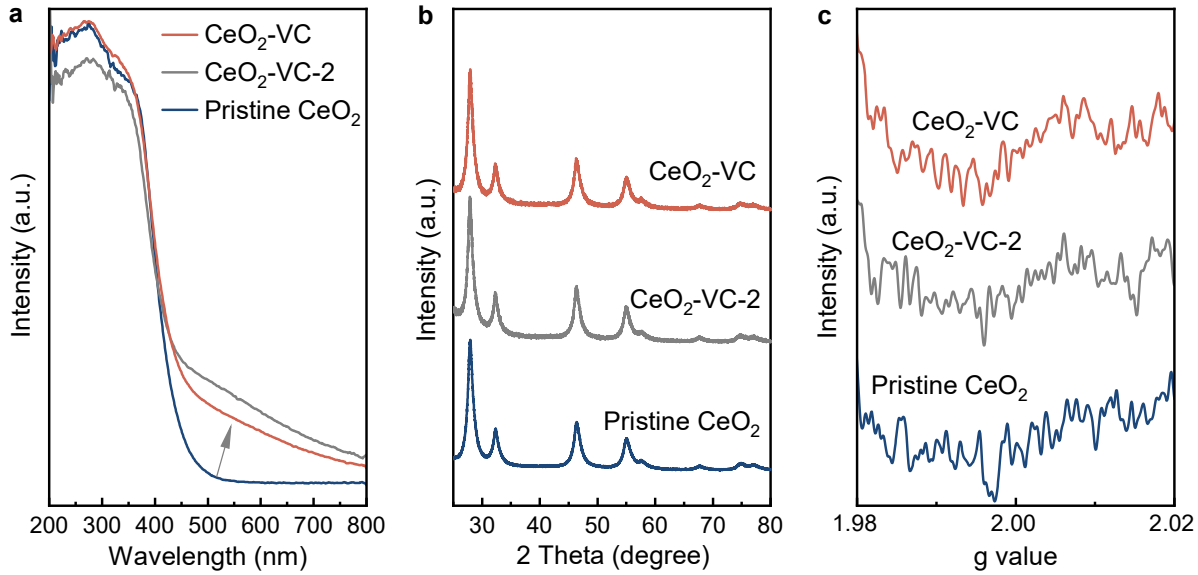

Fig. S6 (a) UV-vis diffuse reflectance spectroscopy (DRS) spectra, (b) XRD patterns, and (c) Room-temperature electron paramagnetic resonance (EPR) spectra of pristine CeO_2, CeO_2-VC-2 (VC-treated for 2 min without washing), and CeO_2-VC (VC-treated for 2 min followed by thorough washing).

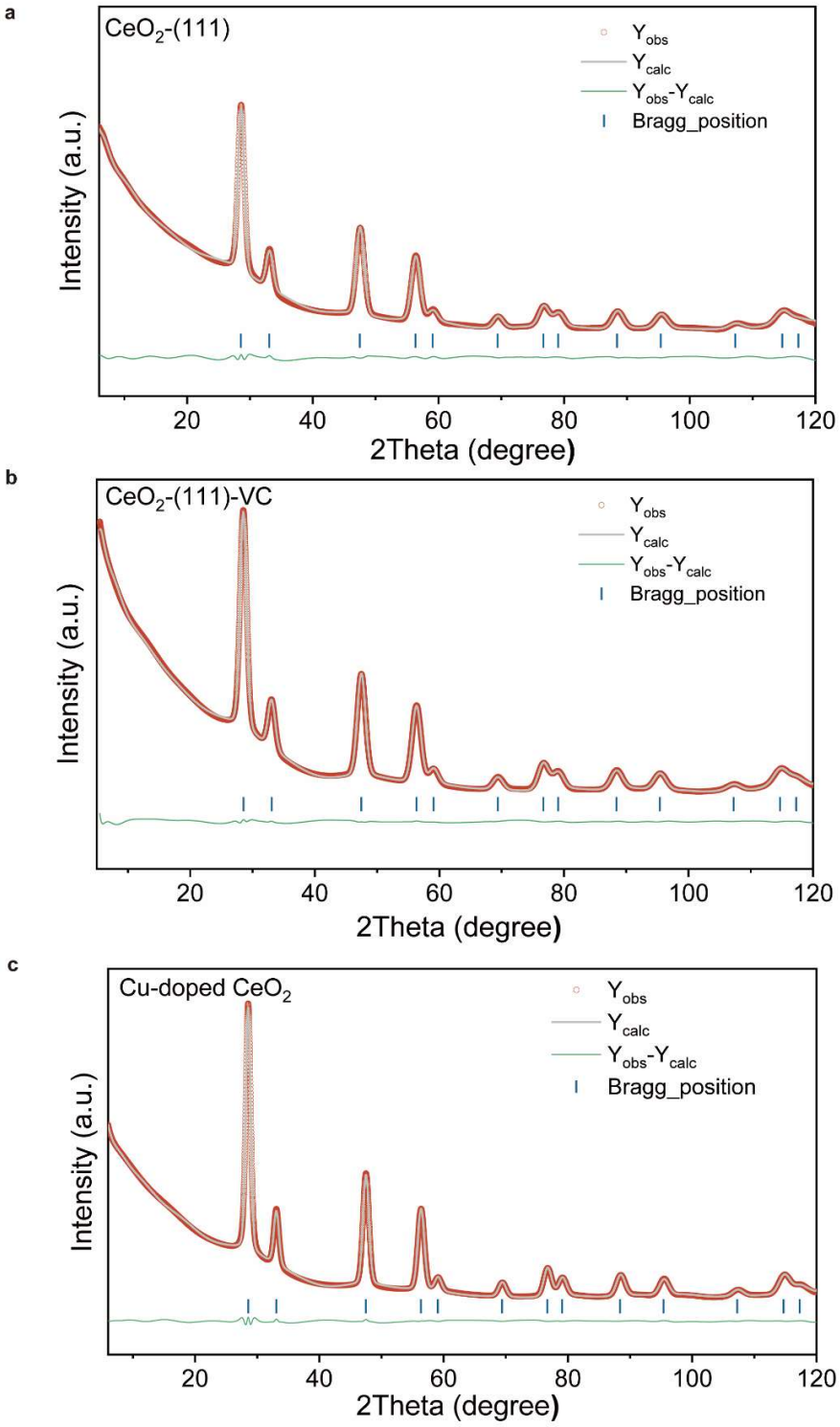

Fig. S7 XRD Rietveld refinement results of CeO_2 support. a, CeO_2-(111). **b**, CeO_2-(111)-VC. **c**, Cu-doped CeO_2 catalysts.

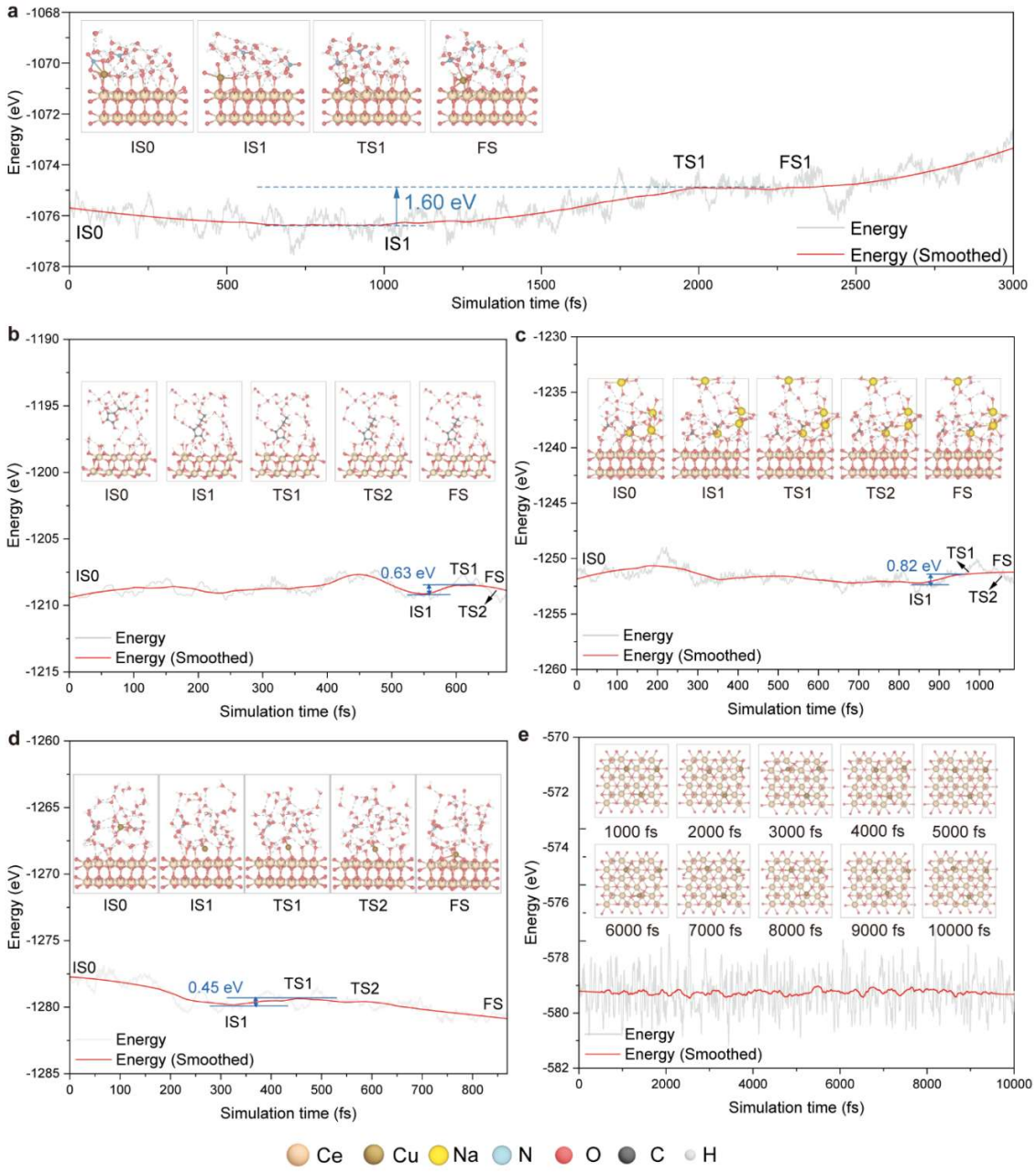

Fig. S8 AIMD simulations of the C-SACs synthesis process on CeO_2 surface. Ab initio molecular dynamics (AIMD) simulations provide an intuitive and detailed view of the energy landscape evolution during the synthesis of C-SACs facilitated by clicking-auxiliaries. **a,** Energy profile for Cu^{2+} adsorption on CeO_2 without VC, revealing a substantially higher energy barrier, indicating the critical role of clicking-auxiliaries. **b,** Energy profile for the chemisorption of VC onto the CeO_2 surface, during which VC donates electrons to CeO_2 and becomes oxidized. **c,** Energy profile for the Na_2CO_3-assisted removal of surface protons from CeO_2, forming electron-rich anchoring sites. **d,** Anchoring of Cu^{2+} ions on the electron-enriched CeO_2 surface. **e,** Stability analysis of the Cu_1/CeO_2 system (NVT ensemble at 800 K).

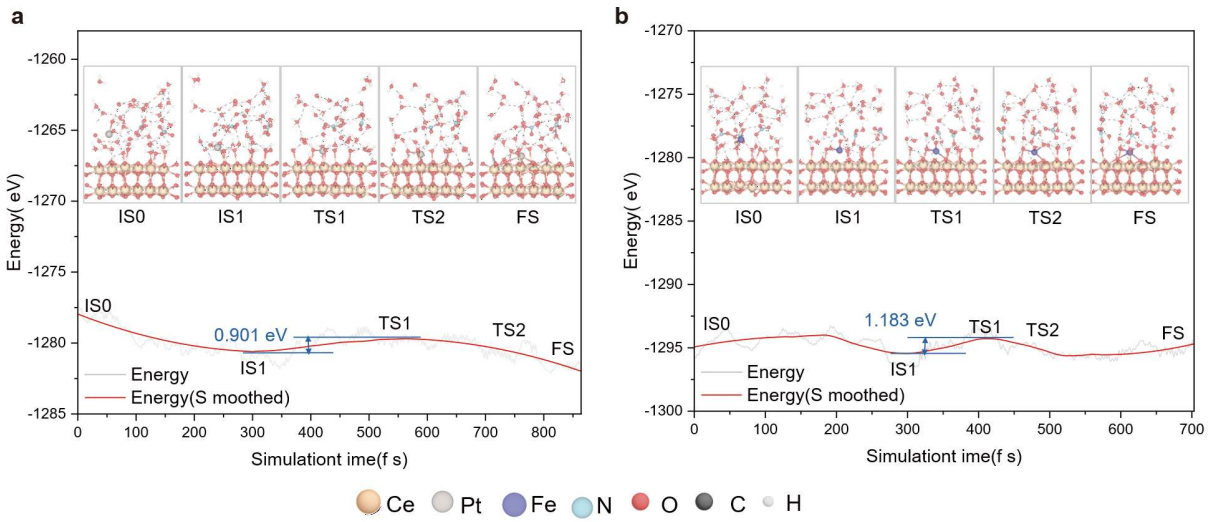

Fig. S9 AIMD simulations of Fe and Pt single-atom anchoring on the electron-enriched CeO_2 surface. Energy profiles for the electrostatic anchoring of a, Fe^{3+} (barrier: 0.90 eV) and b, Pt^{2+} (barrier: 1.18 eV) on the electron-rich CeO_2 surface, demonstrating the generality of CeO_2 as a universal anchoring platform for diverse metal species.

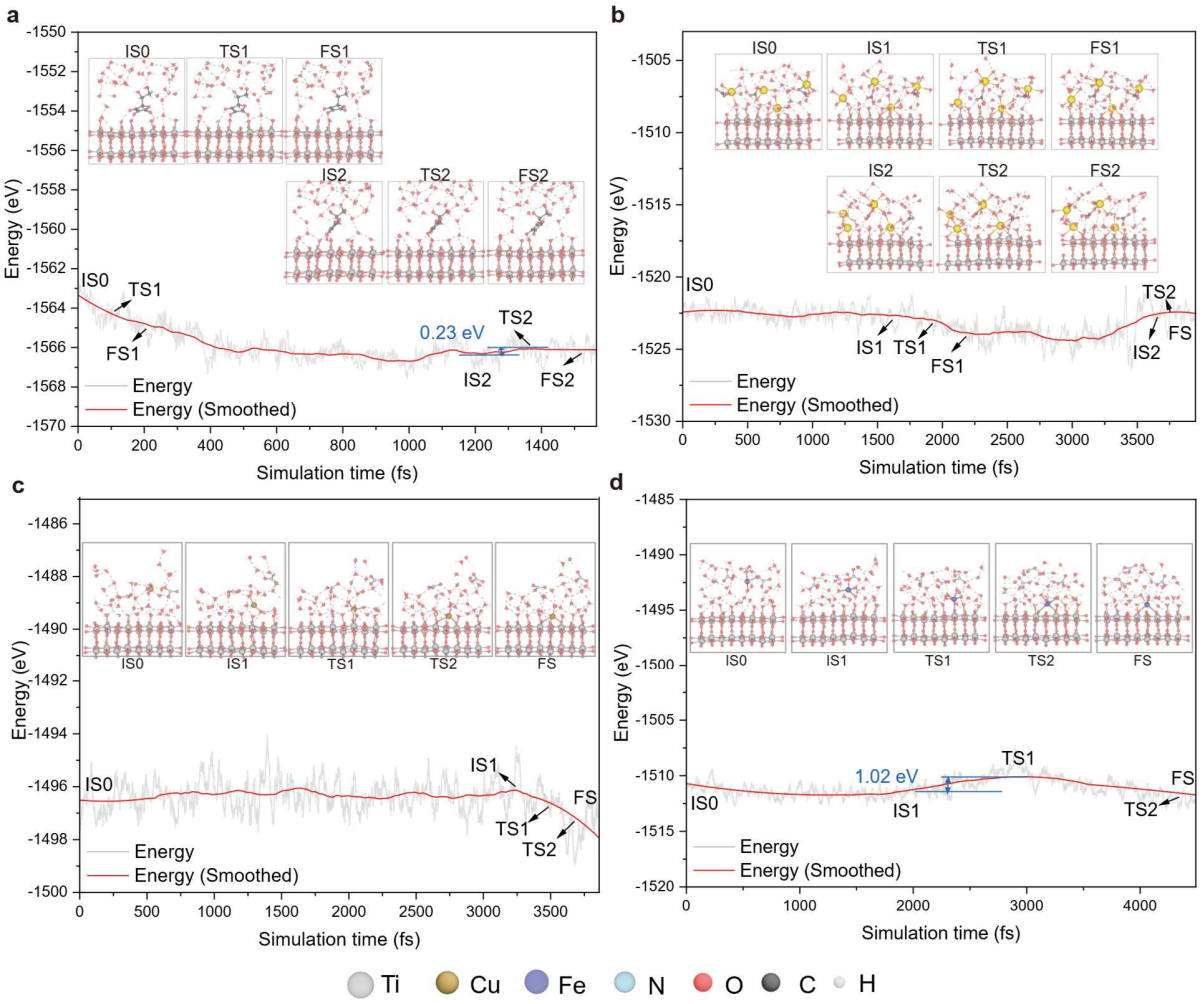

Fig. S10 AIMD simulations of the C-SACs synthesis process on TiO_2 surface. AIMD simulations demonstrate that the clicking-auxiliary-assisted anchoring strategy is transferable to TiO_2. **a**, Energy profile for the chemisorption of VC onto the TiO_2 surface, during which VC donates electrons to TiO_2. **b**, Energy profile for the Na_2CO_3-assisted removal of surface protons, forming electron-rich anchoring sites. **c**, Electrostatic attraction and anchoring of Cu^{2+} ions on the electron-enriched TiO_2 surface. **d**, Electrostatic attraction and anchoring of Fe^{3+} ions on the electron-enriched TiO_2 surface.

Fig. S11 Photographs of the Opentrons Flex liquid-handling robot in the high-throughput synthesis platform for powder-based C-SAC samples. a–**b**, Front (**a**) and top-deck (**b**) views of the liquid-handling robot. The setup includes a Heater-Shaker module (200-3000 rpm) for temperature-controlled mixing and a Temperature module for stable storage of temperature-sensitive reactants. **c**, A custom-designed, 3D-printed six-tube rack holding centrifuge tubes, containing support materials (e.g., CeO_2 slurries) and clicking-auxiliaries (e.g., VC solutions). **d**, A 3D-printed 15-channel rack for centrifuge tubes containing diverse metal precursor solutions. **e**, A 3D-printed sample holder designed for automated oscillatory mixing, improving the handling and preparation of powder-based samples. **f**–**h**, Photographs of representative candidate libraries, showcasing supports, metal precursors, and clicking-auxiliaries, respectively. **i**–**j**, Photographs showing the CeO_2 slurry before and after the addition of VC, with a visible color change indicating the clicking interaction between VC and CeO_2.

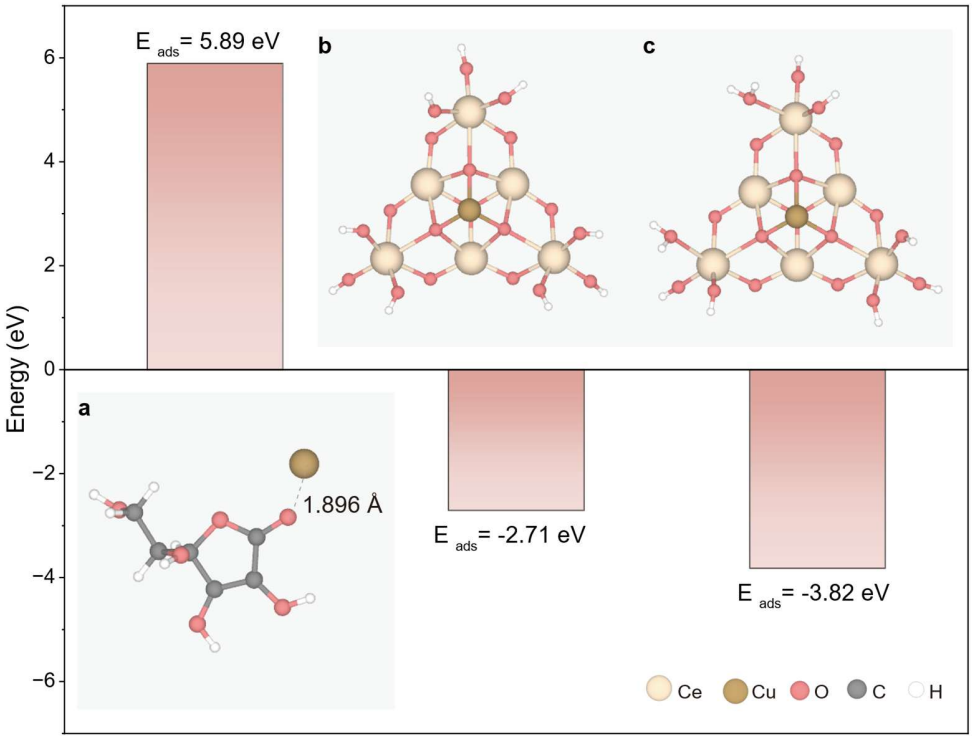

Fig. S12 Optimized adsorption configurations and corresponding adsorption energies for Cu^{2+} ions on: (**a**) isolated VC molecules; (**b**) pristine CeO_2 surfaces without electron transfer from VC; (**c**) electron-enriched CeO_2 surfaces resulting from VC-induced electron transfer.

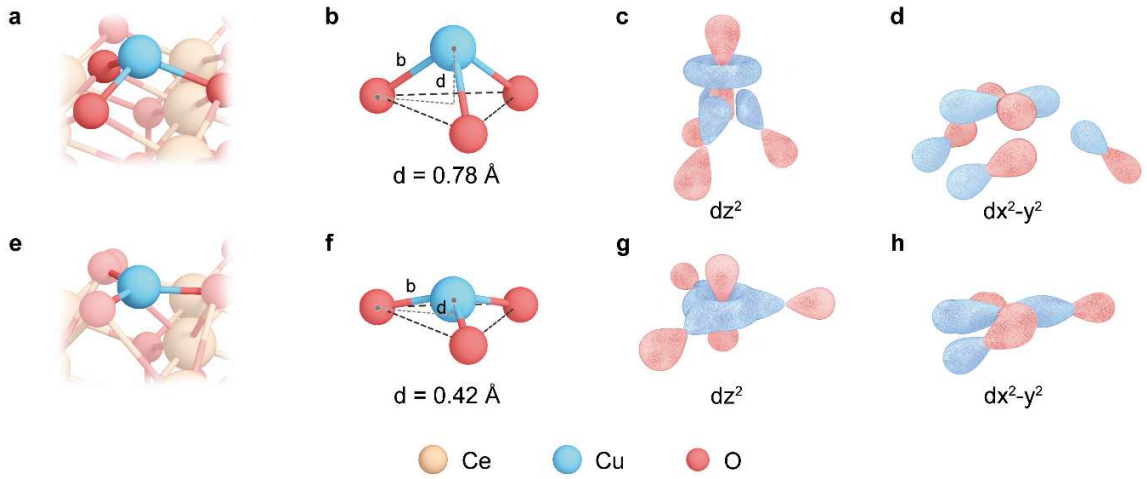

Fig. S13 Cu^{2+} adsorption and orbital interaction with surface oxygen before and after VC^{-} adsorption in A-D and E-H, respectively. a&e, Optimized geometry. **b&f**, Cu-O_3 deviation from ideal planar configuration, labelled by the distance d between Cu and O plane. **c&g,** d_{Z^2} orbital interacting with a_1-SALC. **d&h,** $d_{x^2-y^2}$ orbital interaction with e"-SALC. Cu, O and Ce are shown as blue, red and antique white balls. Atoms are color-coded as follows: cerium (yellow), copper (blue), and oxygen (red).

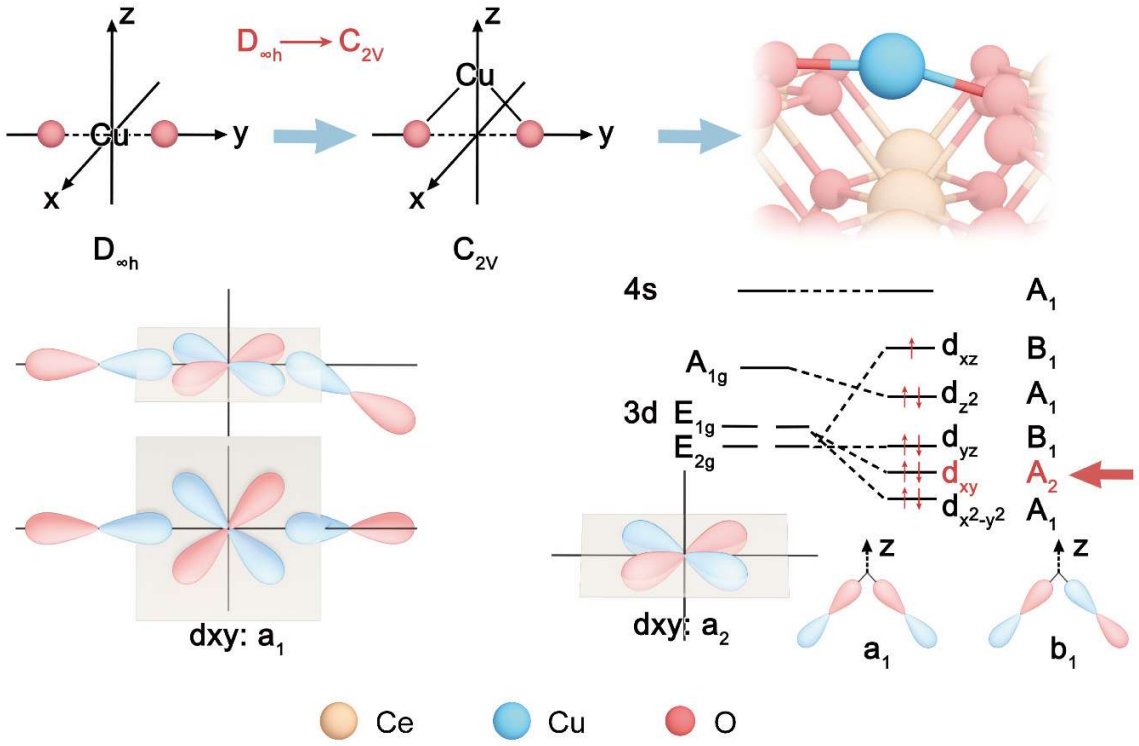

Fig. S14 Schematic illustration on the crystal field splitting of Cu 3d orbitals. Staring from Cu^{2+} adsorption with an ideal linear configuration ($D_{\infty h}$), linear ML_2 crystal field generates the splitting $A_{1g}+E_{1g}+E_{2g}$. Cu-O bonding is dominated by the orbital interactions Cu $3d_{xy}$-O $2p_y$ (a_1 symmetry). Such electronic configuration has been further split due to Cu-moving outward slightly, resulting the degeneration of $E_{1g}+E_{2g}$ into A_1 ($d_{x^2-y^2}$)+A_2 (d_{xy})+B_1 (d_{xz} + d_{yz}). Atoms are color-coded as follows: cerium (yellow), copper (blue), and oxygen (red).

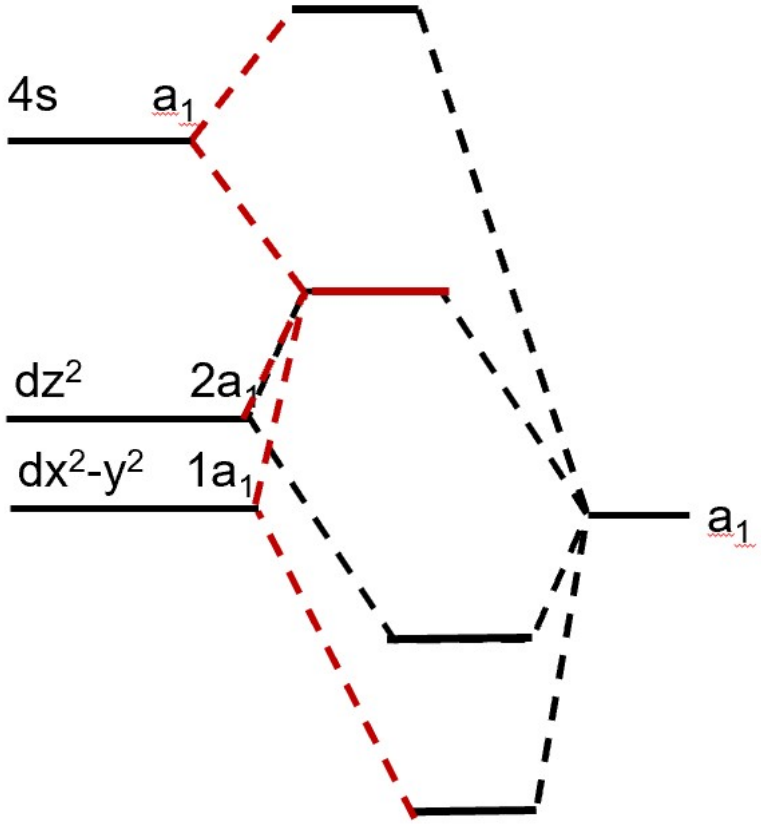

Fig. S15 Illustration of a_1-symmetry orbitals (4s, $3d_{z^2}$, $3d_{x^2-y^2}$) based on the crystal field splitting.

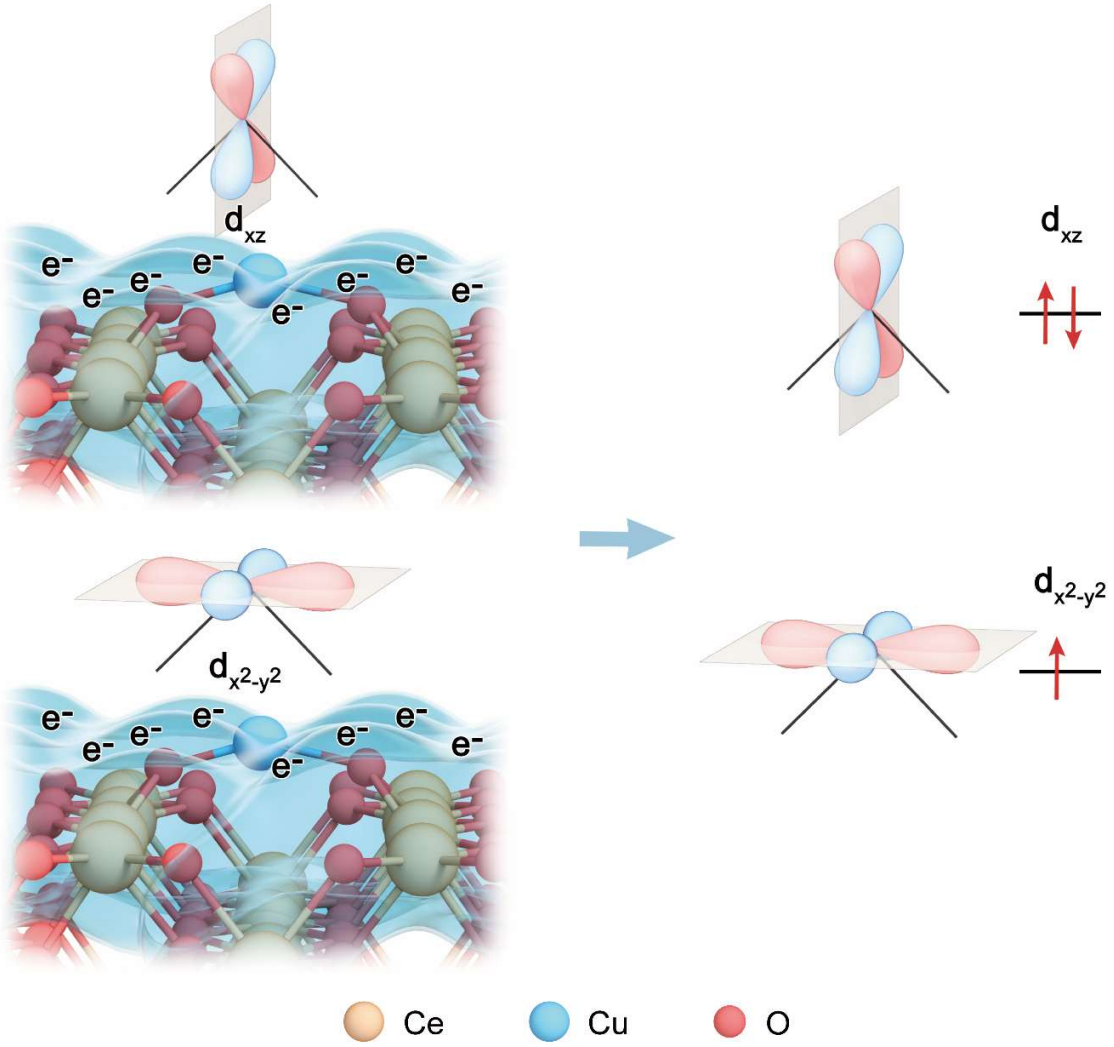

Fig. S16 Illustration of two-coordinated Cu adsorbed on the surface with orbitals (d_{xz}, $d_{x^2-y^2}$) with based on the crystal field splitting. Atoms are color-coded as follows: cerium (yellow), copper (blue), and oxygen (red).

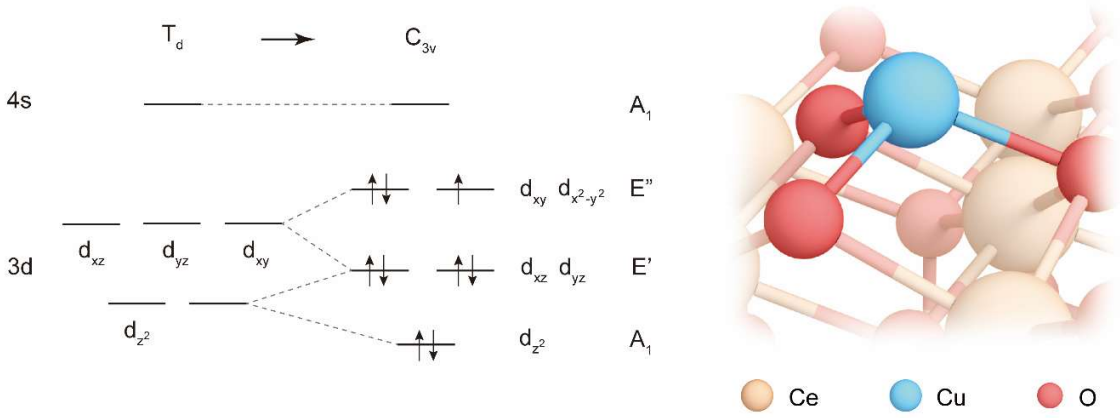

Fig. S17 Schematic illustration on the crystal field splitting of Cu 3d orbitals with three-coordination after Cu^{2+} adsorption, forming ML_3 crystal field. Starting from ideal T_d symmetry, 3d orbitals split into t_g+e_g and further degenerate into A_1+E'+E" when Cu moves outward (C_{3v} symmetry). Atoms are color-coded as follows: cerium (yellow), copper (blue), and oxygen (red).

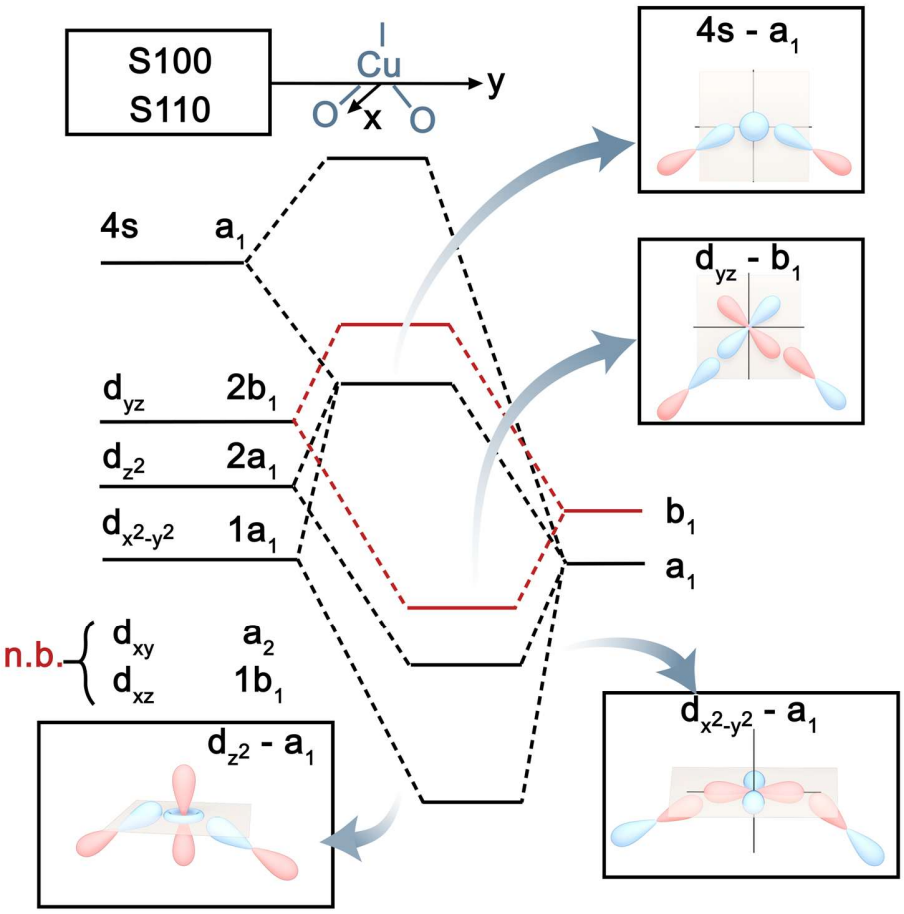

Fig. S18 Illustration of orbital interaction associated with Cu^{2+} adsorption on S100 and S110 with bent O-Cu-O configuration. Oxygen ligands present SALC orbitals (a_1+b_1), forming σ bonds between Cu and O with the contribution of $d_{x^2-y^2}$, d_{z^2}, d_{yz} and 4s based on the orbital symmetry.

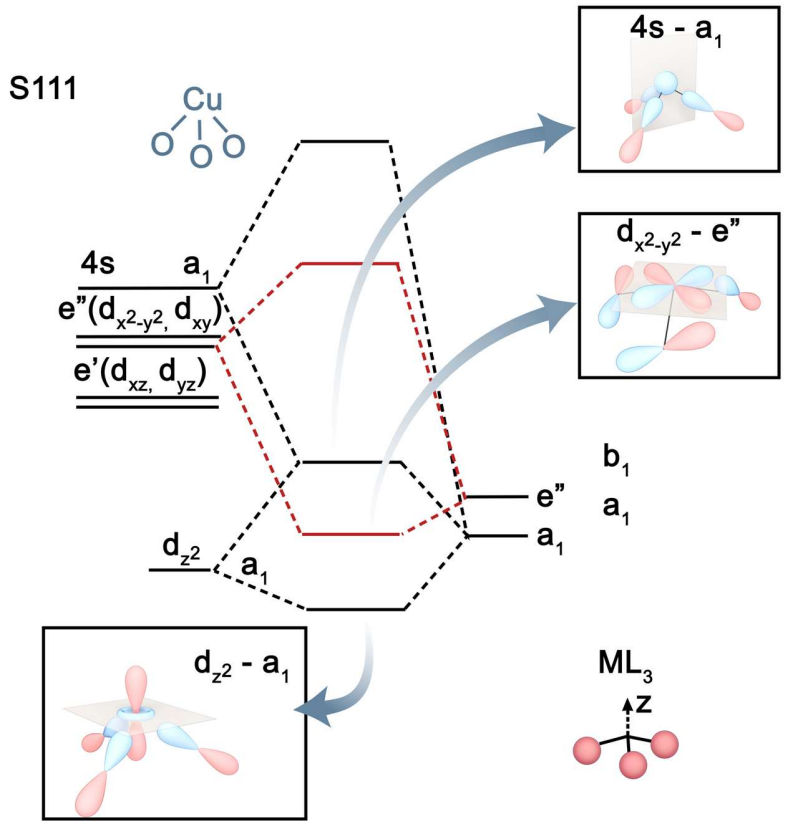

Fig. S19 Illustration of orbital interaction associated with Cu^{2+} adsorption on S111 with Cu-O_3 C_{3v} configuration (nonplanar). Oxygen ligands present SALC orbitals (a_1+e"), forming σ bonds between Cu and O with the contribution of d_{z^2}, $d_{x^2-y^2}$, and 4s based on the orbital symmetry.

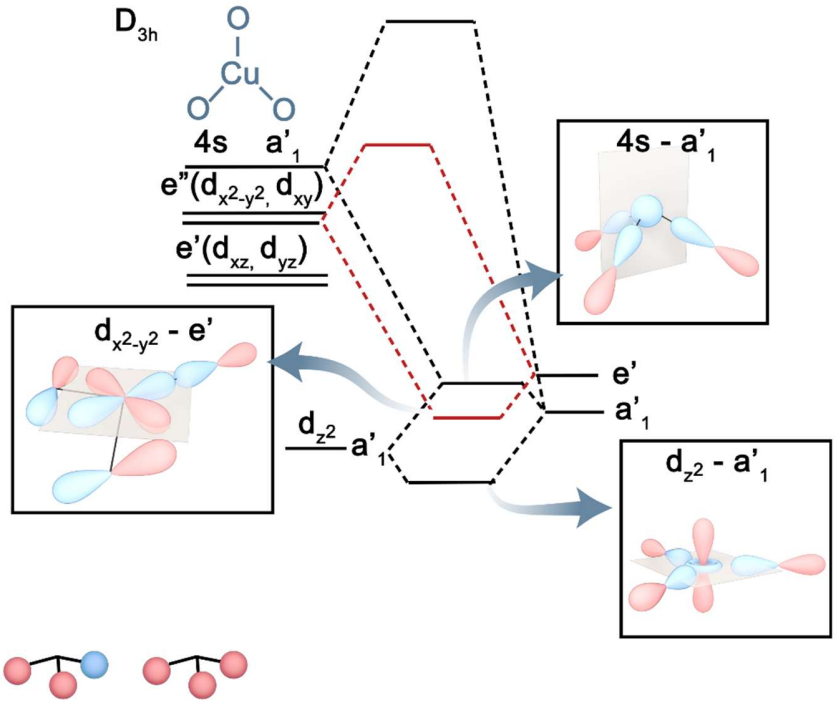

Fig. S20 Illustration of orbital interaction associated with Cu^{2+} adsorption on S111 with Cu-O_3 D_{3h} configuration (ideal trigonal planar). Valence orbitals for Cu split a_1'(d_{z^2}) + e' (d_{xz} + d_{yz}) + e" ($d_{x^2-y^2}$+d_{xy}) + a_1' (4s) and oxygen ligands present SALC orbitals (a_1'+e'). σ bonds between Cu and O are dominated by the orbital interaction d_{z^2}-a_1', $d_{x^2-y^2}$-e', and 4s-a_1 based on the orbital symmetry.

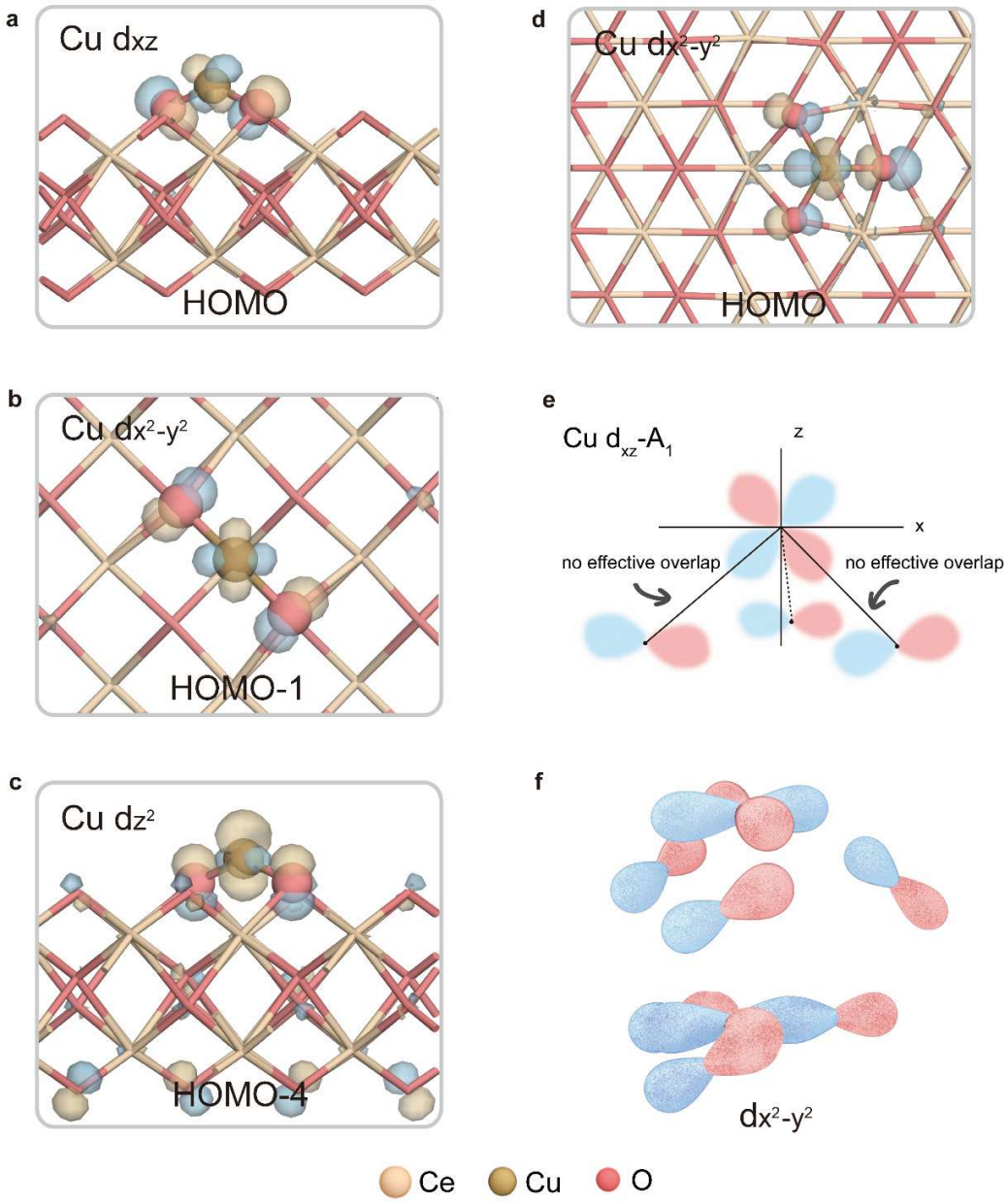

Fig. S21 Frontier molecular orbitals calculated from density functional theory using localized basis set as embedded in DMol^3. a–f, In the case of two-coordinated Cu on S100 and S110, Cu 3d components can effectively overlap with O 2p, as shown in (**a**) highest occupied molecular orbital (HOMO), (**b**) HOMO-1 and (**c**) HOMO-4. In the case of three-coordinated Cu on S111, however, such overlap can hardly be obtained. Using HOMO as an example, Cu ($d_{x^2-y^2}$) is involved as shown in (**d**) (top view), with the overlap decreasing rapidly when Cu moves outward towards the vacuum, as illustrated in (**e**) for d_{xz} and (**f**) for $d_{x^2-y^2}$. Under such situation, Cu^{2+} adsorption on S111 is relatively weak with respect to that on S110 and S100. Atoms are color-coded as follows: oxygen (red), copper (brown), and cerium (yellow).

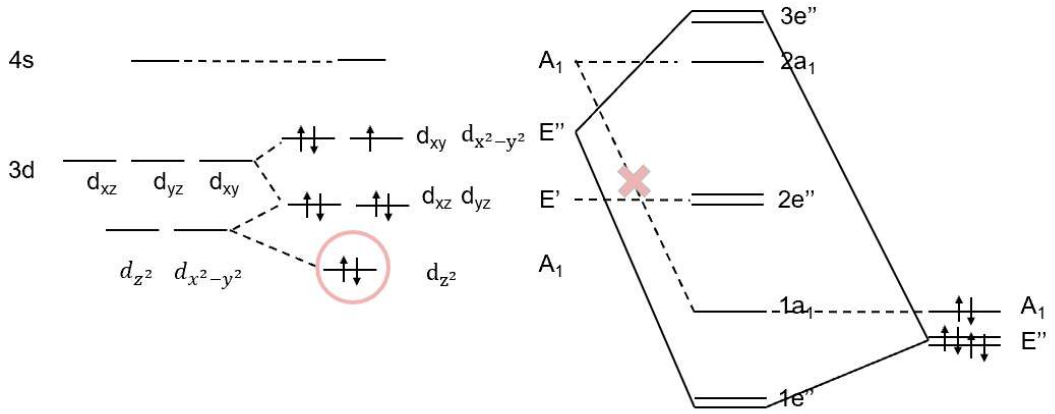

Fig. S22 Illustration of weak interaction between Cu 4s and O 2p when Cu^{2+} adsorbs on S111. Staring from ideal T_d-symmetry, 3d orbitals split into t_g ($e+t_2$) and further degenerate to C_{3v} configuration with $A_1(d_{z^2})$, $E'(d_{xz}+d_{yz})$, $E''(d_{xy}+d_{x^2-y^2})$. In all cases, 4s presents the A_1 symmetry with an energy level notably higher than Cu 3d components. In terms of orbital symmetry, d_{z^2} can interact with the A_1-symmetry SALC, but d_{z^2} is fully occupied and Cu^{2+} can hardly accept electrons via this interaction; moreover, the overlap will decrease rapidly when Cu moves outward (see Fig. S15 and Fig. S16 for comparison). Another orbital with matched A_1 symmetry is Cu 4s, which is empty for Cu^{2+} but its energy level is significantly higher than that of O 2p. Due to this constraint, Cu^{2+} can be only weakly adsorbed by S111.

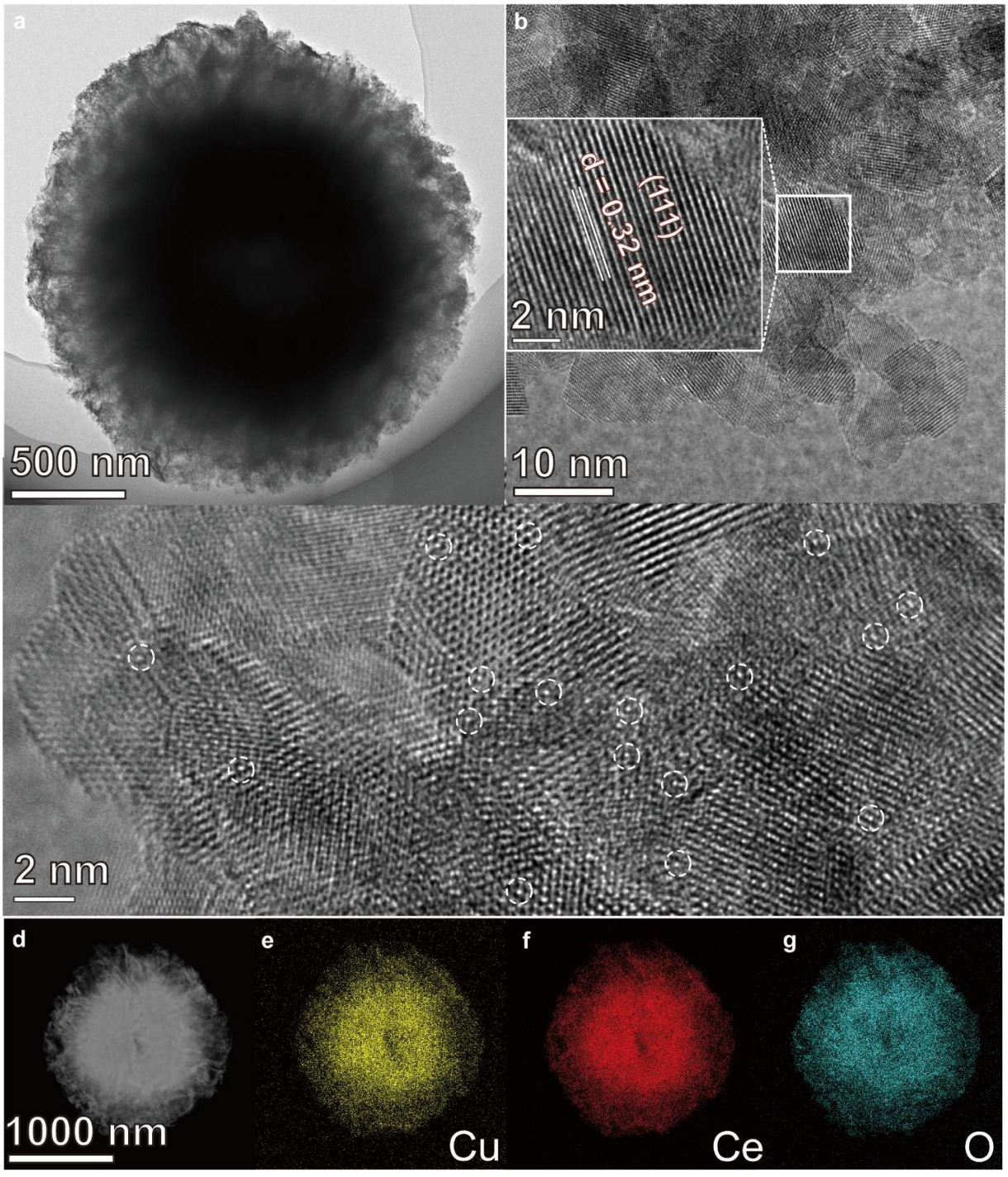

Fig. S23 Morphology and elemental characterization of Cu_1/CeO_2-(111) C-SACs. a, TEM image. **b**, HR-TEM image. **c**, High magnification HAADF-STEM image. **d**–**g**, EDS surface scanning image of Cu_1/CeO_2-(111) C-SACs.

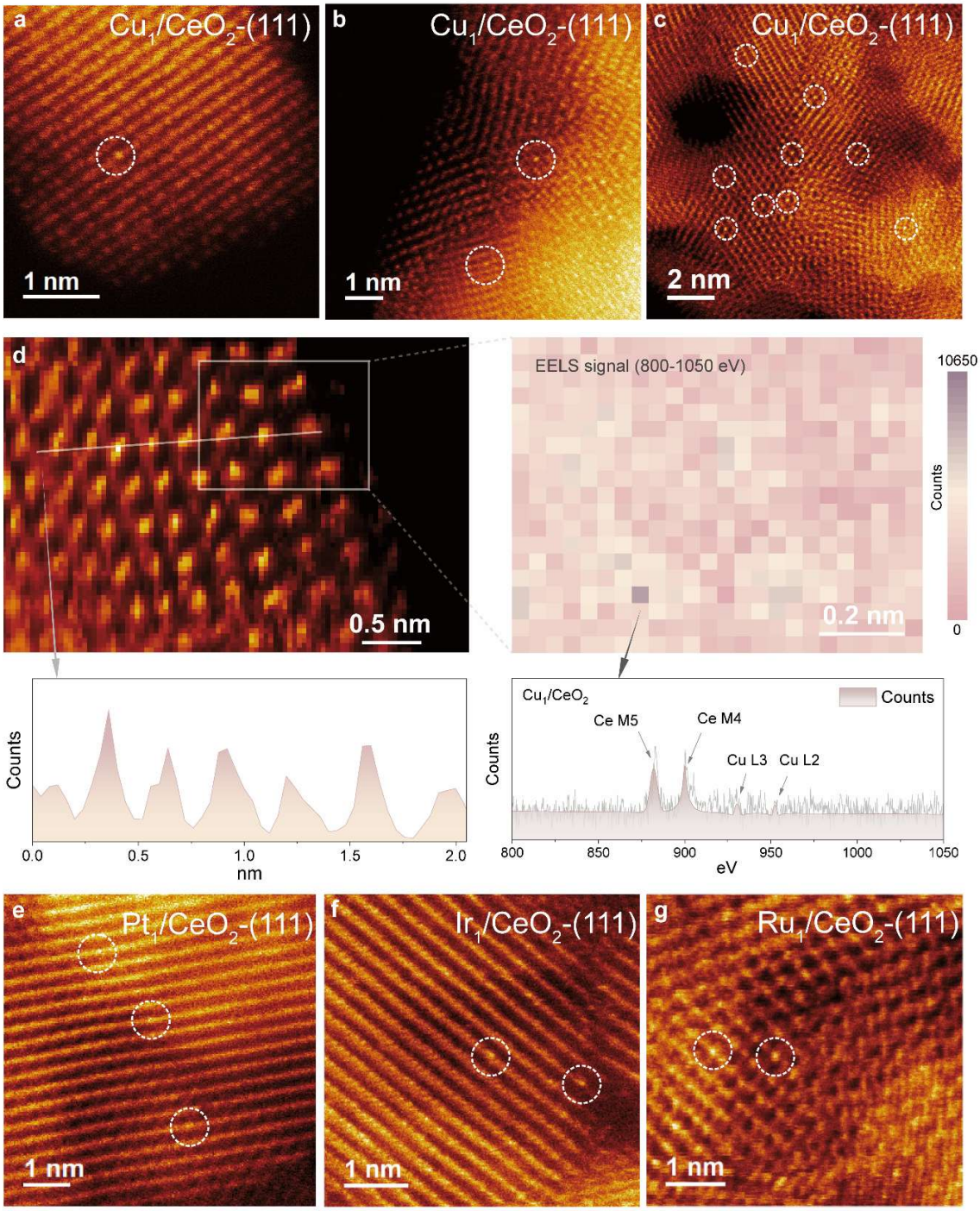

Fig. S24 AC-TEM Images and Atomic-Scale Electron Energy Loss Spectroscopy (EELS) Analysis of Selected Synthesized C-SACs on CeO_2. a–c, Atomic-resolution HAADF-STEM images of Cu_1/CeO_2-(111), highlighting the presence of single Cu atoms. **d**, EELS analysis of Cu_1/CeO_2-(111), providing detailed elemental and structural information. **e–g**, Atomic-resolution AC-HAADF-STEM images of other single-atom catalysts: (**e**) Pt_1/CeO_2, (**f**) Ir_1/CeO_2, and (**g**) Ru_1/CeO_2.

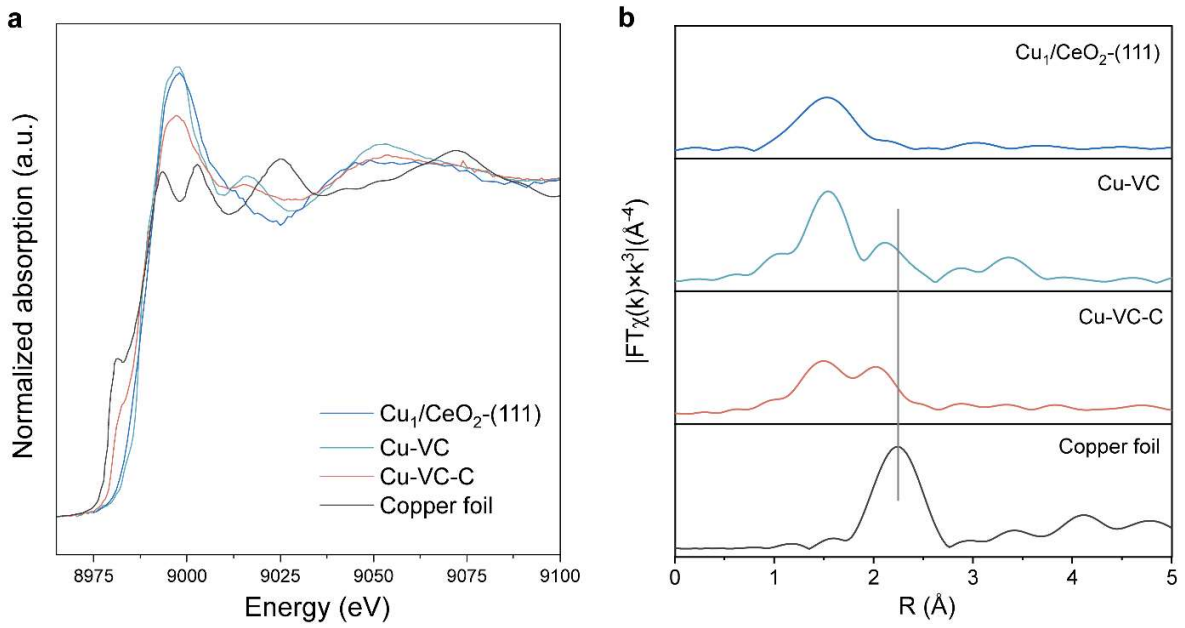

Fig. S25 Characterization of copper chemical states and fine structures. a, Cu K-edge XANES spectra of Cu_1/CeO_2-(111), Cu-VC, Cu-VC-C, and copper foil. **b,** Fourier-transformed EXAFS spectra at the Cu K-edge for Cu_1/CeO_2-(111), Cu-VC, Cu-VC-C, and copper foil. Cu-VC represents the copper–VC complex directly formed in solution, while Cu-VC-C denotes the copper–VC complex after calcination.

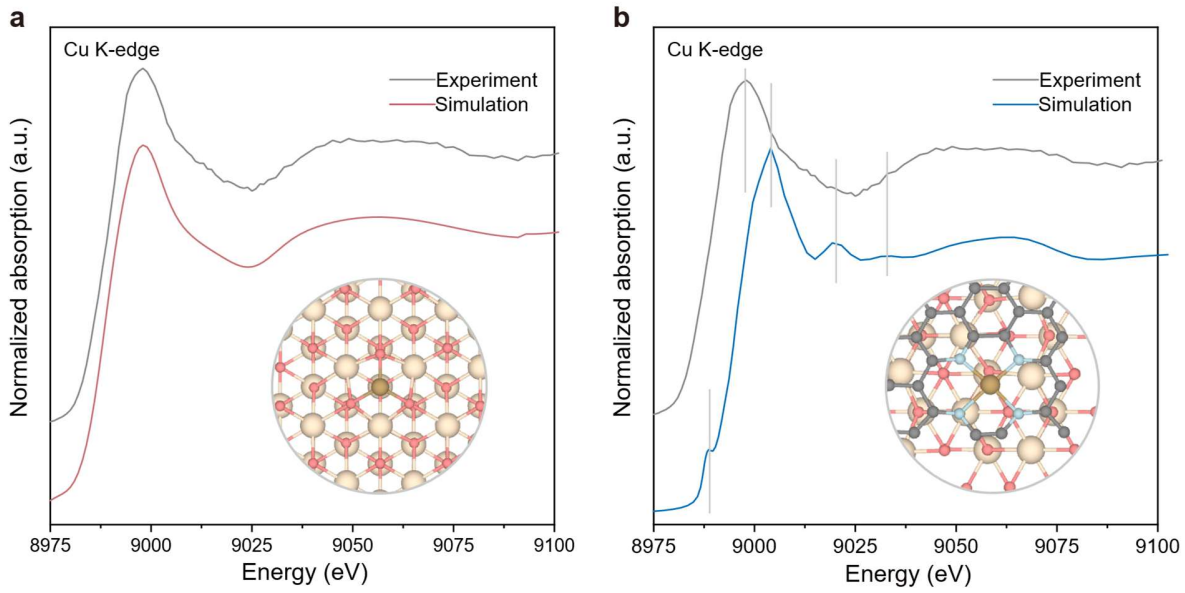

Fig. S26 Comparison of experimental and simulated Cu K-edge XANES spectra. The experimental spectra (gray lines, shown in both panels) are compared with calculated spectra based on proposed structures of (**a**) Cu_1/CeO_2-(111) and (**b**) oxide-supported M–N–C SACs. Insets show the corresponding DFT-optimized structures: Cu (brown), Ce (yellow), O (red), C (gray), and N (blue).

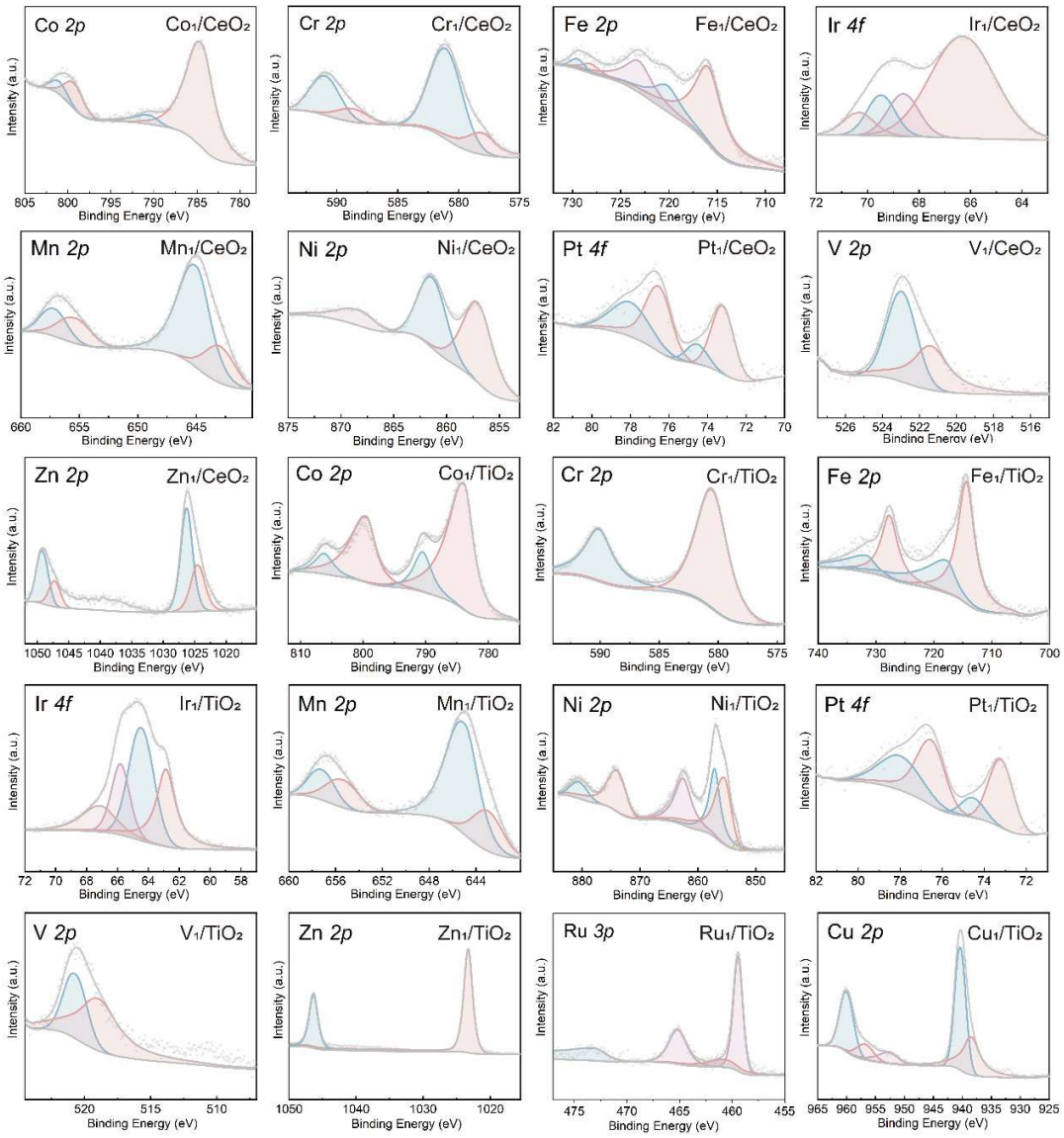

Fig. S27 X-ray Photoelectron Spectroscopy (XPS) spectra of the synthesized C-SACs.

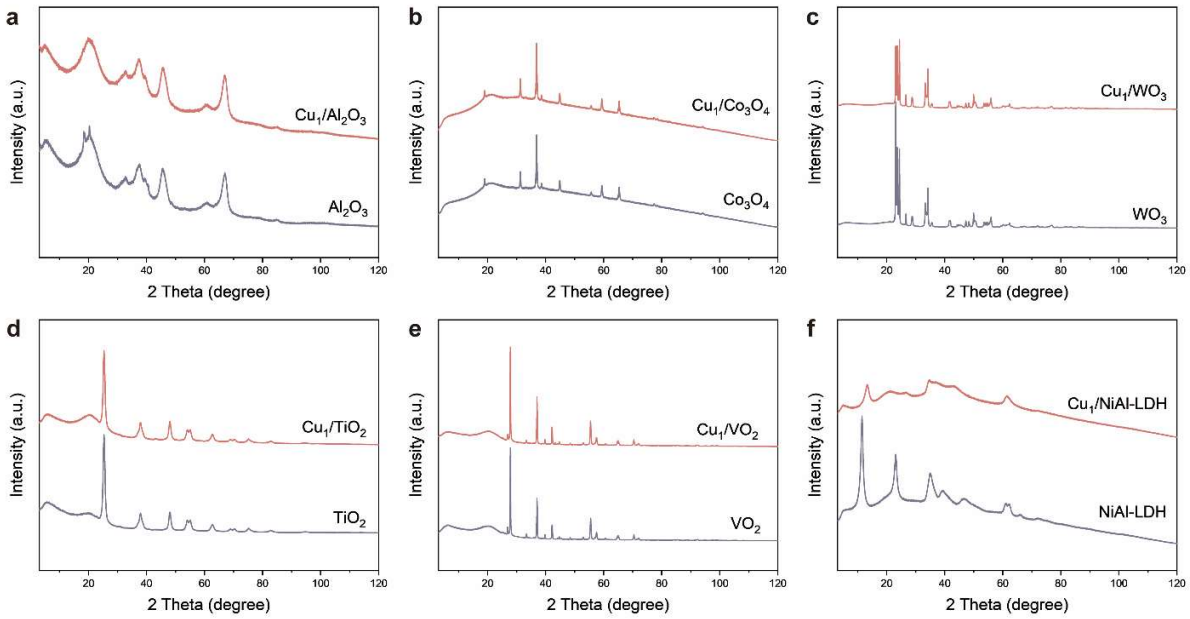

Fig. S28 XRD patterns of Cu-based C-SACs. a–f, Cu is anchored on various supports: (**a**) Al_2O_3, (**b**) Co_3O_4, (**c**) WO_3, (**d**) TiO_2, (**e**) VO_2 and (**f**) NiAl-LDH.

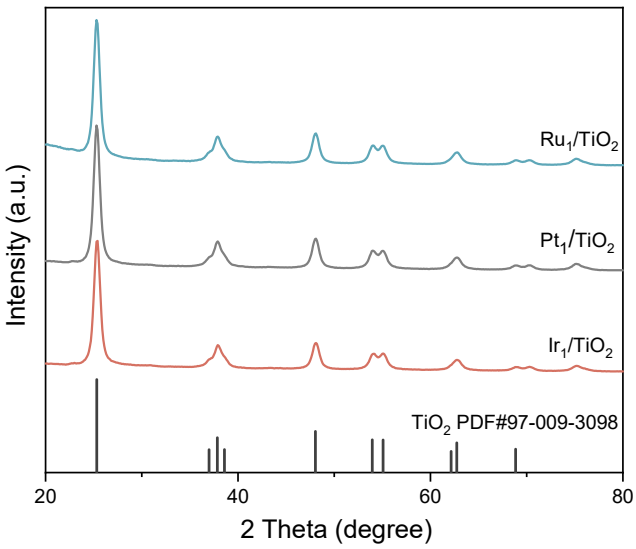

Fig. S29 The XRD patterns of Ir_1/TiO_2, Pd_1/TiO_2 and Ru_1/TiO_2.

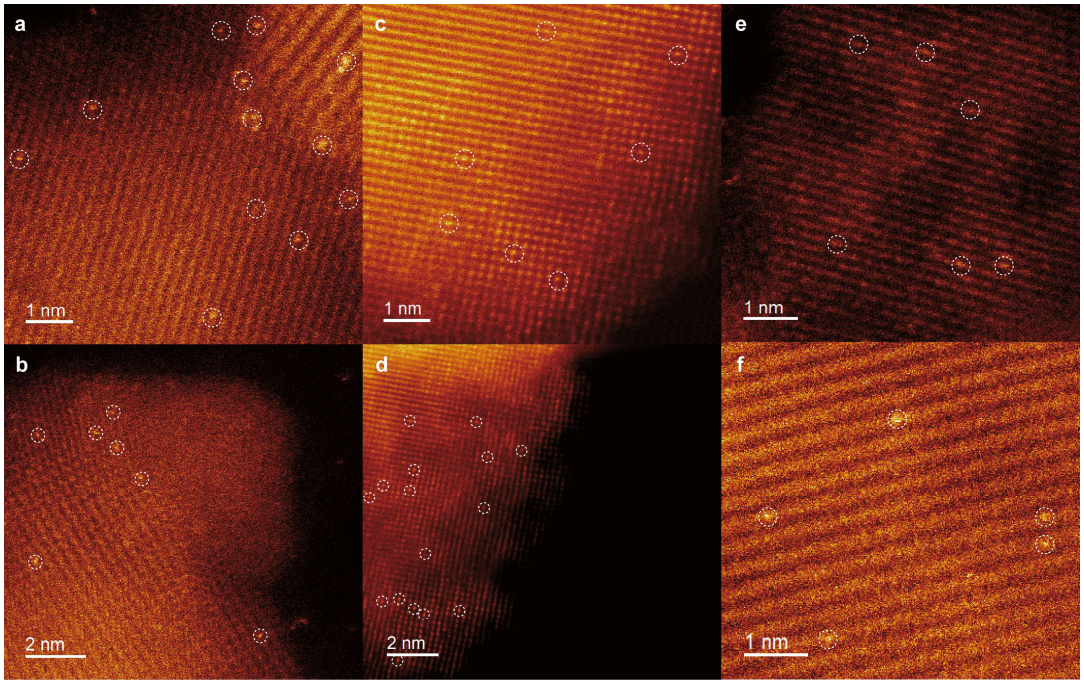

Fig. S30 HAADF-STEM images of (a–b) Ir_1/TiO_2, (c–d) Pd_1/TiO_2, and (e–f) Ru_1/TiO_2.

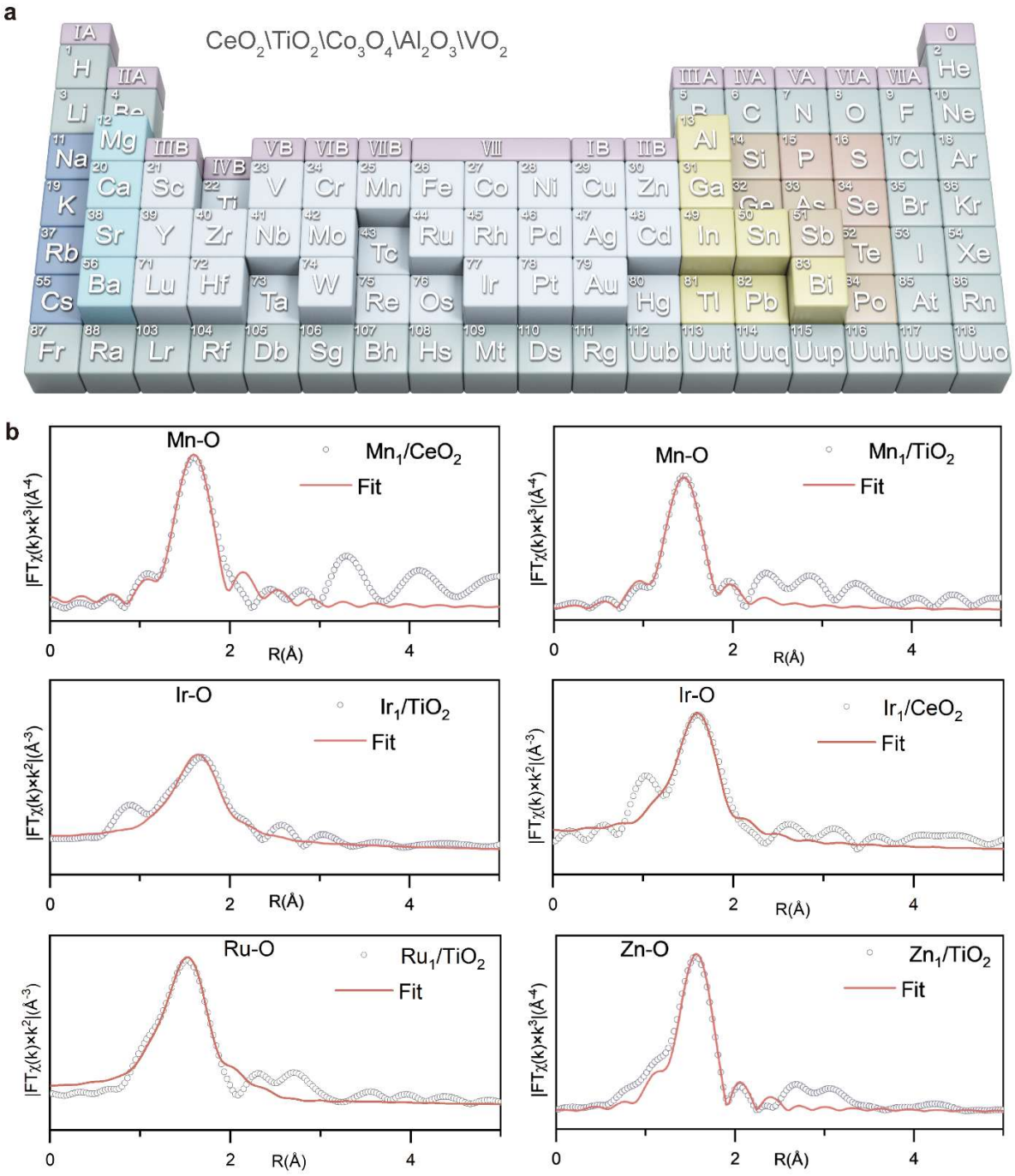

Fig. S31 Characterization of representative C-SACs. a, Periodic table showing the metals (raised parts) and supports (words in gray) that have the possibility of forming C-SACs. **b**, FT-EXAFS spectra and for C-SACs (gray) and fits (red). FT, Fourier transform.

Fig. S32 Photograph and demonstration of the 6-axisrobotic arm in high-throughput experimental workflows. a, The robotic arm showcasing its adaptability for tasks such as sample assembly, pick-and-place operations, and furnace loading/unloading. **b**, The robotic arm holding CeO_2@NF (nickel foam) and featuring a custom-fabricated metallic electrode holder with a capacity for over 100 electrodes. **c**, The robotic arm immersing CeO_2@NF into a VC solution. **d**, 3D rendering of a sample stage designed for storing electrodes. **e**, Photograph of the actual sample stage.

Fig. S33 A liquid handling robot completes the SAC loading process.

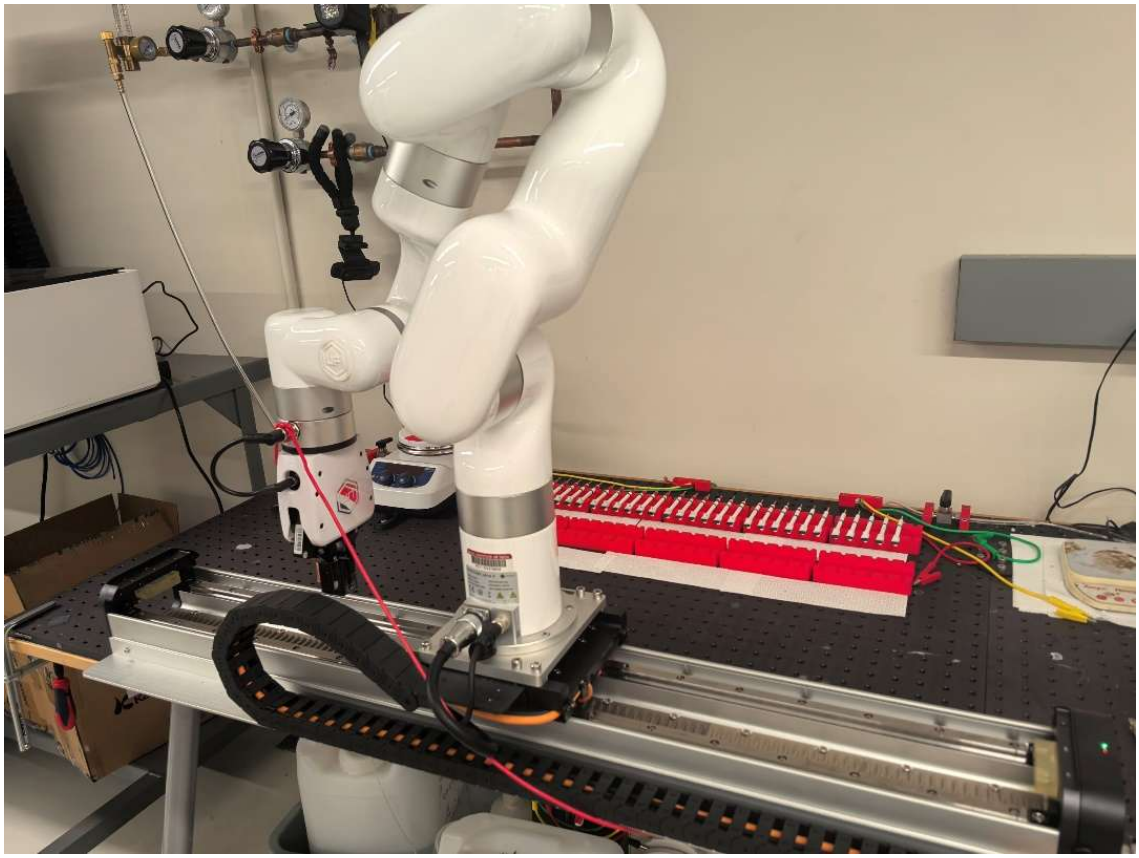

Fig. S34 A laboratory-customized high-throughput automated electrochemical performance testing system based on a 6-axis robotic arm.

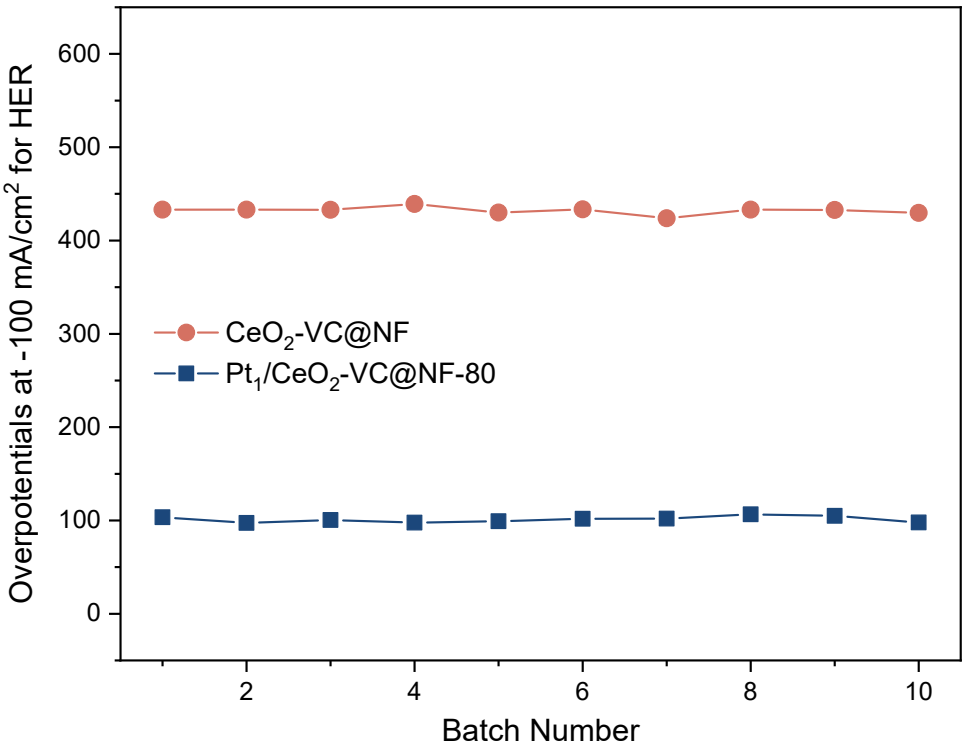

Fig. S35 Batch-to-batch reproducibility of C-SACs synthesized via robotic automation. The x-axis indicates the batch number; the y-axis represents the overpotentials at 100 mA cm^{-2} for HER, measured across ten independently synthesized batches of Pt_1/CeO_2-VC@NF-80 and CeO_2-VC@NF electrodes. The narrow variation range confirms excellent batch-to-batch consistency enabled by the robotic platform.

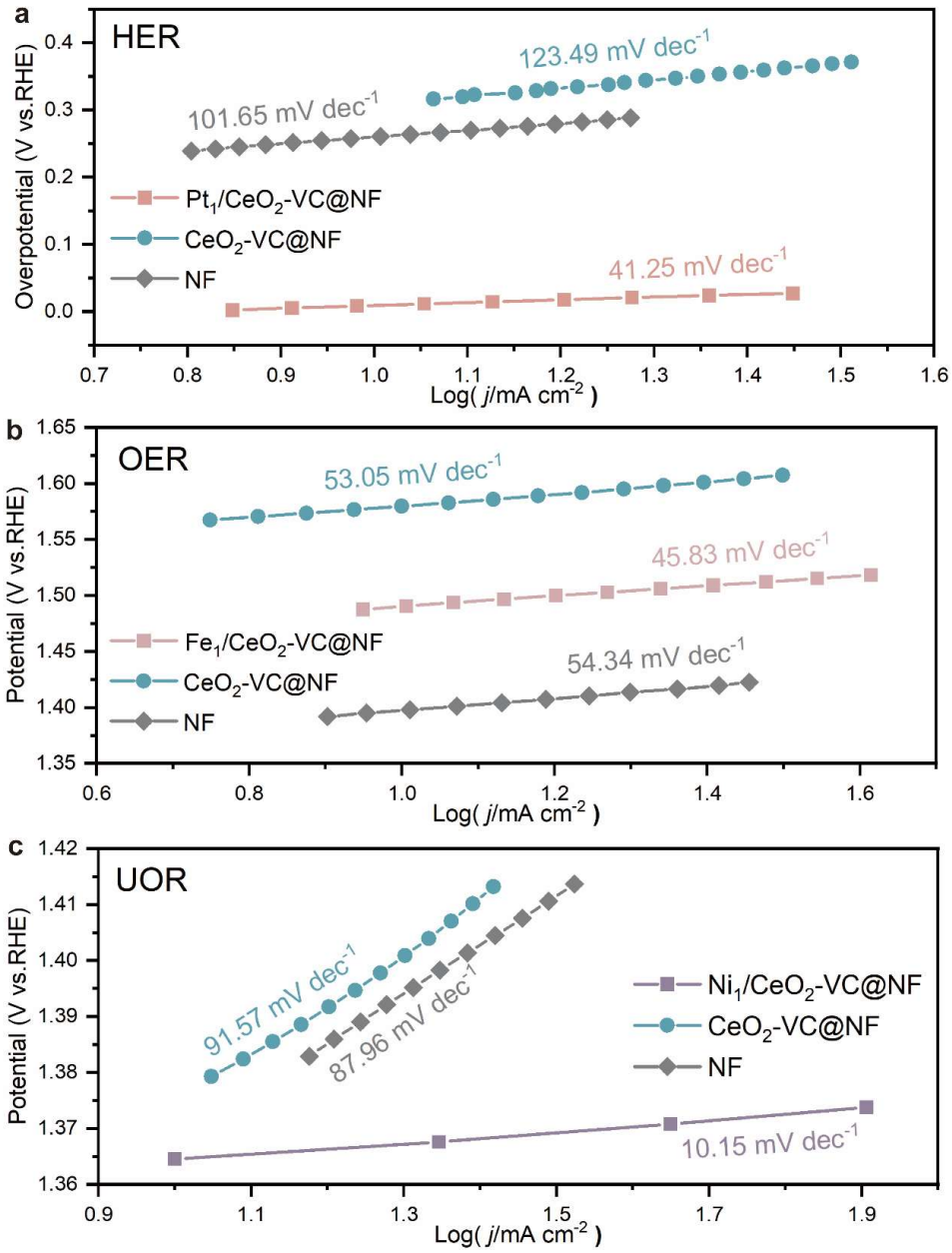

Fig. S36 Corresponding Tafel slopes obtained from the HER (a), OER (b) and UOR (c).

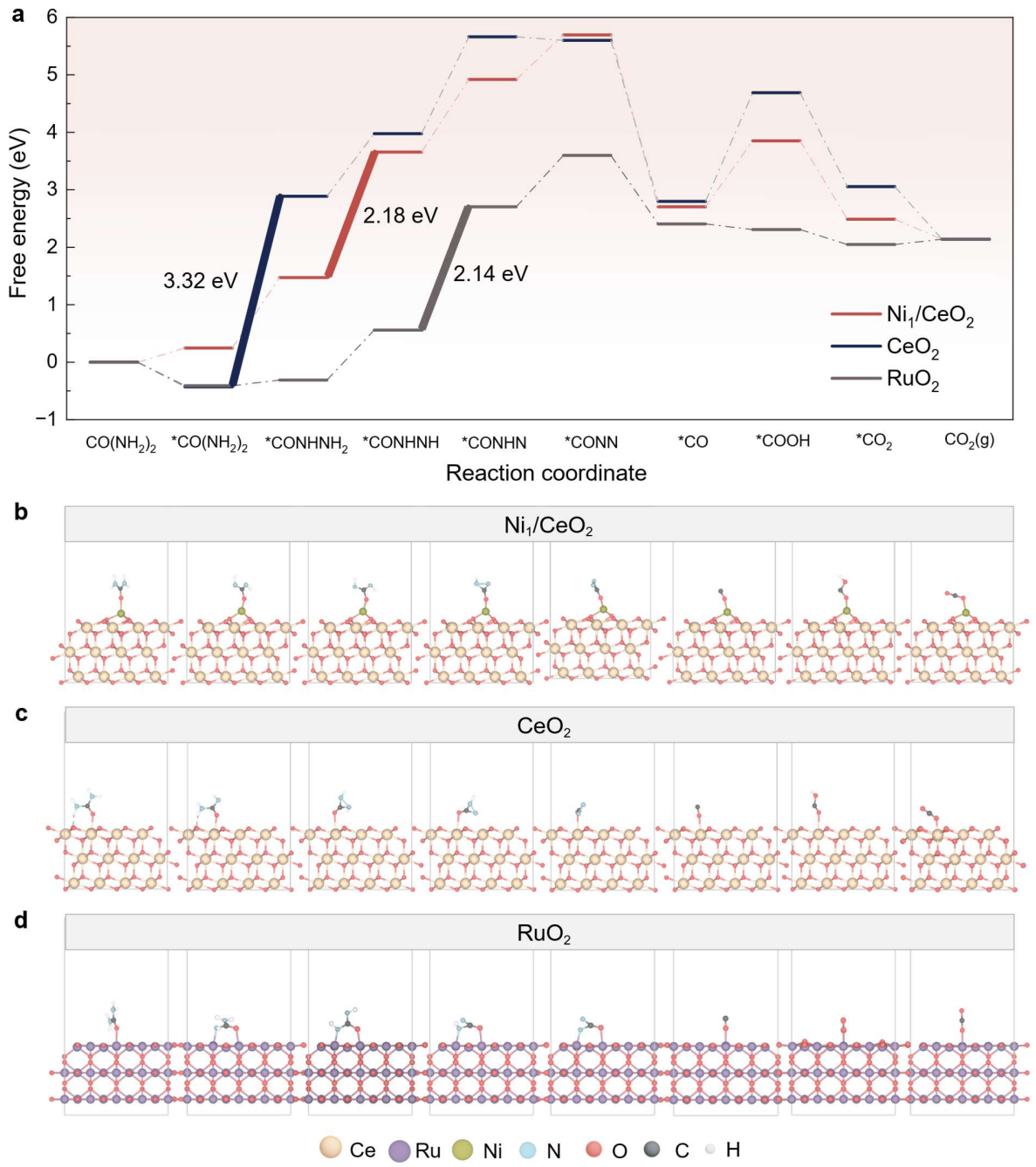

Fig. S37 DFT simulations and proposed catalytic mechanism for UOR on Ni_1/CeO_2 compared with reference catalysts. a, Calculated free energy diagrams outlining the reaction pathways and energetics for the UOR. **b–d,** Optimized atomic configurations of key reaction intermediates on Ni_1/CeO_2 (b), pristine CeO_2 (c), and benchmark RuO_2 (d) surfaces.

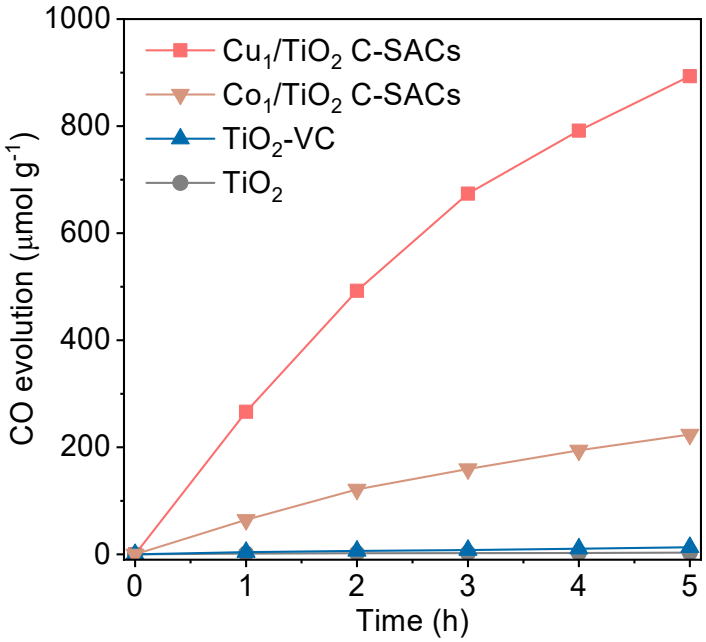

Fig. S38 Catalytic performance of representative C-SACs: Photocatalytic CO_2 reduction reaction.

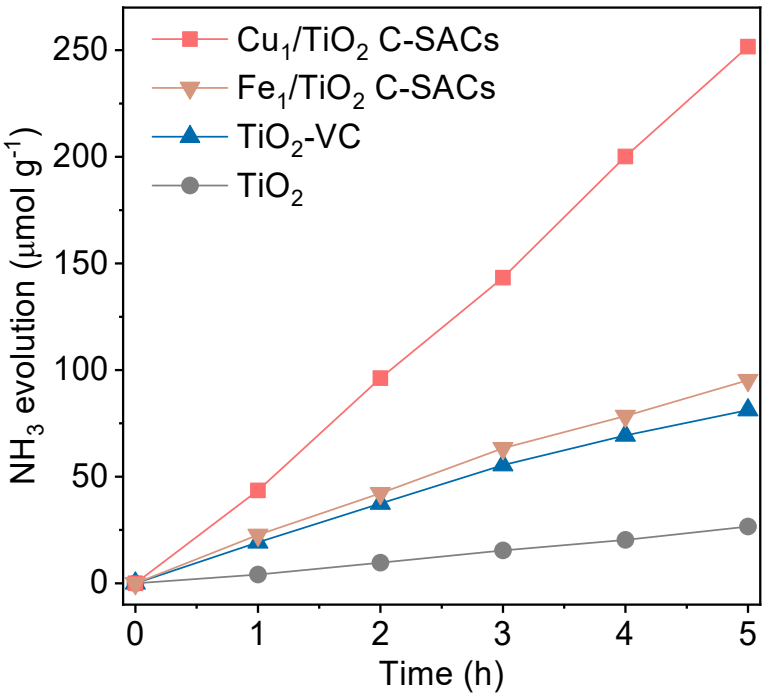

Fig. S39 Catalytic performance of representative C-SACs: Photocatalytic NO reduction reaction.

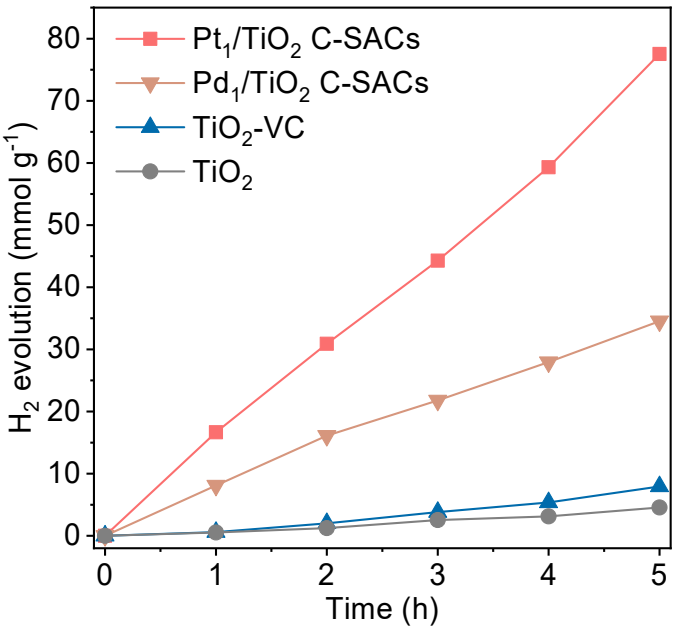

Fig. S40 Catalytic performance of representative C-SACs: Photocatalytic H_2 evolution reaction.

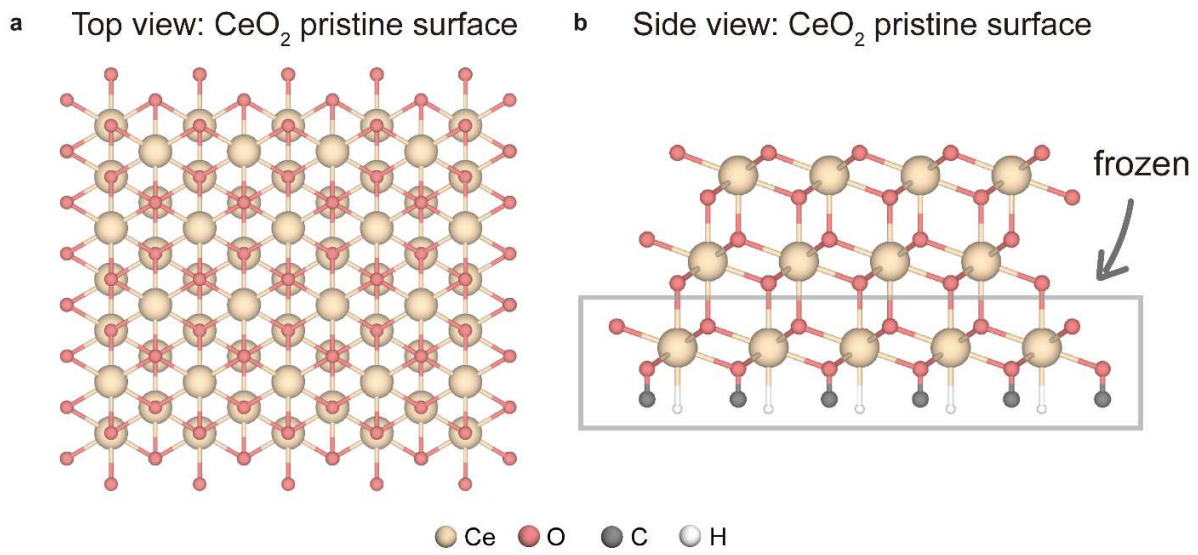

Fig. S41 Top view (a) and side view (b) of the periodic slab models for the CeO_2-(111) surface. The slab consists of three Ce layers, six O layers, and one pseudo-H layer (capping the bottom Ce/O atoms). The valence electron number of the pseudo-H atoms connected to the cerium/oxygen atoms on the bottom side of the slab is 1.5/0.5. The bottom layer of Ce, two layers of O, and the pseudo-H layer are frozen during the geometry optimizations (marked by the gray dashed frame in the side view panel). Atoms are color-coded as follows: carbon (gray), oxygen (red), hydrogen (white), and cerium (yellow).

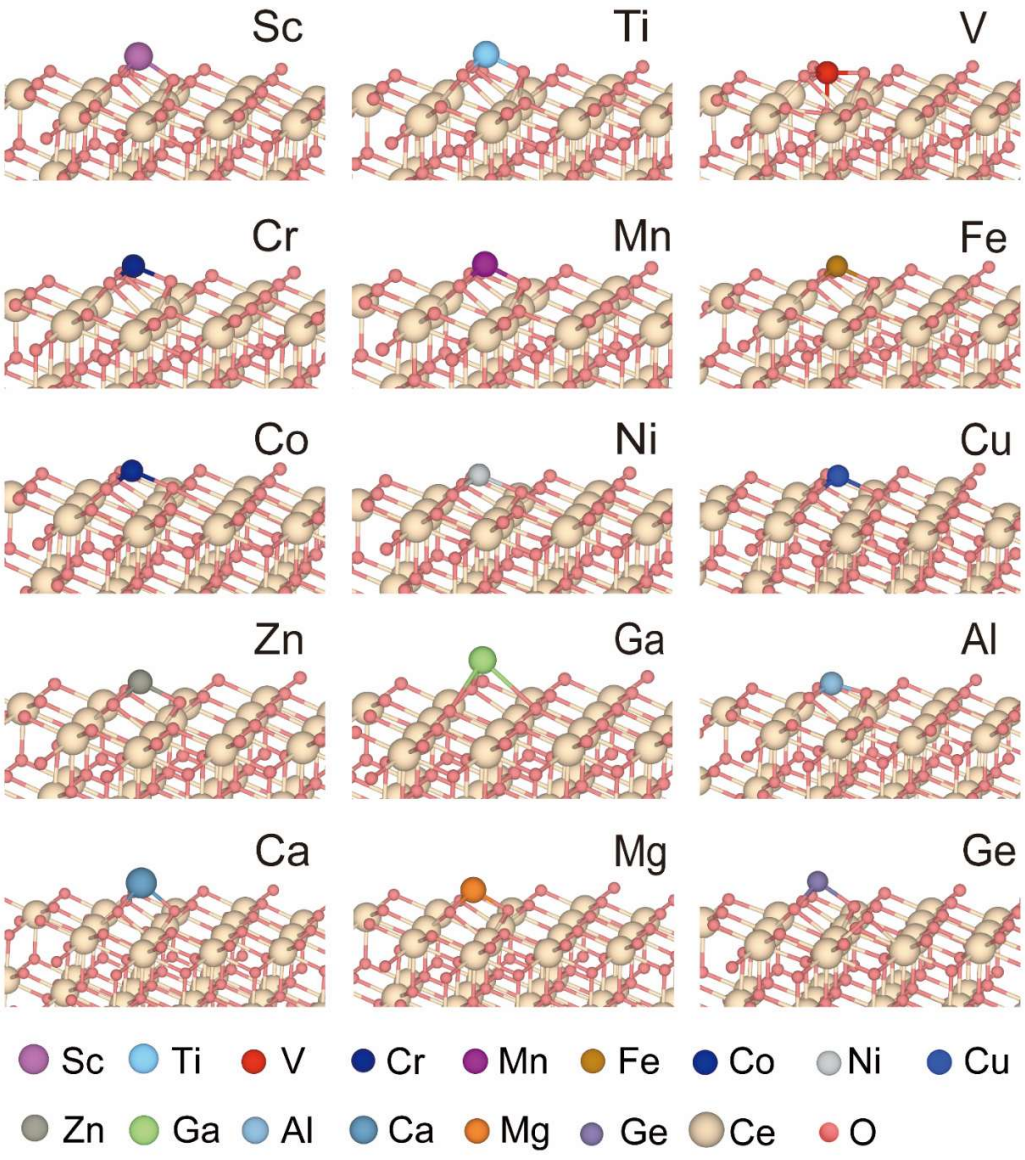

Fig. S42 Stable adsorption configurations of different single-metal atoms on the CeO_2 surface.

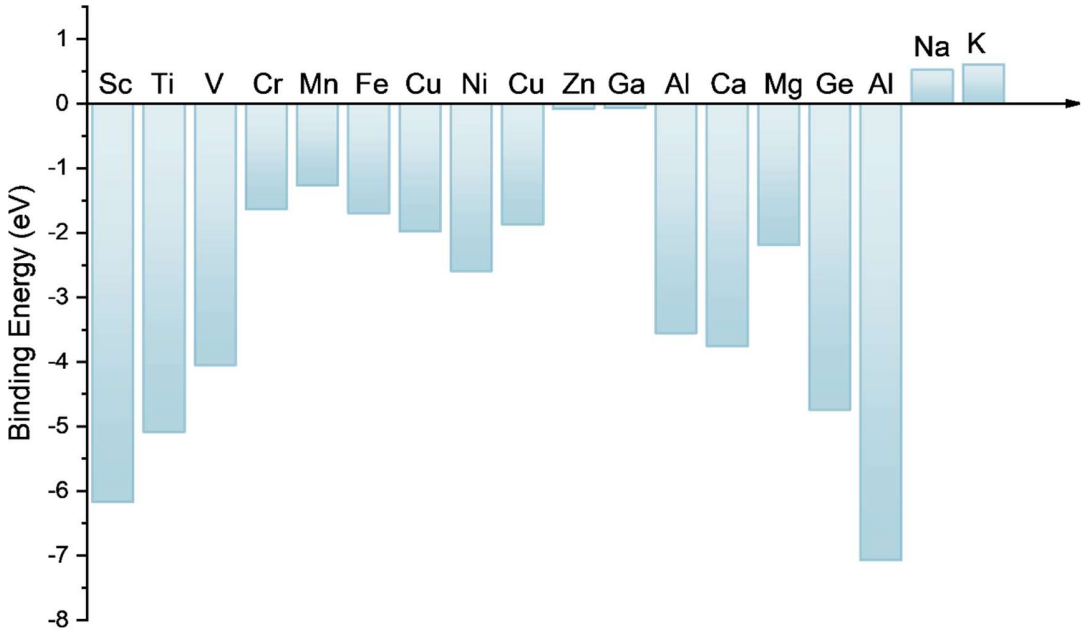

Fig. S43 Stability analysis of candidate single-atom catalysts.

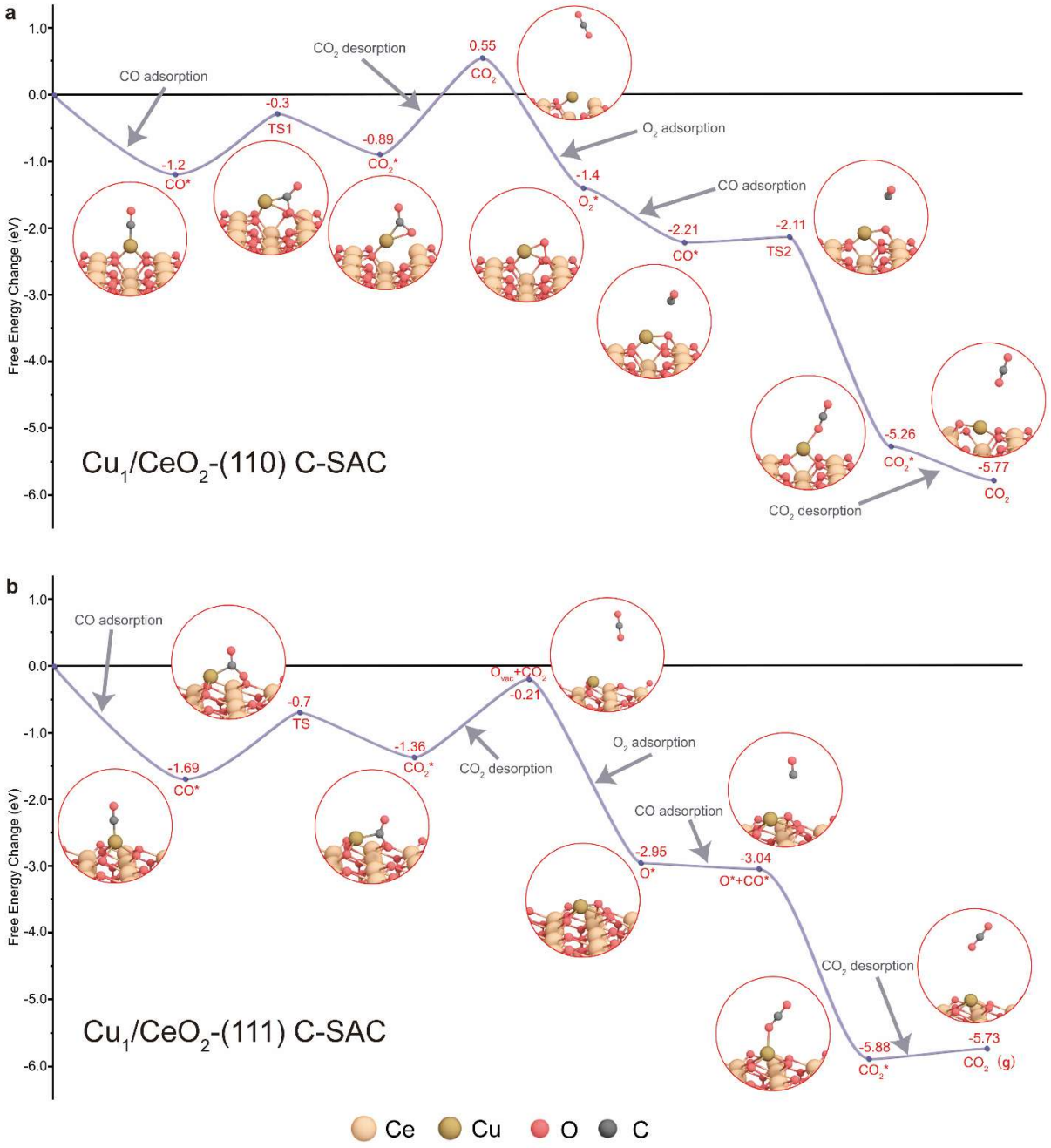

Fig. S44 Under the standard CO oxidation reaction conditions, the free energy change of the reaction. a–b, The CO_2 formation reaction pathway on the (**a**) Cu_1/CeO_2-(110) surface and (**b**) Cu_1/CeO_2-(111) surface, and inserts are the configuration of the corresponding reaction intermediates and transition states. Atoms are color-coded as follows: carbon (gray), oxygen (red), copper (brown), and cerium (yellow).

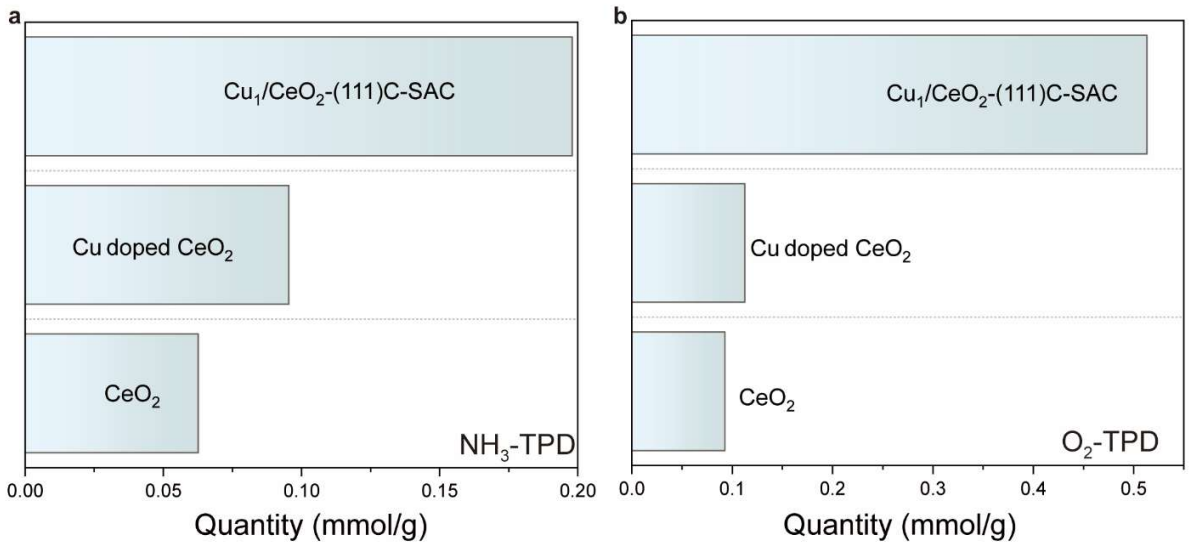

Fig. S45 a, Quantitative analysis of NH_3 temperature-programmed desorption (NH_3-TPD) profiles of Cu_1/CeO_2-(111) C-SAC, CeO_2 and Cu-doped CeO_2 catalysts. **b**, Quantitative analysis of O_2 temperature-programmed desorption (O_2-TPD) profiles of Cu_1/CeO_2-(111) C-SAC, CeO_2 and Cu-doped CeO_2 catalysts.

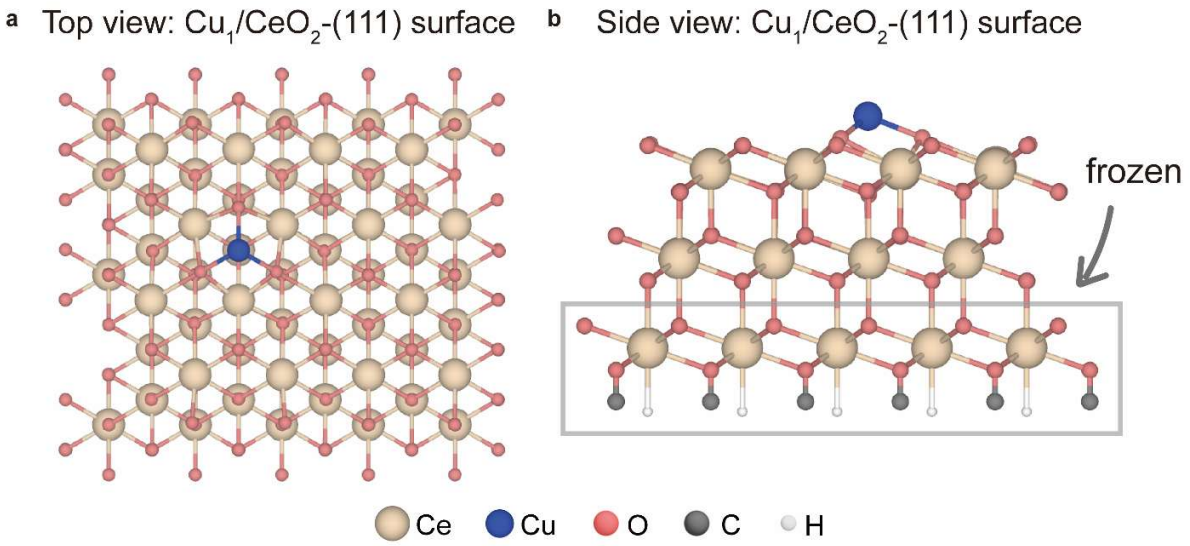

Fig. S46 The structural model of Cu_1/CeO_2-(111) C-SACs. a, Top view. **b**, Side view. Atoms are color-coded as follows: carbon (gray), oxygen (red), hydrogen (white), copper (blue), and cerium (yellow).

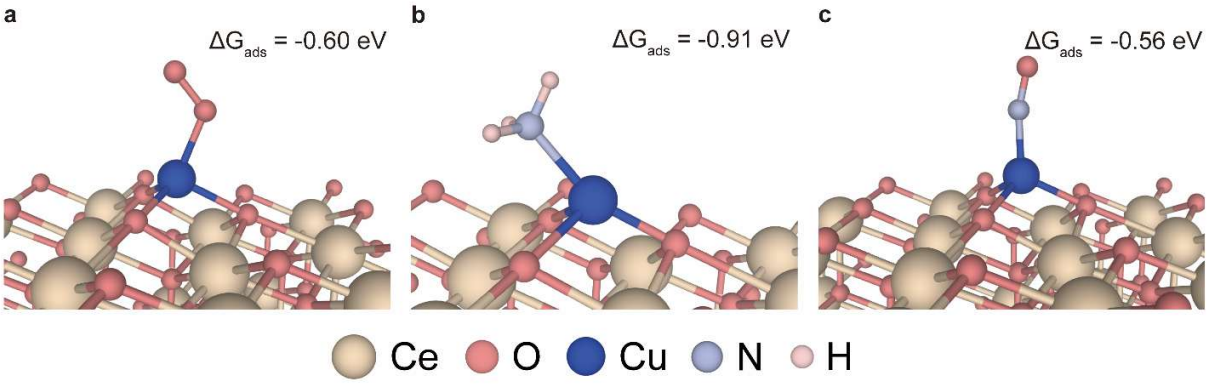

Fig. S47 The side view of the most stable configurations. a–c, Adsorption free energies and corresponding charge density difference at the Cu_1/CeO_2-(111) surface for (**a**) O_2, (**b**) NH_3 and (**c**) NO. Atoms are color-coded as follows: oxygen (red), nitrogen (light blue), hydrogen (pink), copper (blue), and cerium (yellow).

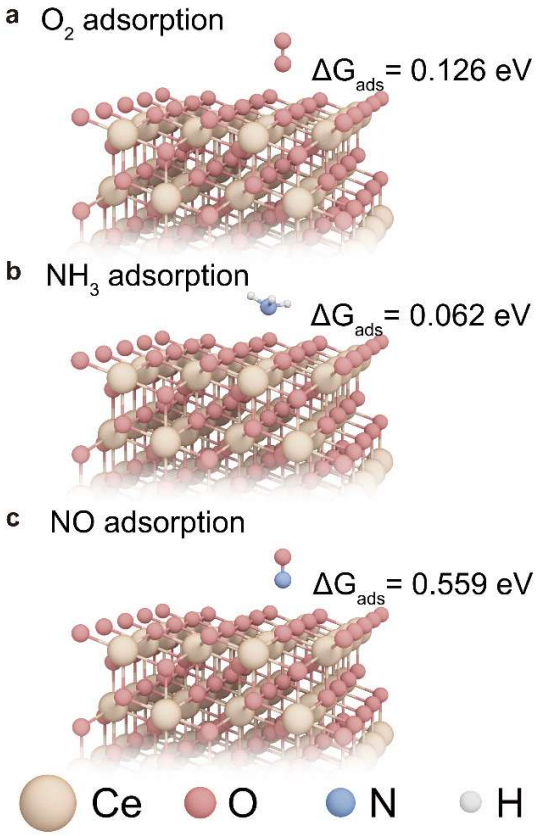

Fig. S48 The adsorbed configurations and adsorption free energies of different molecules. a–c, the adsorption free energies of (**a**) O_2, (**b**) NH_3 and (**c**) NO on CeO_2-(111) pristine surface. Atoms are color-coded as follows: oxygen (red), nitrogen (light blue), hydrogen (white), and cerium (yellow).

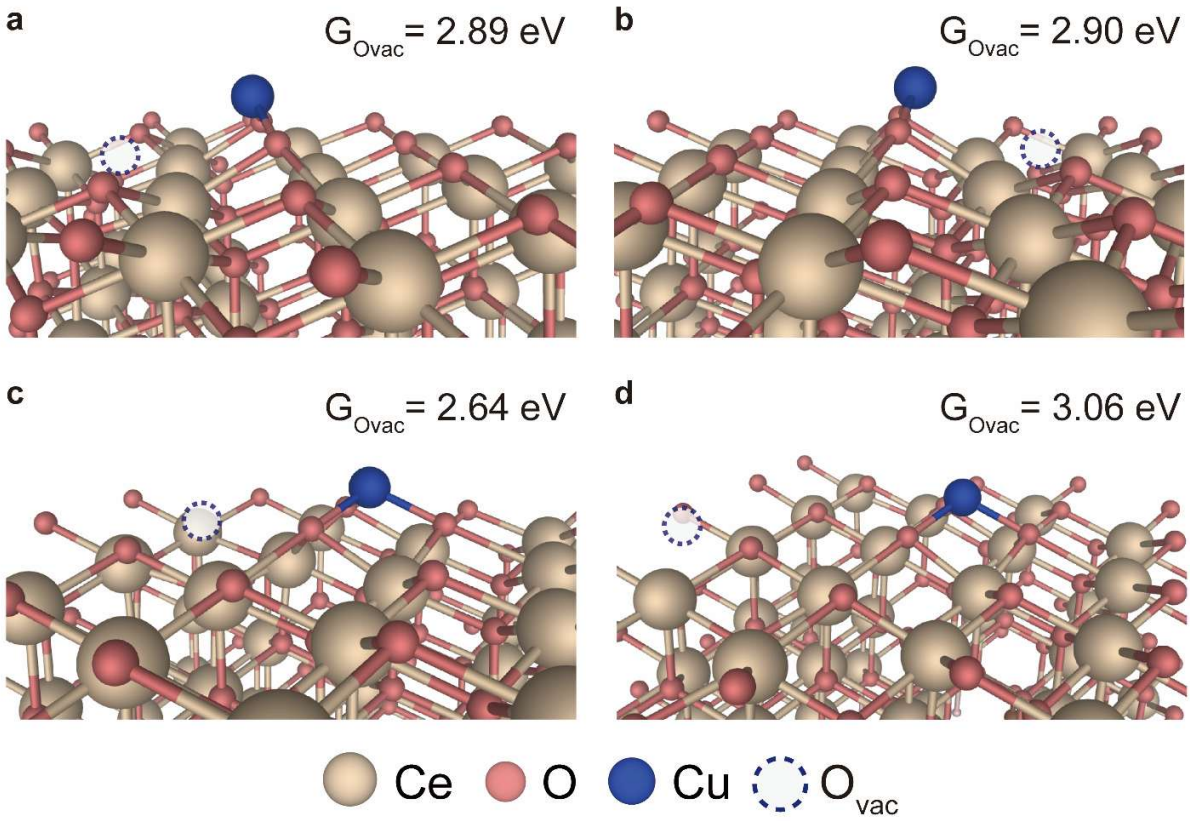

Fig. S49 Oxygen vacancy formation energies of different sites on Cu_1/CeO_2-(111) surface. a–d, represent oxygen vacancies formed at different sites. Atoms are color-coded as follows: oxygen (red), copper (blue), and cerium (yellow).

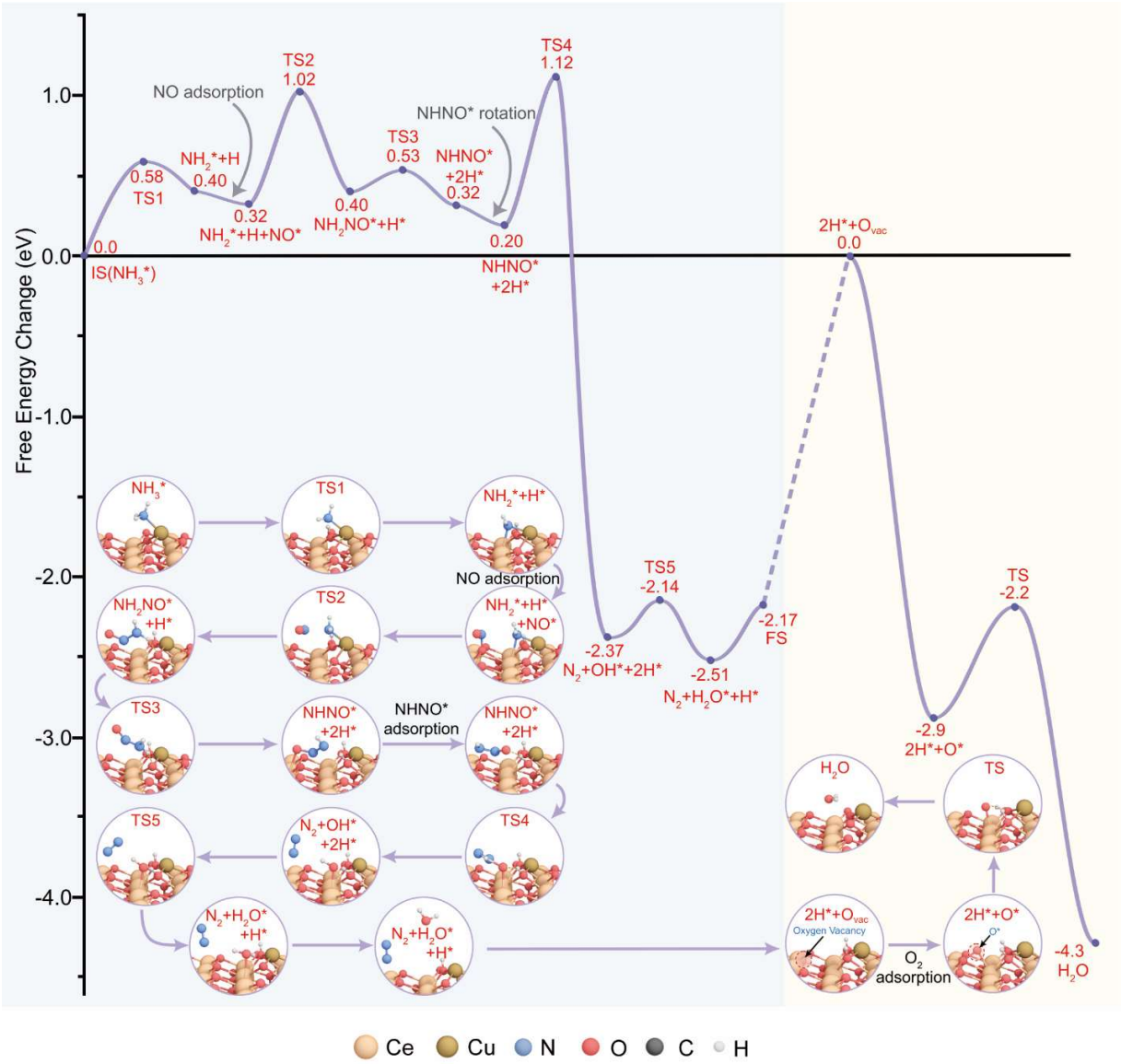

Fig. S50 Under the standard-SCR reaction conditions, the free energy change of the N_2 formation reaction pathway on the Cu_1/CeO_2-(111) surface and the configuration of the corresponding reaction intermediates and transition states. Atoms are color-coded as follows: oxygen (red), nitrogen (light blue), hydrogen (white), copper (brown), and cerium (yellow).

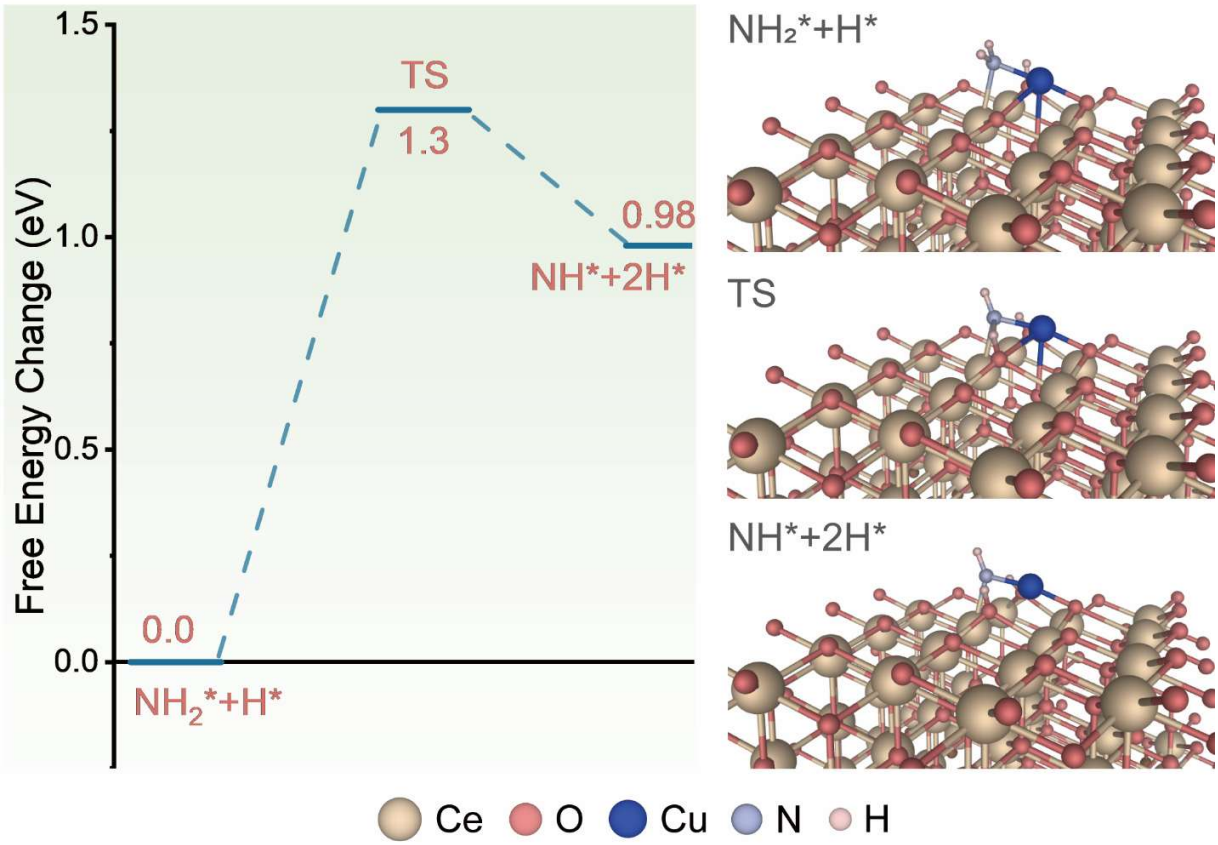

Fig. S51 The free energy change of the dissociation of NH_2^* to NH^* on the surface of Cu_1/CeO_2-(111) and the configurations of reactants, transition states and products on the reaction path. Atoms are color-coded as follows: oxygen (red), nitrogen (light blue), hydrogen (pink), copper (blue), and cerium (yellow).

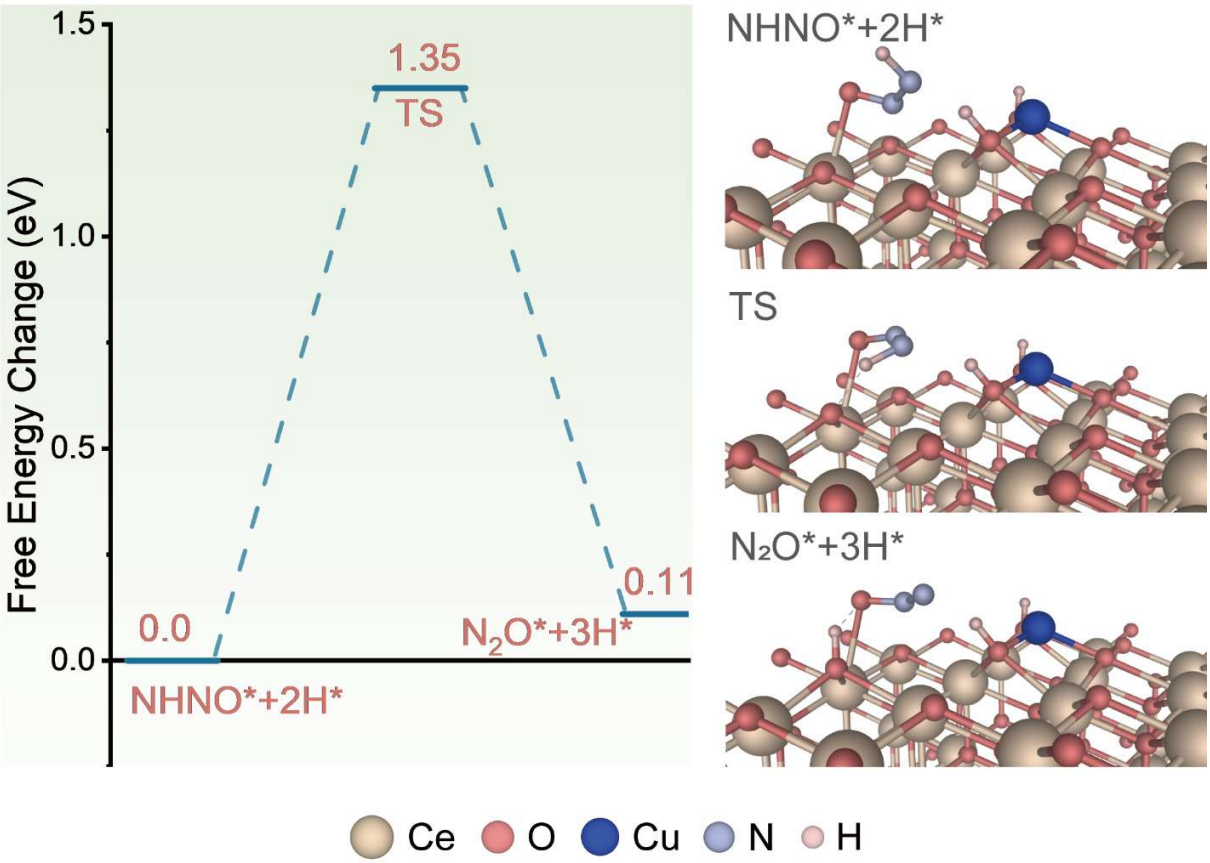

Fig. S52 The free energy change of NHNO* dissociation into N_2O and H* on the surface of Cu_1/CeO_2-(111) and the configurations of reactants, transition states and products along the reaction path. Atoms are color-coded as follows: oxygen (red), nitrogen (light blue), hydrogen (pink), copper (blue), and cerium (yellow).

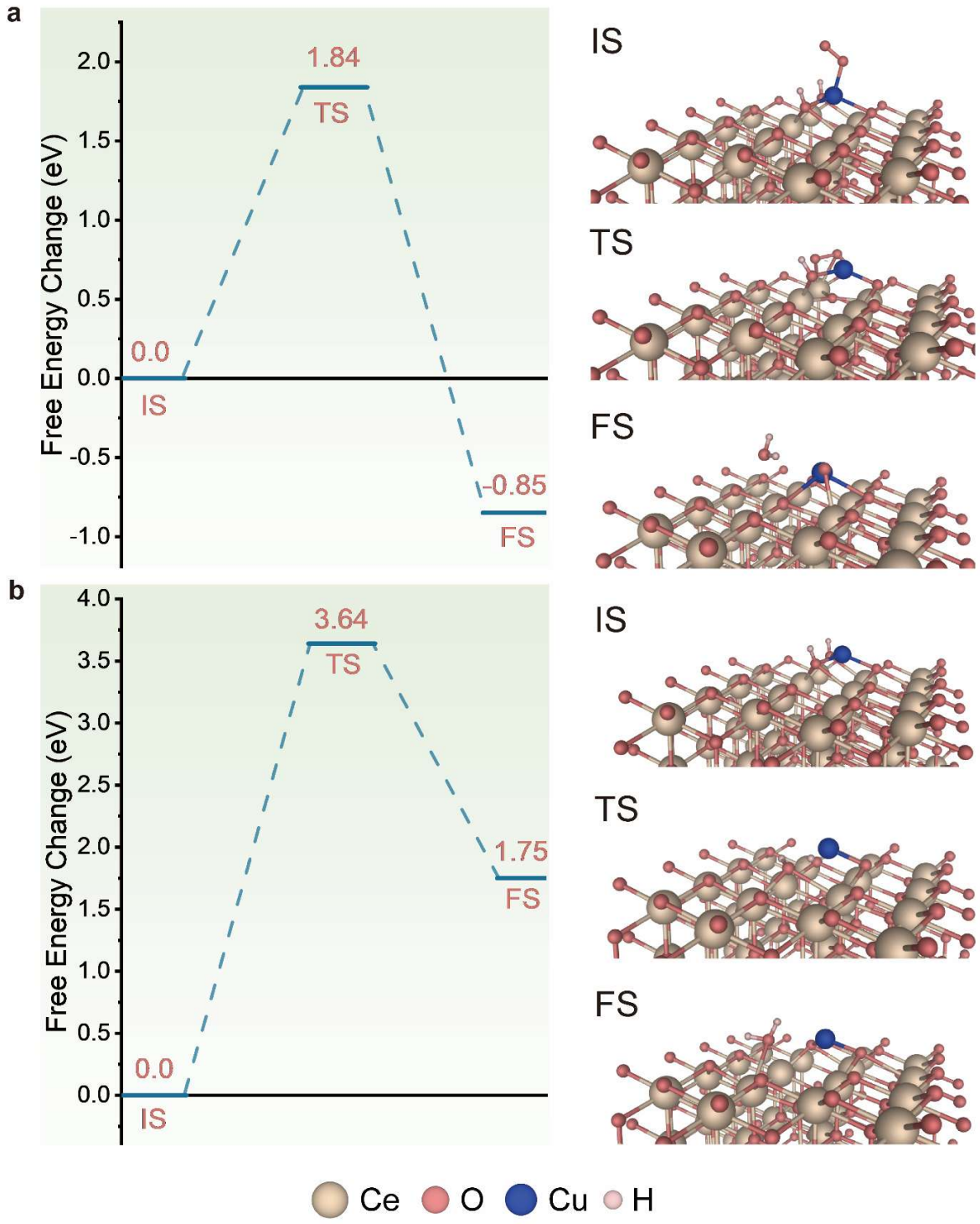

Fig. S53 Reaction pathway of surface H* removal. a–b, H* removal by (**a**) gas-phase O_2 and (**b**) lattice oxygen on the surface of Cu_1/CeO_2-(111). Atoms are color-coded as follows: oxygen (red), hydrogen (pink), copper (blue), and cerium (yellow).

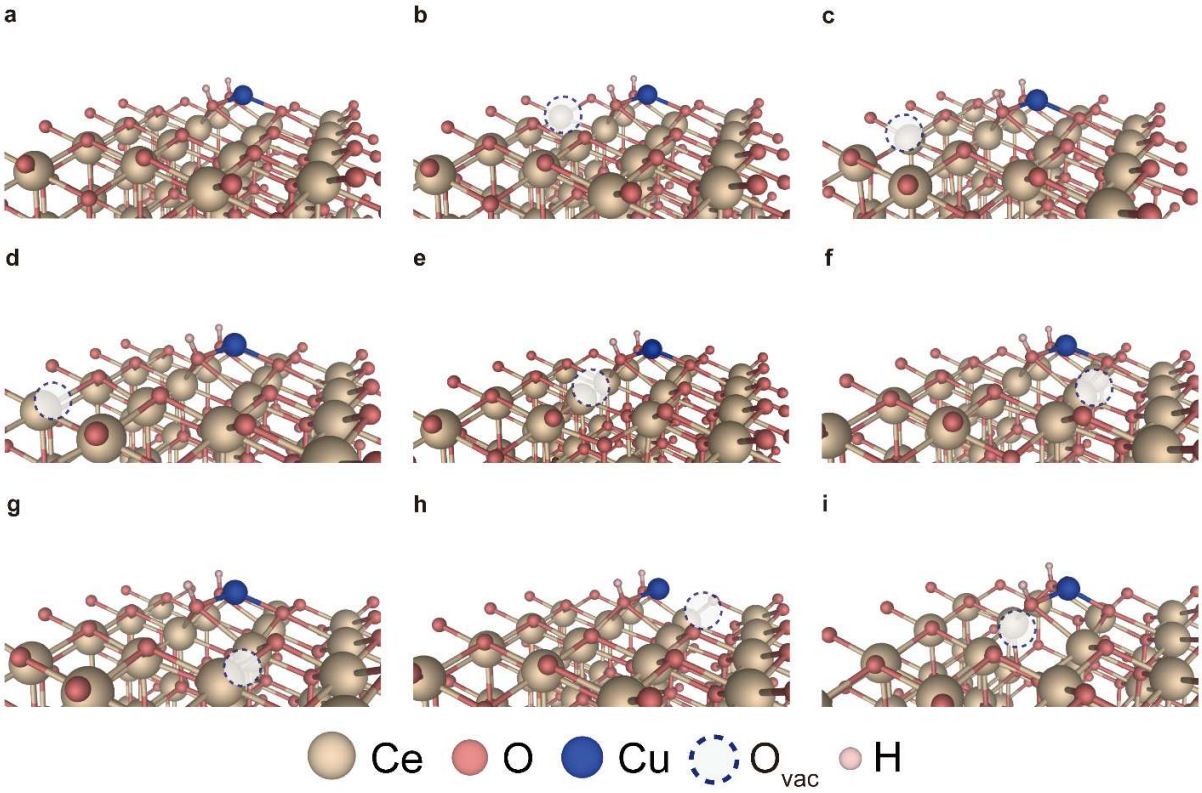

Fig. S54 Oxygen vacancy formation energies at different sites on the Cu_1/CeO_2-(111) surface covered with $2H^*$. a–i, represent oxygen vacancies formed at different sites. Atoms are color-coded as follows: oxygen (red), hydrogen (pink), copper (blue), and cerium (yellow).

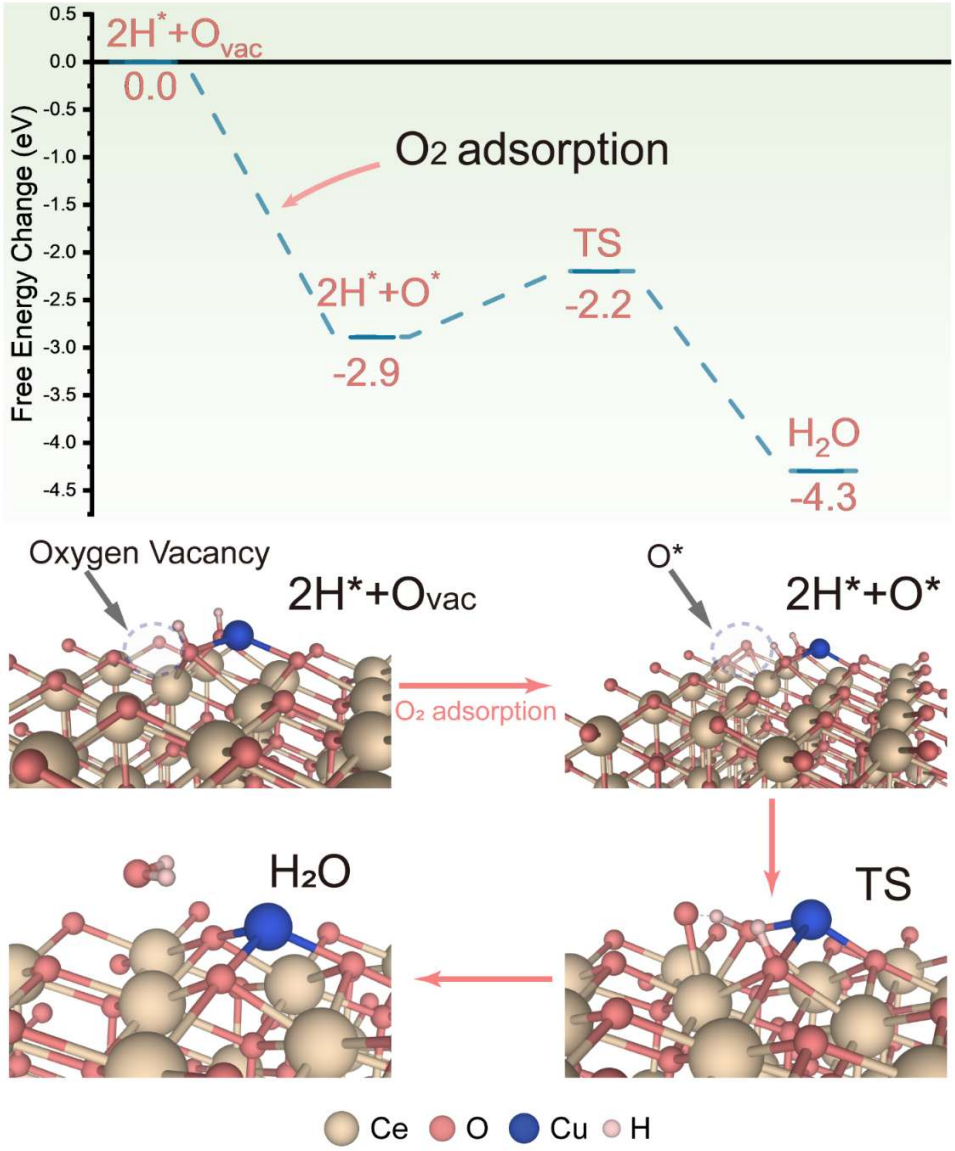

Fig. S55 Free energy change of H^* removal reaction on Cu_1/CeO_2-(111) surface and configurations of reactants, transition states and products along the reaction path. Atoms are color-coded as follows: oxygen (red), hydrogen (pink), copper (blue), and cerium (yellow).

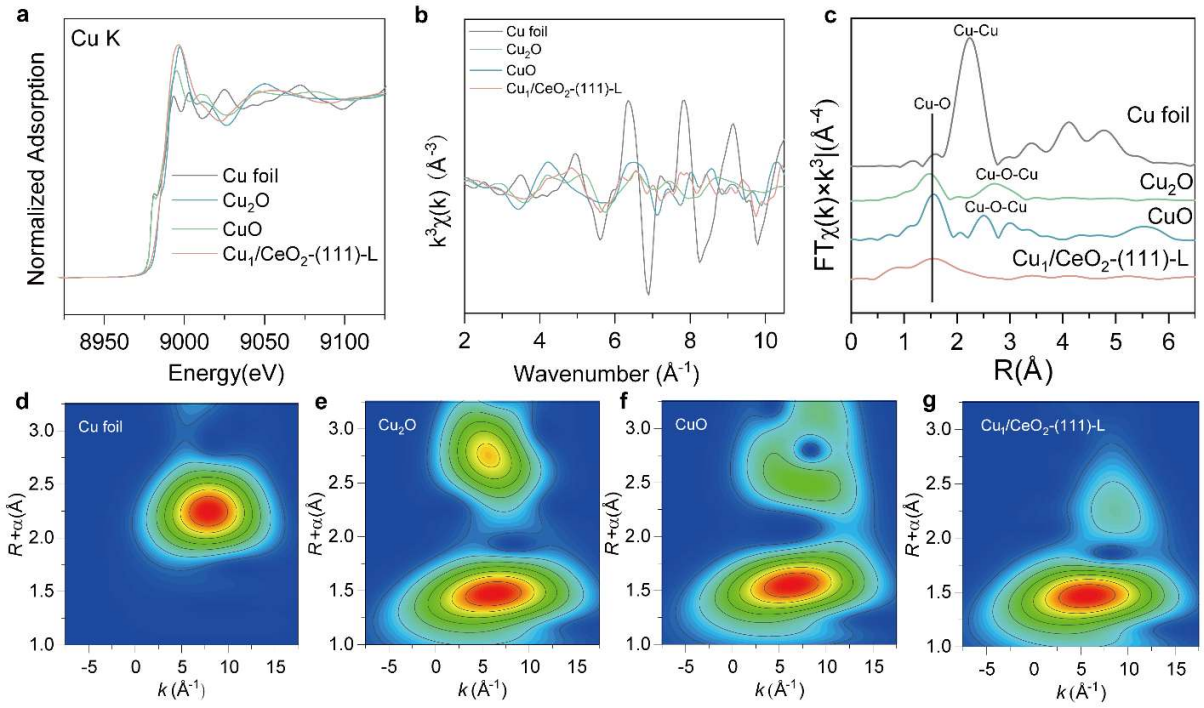

Fig. S56 Characterization of Cu_1/CeO_2-(111)-L. a, Cu K-edge XANES diagram of Cu_1/CeO_2-(111)-L catalyst and comparative samples Cu foil, Cu_2O, and CuO; **b**–**c**, K-space and R-space EXAFS map; **d**–**j**, Wavelet transform of EXAFS spectra of (**d**) Cu foil, (**e**) Cu_2O, (**f**) CuO, and (**g**) Cu_1/CeO_2-(111)-L.

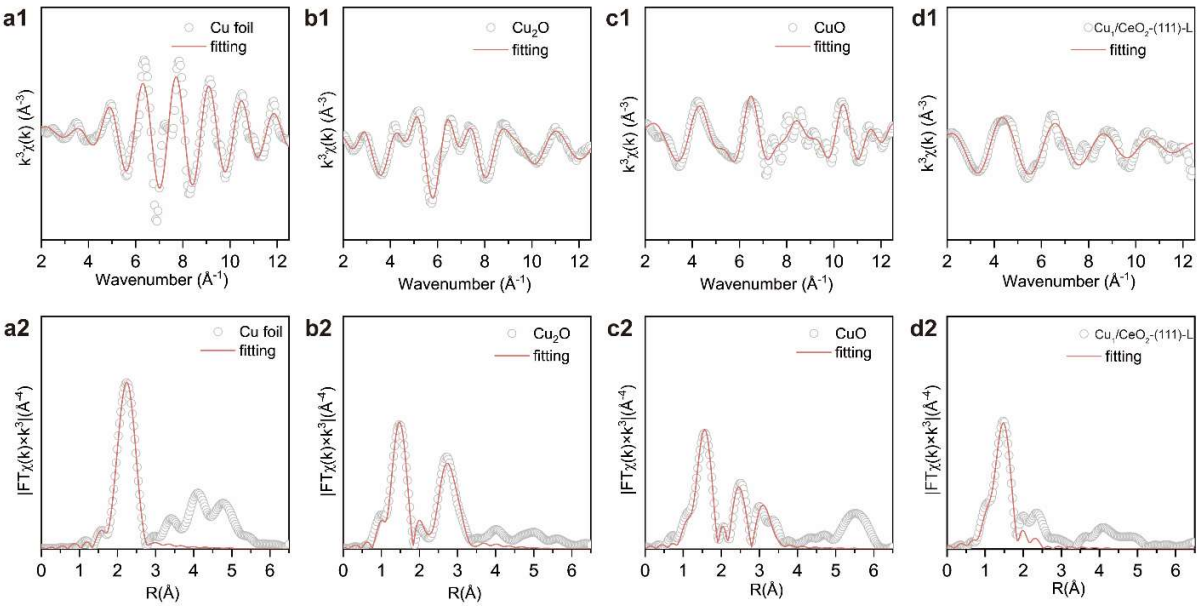

Fig. S57 The corresponding EXAFS fitting curves in R-space and in K-space. a1–d2, The EXAFS fitting curves in R-space for Cu foil (**a1**), Cu_2O (**b1**), CuO (**c1**) and Cu_1/CeO_2-(111)-L (**d1**); The EXAFS fitting curves in K-space for Cu foil (**a2**), Cu_2O (**b2**), CuO (**c2**) and Cu_1/CeO_2-(111)-L (**d2**).

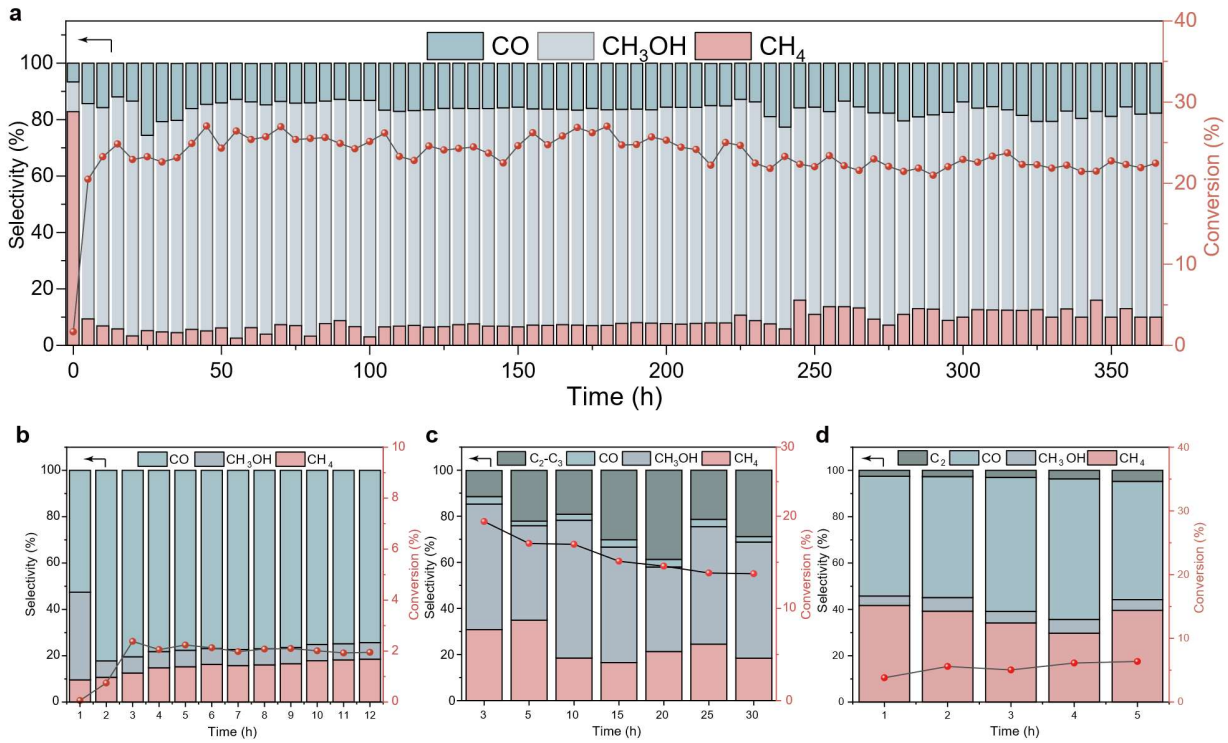

Fig. S58 Catalytic CO_2 hydrogenation performance. (a) Cu_1/CeO_2-(111)-L, (b) Cu-VC/CeO_2, (c) Cu_x/CeO_2-2 catalysts and (d) Cu/CeO_2-H_2. The reactions were conducted at 240 ℃ using a gas mixture of $CO_2/H_2/Ar$ = 24:72:4 under 3.5 MPa.

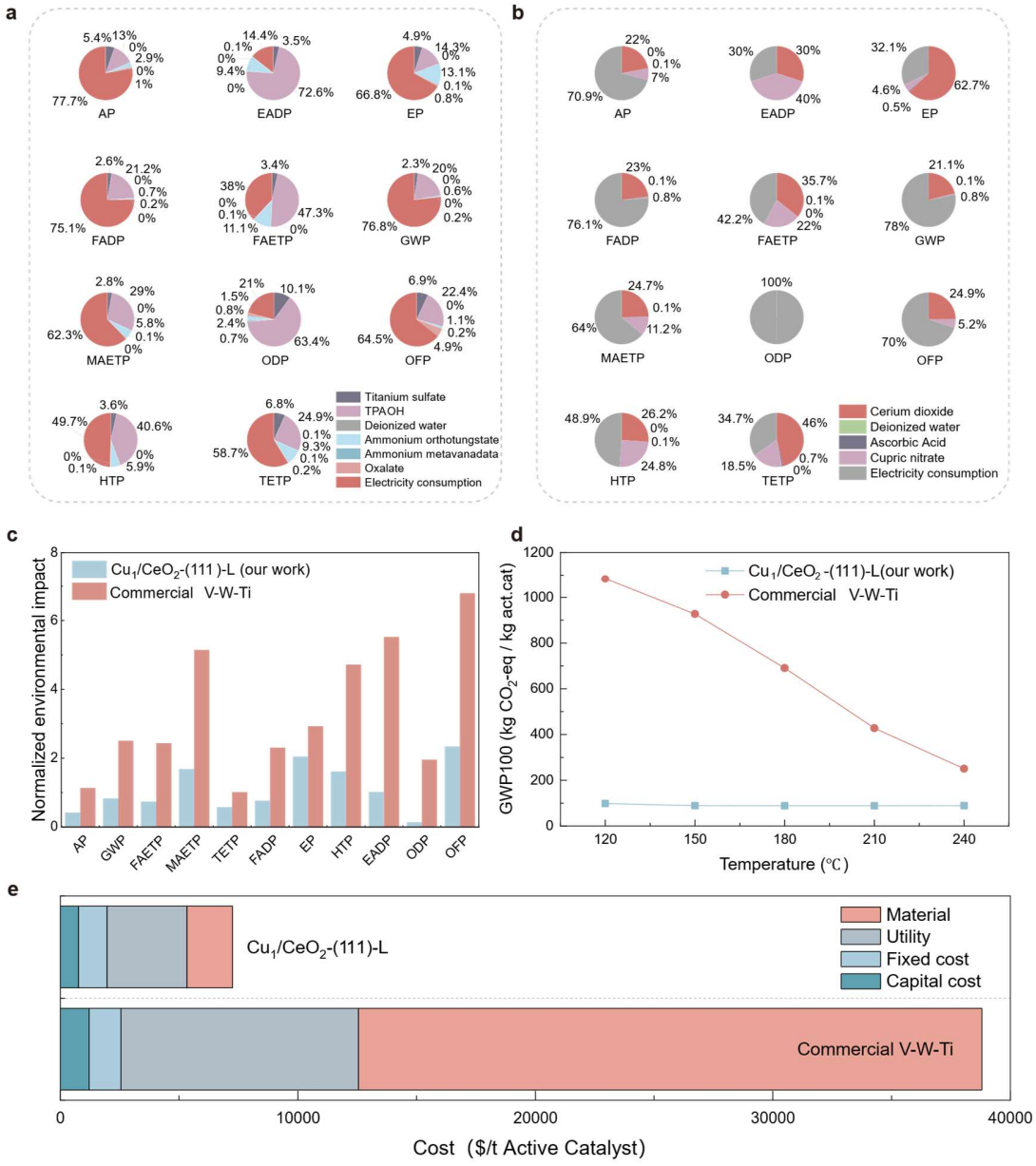

Fig. S59 Environmental impact and techno-economic analysis of Cu_1/CeO_2-(111)-L production for NH_3-SCR. a–b, LCA impact distribution associated with catalyst production for (a) commercial V-W-Ti catalysts and (b) Cu_1/CeO_2-(111)-L. **c**, Comparison of environmental impacts between the two catalyst systems based on 11 sustainability indicators: acidification, global warming potential, freshwater aquatic ecotoxicity, marine aquatic ecotoxicity, terrestrial ecotoxicity, abiotic depletion (fossil fuels), eutrophication, human toxicity, abiotic depletion (elements), ozone layer depletion, and photochemical oxidation. **d**, GWP_{100} for different catalysts across various operating temperatures. **e**, Annualized cost comparison of Cu_1/CeO_2-(111)-L and commercial V-W-Ti catalysts, normalized per ton of active catalyst. Catalyst mass is determined based on the NH_3-SCR activity and N_2 selectivity at 240 °C.

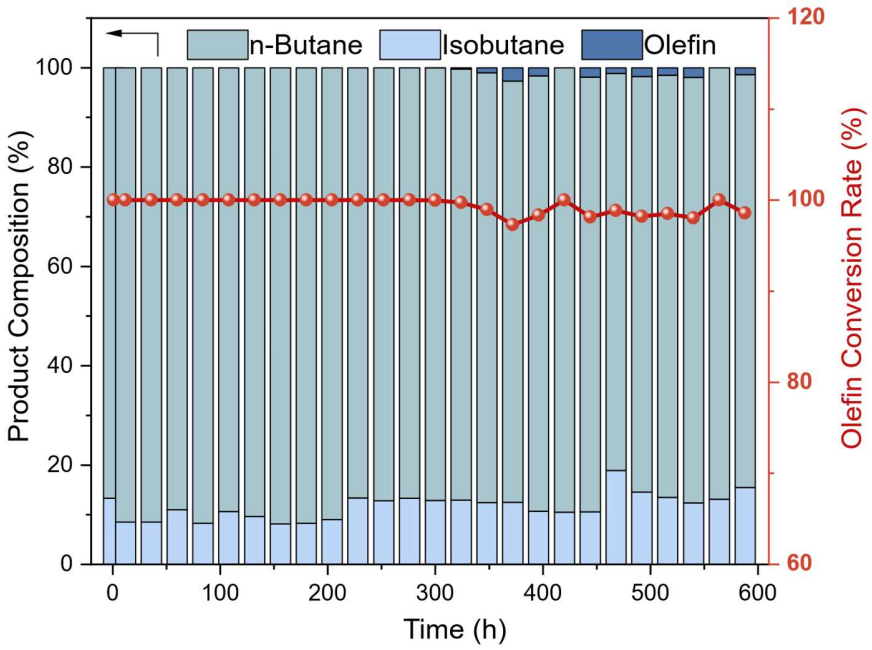

Fig. S60 Product distribution and olefin conversion performance of Ni_1/CeO_2-L C-SACs during C_4 hydrogenation. C_4 fraction obtained from the Fushun Petrochemical Olefin Plant, consisting primarily of olefins such as trans-butene, cis-butene, isobutene, and 1-butene. Hydrogenation reactions were conducted over Ni_1/CeO_2 C-SACs under the following conditions: reaction pressure of 1.5 MPa, inlet temperature of 40 °C, hydrogen flow rate of 200 mL/h, and a liquid hourly space velocity (LHSV) of 1 h^{-1} (feedstock rate: 550 mL h^{-1}).

Supplementary Tables

Table S1 Cu content in samples determined by ICP-OES.

No.	Samples	Cu (wt%)
1	Cu_1/CeO_2-(111)	4.31
2	Cu_1/CeO_2-(110)	4.93
3	Cu_x/CeO_2-1	0.82
4	Cu_x/CeO_2-2	4.83
5	Cu-doped CeO_2	3.11
6	Cu-VC/CeO_2	0.045

Table S2 Reliability factors for points with Bragg contributions of Fig. 3c and Fig. S7

Samples	Lattice parameter (Å)	Cell volume ($Å^3$)	Rwp
Cu_1/CeO_2-(111)	5.4113	158.458	0.78%
Cu_1/CeO_2-(110)	5.4277	159.900	1.91%
CeO_2-(111)	5.4119	158.509	2.46%
CeO_2-(111)-VC	5.4120	158.514	1.88%
Cu-doped CeO_2	5.4111	158.443	2.52%

Table S3 Summary of synthesized C-SACs.

Nb.	Support	Auxiliary	Single-Atom
1	CeO_2	VC	V
2	CeO_2	VC	Cr
3	CeO_2	VC	Mn
4	CeO_2	VC	Fe
5	CeO_2	VC	Co
6	CeO_2	VC	Ni
7	CeO_2	VC	Cu
8	CeO_2	VC	Zn
9	CeO_2	VC	Mo
10	CeO_2	VC	Ru
11	CeO_2	VC	Pt
12	CeO_2	VC	Ir
13	CeO_2	VC	Al
14	CeO_2	VC	Ca
15	CeO_2	VC	Sc
16	CeO_2	VC	Ga
17	CeO_2	VC	Sr
18	CeO_2	VC	Y
19	CeO_2	VC	Zr
20	CeO_2	VC	Nb
21	CeO_2	VC	Mo
22	CeO_2	VC	Rh
23	CeO_2	VC	Ag
24	CeO_2	VC	Cd
25	CeO_2	VC	In
26	CeO_2	VC	Sn
27	CeO_2	VC	Sb
28	CeO_2	VC	Ba
29	CeO_2	VC	Lu
30	CeO_2	VC	Hf
31	CeO_2	VC	W
32	CeO_2	VC	Au
33	CeO_2	VC	Bi
34	CeO_2	VC	Pd
35	CeO_2	VC	Pd
36	CeO_2	VC	Pd

37	CeO_2	VC	Pd
38	CeO_2	VC	Pt
39	CeO_2	VC	Pt
40	CeO_2	VC	Pt
41	CeO_2	VC	Pt
42	CeO_2	VC	V
43	CeO_2	VC	Cr
44	CeO_2	VC	Mn
45	CeO_2	VC	Fe
46	CeO_2	VC	Co
47	CeO_2	VC	Ni
48	CeO_2	VC	Cu
49	CeO_2	VC	Zn
50	CeO_2	VC	Mo
51	CeO_2	VC	Ru
52	CeO_2	VC	Pt
53	CeO_2	VC	Ir
54	TiO_2	VC	V
55	TiO_2	VC	Cr
56	TiO_2	VC	Mn
57	TiO_2	VC	Fe
58	TiO_2	VC	Co
59	TiO_2	VC	Ni
60	TiO_2	VC	Cu
61	TiO_2	VC	Zn
62	TiO_2	VC	Mo
63	TiO_2	VC	Ru
64	TiO_2	VC	Pt
65	TiO_2	VC	Ir
66	TiO_2	VC	V
67	TiO_2	VC	Cr
68	TiO_2	VC	Mn
69	TiO_2	VC	Fe
70	TiO_2	VC	Co
71	TiO_2	VC	Ni
72	TiO_2	VC	Cu
73	TiO_2	VC	Zn
74	TiO_2	VC	Mo

75	TiO_2	VC	Ru
76	TiO_2	VC	Pt
77	TiO_2	VC	Ir
78	Al_2O_3	VC	Cu
79	Al_2O_3	VC	Ru
80	Al_2O_3	VC	Pt
81	MgAl-LDH	VC	Cu
82	MgAl-LDH	VC	Ru
83	MgAl-LDH	VC	Pt
84	NiAl-LDH	VC	Cu
85	NiAl-LDH	VC	Ru
86	NiAl-LDH	VC	Pt
87	NiFe-LDH	VC	Cu
88	NiFe-LDH	VC	Ru
89	NiFe-LDH	VC	Pt
90	WO_3	VC	Cu
91	WO_3	VC	Ru
92	WO_3	VC	Pt
93	VO_2	VC	Cu
94	VO_2	VC	Ru
95	VO_2	VC	Pt
96	CeO_2	GSH	Pt
97	CeO_2	GSH	Cu
98	VO_2	GSH	Pt
99	VO_2	GSH	Cu
100	TiO_2	GSH	Pt
101	TiO_2	GSH	Cu
102	CeO_2	NAC	Pt
103	CeO_2	NAC	Cu
104	VO_2	NAC	Pt
105	VO_2	NAC	Cu
106	TiO_2	NAC	Pt
107	TiO_2	NAC	Cu

Table S4 Statistical results for batch-to-batch consistency.

Statistic	Pt_1/CeO_2-VC@NF-80	CeO_2-VC@NF
Mean (mV)	101.12	432.12
Median (mV)	101.08	433.02
Std. Dev. (mV)	3.21	3.85
Min (mV)	97.38	423.92

Table S5. Comparison of overpotentials at 100 mA cm^{-2} for HER catalysts screened from the clicking single-atom library. This table summarizes the HER catalyst samples tested using an automated robotic system. The numerical suffix following each sample identifier indicates the volume (in μL) of a 50 mM precursor solution in ethanol deposited onto the support surface by the *Opentrons Flex* workstation. Using the fully automated robotic evaluation system, the Pt_1CeO_2-VC@NF-80 sample, screened from a total of 57 candidates, demonstrated the best performance. Samples with excessively high overpotentials or failed measurements are marked as "–" in the Overpotential (mV) column.

Serial number	Catalysts	Overpotential (mV)
1	Pt_1CeO_2-VC@NF-20	140.47
2	Pt_1CeO_2-VC@NF-40	100.43
3	Pt_1CeO_2-VC@NF-60	97.38
4	Pt_1CeO_2-VC@NF-80	48.39
5	Pt_1CeO_2-VC@NF-100	73.05
6	CeO_2-VC@NF	-
7	Fe_1CeO_2-VC@NF-20	414.65
8	Fe_1CeO_2-VC@NF-40	420.83
9	Fe_1CeO_2-VC@NF-60	381.55
10	Fe_1CeO_2-VC@NF-100	426.90
11	Co_1CeO_2-VC@NF-20	433.05
12	Co_1CeO_2-VC@NF-40	393.11
13	Mn_1CeO_2-VC@NF-20	414.61
14	Mn_1CeO_2-VC@NF-40	417.64
15	Mn_1CeO_2-VC@NF-60	433.08
16	Mn_1CeO_2-VC@NF-80	-
17	Mn_1CeO_2-VC@NF-100	433.13
18	Ru_1CeO_2-VC@NF-20	386.86
19	Ru_1CeO_2-VC@NF-40	386.91
20	Ru_1CeO_2-VC@NF-60	414.63
21	Ru_1CeO_2-VC@NF-80	399.17
22	Ru_1CeO_2-VC@NF-100	380.73
23	Ir_1CeO_2-VC@NF-20	389.94
24	Ir_1CeO_2-VC@NF-40	348.96
25	Ir_1CeO_2-VC@NF-60	353.37
26	Ir_1CeO_2-VC@NF-80	365.26
27	Ir_1CeO_2-VC@NF-100	386.93
28	$Co_1Mn_1Pt_1Ru_1Ir_1CeO_2$-VC@NF-40	118.87
29	Fe_1@NF-40	353.11
30	Pt_1@NF-40	251.48

31	$Ni_1Mo_1CeO_2$@NF-40	411.36
32	Fe_1-VC@NF-20	346.92
33	Fe_1-VC@NF-60	343.85
34	Pt_1-VC@NF-20	220.17
35	Pt_1-VC@NF-40	146.61
36	Pt_1-VC@NF-60	106.62
37	Pt_1-VC@NF-80	85.00
38	Pt_1-VC@NF-100	103.45
39	Ni_1CeO_2-VC@NF-40	424.01
40	$Ni_1Co_1CeO_2$-VC@NF-40	417.47
41	$Co_1Mo_1CeO_2$-VC@NF-40	405.17
42	Cu_1-VC@NF-100	389.61
43	Co_1-VC@NF-100	389.64
44	Ni_1-VC@NF-100	389.62
45	Au_1-VC@NF-100	352.70
46	Ir_1-VC@NF-100	386.53
47	Ru_1-VC@NF-100	380.38
48	In_1-VC@NF-100	380.33
49	Mn_1-VC@NF-100	387.20
50	Zn_1-VC@NF-100	383.48
51	Mo_1-VC@NF-100	392.68
52	V_1-VC@NF-100	399.40
53	Sn_1-VC@NF-100	392.70
54	Ce_1-VC@NF-100	429.67
55	Yb_1-VC@NF-100	414.85
56	La_1-VC@NF-100	380.28
57	Ta_1-VC@NF-100	377.30

Table S6. Comparison of overpotentials at 100 mA cm^{-2} for OER catalysts screened from the clicking single-atom library. This table summarizes the OER catalyst samples tested using an automated robotic system. The numerical suffix following each sample identifier indicates the volume (in μL) of a 50 mM precursor solution in ethanol deposited onto the support surface by the *Opentrons Flex* workstation. For samples 57–66, the suffix "-2h" indicates that the samples underwent a 2-hour immersion in a VC solution. Using the fully automated robotic evaluation system, the Fe_1CeO_2-VC@NF-80 sample, screened from a total of 66 candidates, demonstrated the best performance. Samples with excessively high overpotentials or failed measurements are marked as "–" in the Overpotential (mV) column.

Serial number	Catalysts	Overpotential (mV)
1	Fe_1CeO_2-VC@NF-20	336.95
2	Fe_1CeO_2-VC@NF-40	328.32
3	Fe_1CeO_2-VC@NF-60	312.94
4	Fe_1CeO_2-VC@NF-80	306.77
5	Fe_1CeO_2-VC@NF-100	309.88
6	CeO_2-VC@NF-0	-
7	Co_1CeO_2-VC@NF-20	334.53
8	Co_1CeO_2-VC@NF-40	331.45
9	Co_1CeO_2-VC@NF-60	334.46
10	Co_1CeO_2-VC@NF-80	331.50
11	Co_1CeO_2-VC@NF-100	337.64
12	Mn_1CeO_2-VC@NF-20	346.43
13	Mn_1CeO_2-VC@NF-40	349.66
14	Mn_1CeO_2-VC@NF-60	349.30
15	Mn_1CeO_2-VC@NF-80	346.54
16	Mn_1CeO_2-VC@NF-100	352.98
17	Ru_1CeO_2-VC@NF-20	362.28
18	Ru_1CeO_2-VC@NF-40	377.36
19	Ru_1CeO_2-VC@NF-60	-
20	Ru_1CeO_2-VC@NF-80	-
21	Ru_1CeO_2-VC@NF-100	-
22	Pt_1CeO_2-VC@NF-20	-
23	Pt_1CeO_2-VC@NF-40	328.41
24	Pt_1CeO_2-VC@NF-60	337.21
25	Pt_1CeO_2-VC@NF-80	346.84
26	Pt_1CeO_2-VC@NF-100	337.33
27	Ir_1CeO_2-VC@NF-20	393.05
28	Ir_1CeO_2-VC@NF-40	362.29
29	Ir_1CeO_2-VC@NF-60	349.92

30	Ir_1CeO_2-VC@NF-80	343.83
31	Ir_1CeO_2-VC@NF-100	349.65
32	Fe_1@NF-40	322.22
33	Pt_1@NF-40	-
34	Fe_1-VC@NF-20	319.14
35	Fe_1-VC@NF-40	-
36	Fe_1-VC@NF-60	312.69
37	Pt_1-VC@NF-20	358.84
38	Pt_1-VC@NF-40	353.33
39	Pt_1-VC@NF-60	374.58
40	Pt_1-VC@NF-80	-
41	Cu_1-VC@NF-100	471.04
42	Co_1-VC@NF-100	451.35
43	Ni_1-VC@NF-100	439.31
44	Au_1-VC@NF-100	411.26
45	Ir_1-VC@NF-100	386.98
46	Ru_1-VC@NF-100	417.83
47	In_1-VC@NF-100	414.42
48	Mn_1-VC@NF-100	473.18
49	Zn_1-VC@NF-100	464.88
50	Mo_1-VC@NF-100	408.49
51	V_1-VC@NF-100	420.53
52	Sn_1-VC@NF-100	432.89
53	Ce_1-VC@NF-100	460.51
54	Yb_1-VC@NF-100	408.52
55	La_1-VC@NF-100	426.69
56	Ta_1-VC@NF-100	420.59
57	Fe_1-VC-2h@NF-20	318.54
58	Fe_1-VC-2h@NF-40	321.98
59	Co_1-VC-2h@NF-20	392.86
60	Co_1-VC-2h@NF-40	389.69
61	Pt_1-VC-2h@NF-20	392.84
62	Pt_1-VC-2h@NF-40	393.09
63	Ru_1-VC-2h@NF-20	355.85
64	Ru_1-VC-2h@NF-40	365.11
65	Ir_1-VC-2h@NF-20	343.28
66	Ir_1-VC-2h@NF-40	330.87

Table S7. Comparison of overpotentials at 100 mA cm^{-2} for UOR catalysts screened from the clicking single-atom library. This table summarizes the UOR catalyst samples tested using an automated robotic system. The numerical suffix following each sample identifier indicates the volume (in μL) of a 50 mM precursor solution in ethanol deposited onto the support surface by the *Opentrons Flex* workstation. Using the fully automated robotic evaluation system, the Ni_1CeO_2-VC@NF-40 sample, screened from a total of 44 candidates, demonstrated the best performance. Samples with excessively high overpotentials or failed measurements are marked as "–" in the Potential (mV) column.

Serial number	Catalysts	Potential (V)
1	Fe_1CeO_2-VC@NF-40	1.43
2	Fe_1-2CeO_2-VC@NF-40	1.56
3	Co_1CeO_2-VC@NF-40	1.51
4	Co_1-2CeO_2-VC@NF-40	1.62
5	Ni_1CeO_2-VC@NF-40	1.37
6	Mn_1CeO_2-VC@NF-40	1.48
7	Pt_1CeO_2-VC@NF-40	1.41
8	Ru_1CeO_2-VC@NF-40	1.42
9	$Co_1Mn_1Pt_1Ru_1Ir_1CeO_2$-VC@NF-40	1.42
10	CeO_2-VC@NF-0	1.46
11	CeO_2@NF-0	1.62
12	Fe_1CeO_2@NF-40	1.45
13	Co_1CeO_2@NF-40	1.51
14	Mn_1CeO_2@NF-40	1.50
15	Pt_1CeO_2@NF-40	1.42
16	Ru_1CeO_2@NF-40	1.43
17	Ni_1CeO_2@NF-40	1.44
18	$Ni_1Mo_1CeO_2$@NF-40	1.42
19	$Fe_1Mo_1CeO_2$-VC@NF-40	1.50
20	$Ni_1Co_1CeO_2$-VC@NF-40	1.45
21	$Co_1Mo_1CeO_2$-VC@NF-40	1.55
22	$Ni_1Mo_1CeO_2$-VC@NF-40	-
23	Fe_1@NF-40	1.44
24	Co_1@NF-40	1.47
25	Mn_1@NF-40	1.47
26	Pt_1@NF-40	1.42
27	Ru_1@NF-40	1.43
28	Fe_1-VC@NF-20	-
29	Fe_1-VC@NF-40	-
30	Fe_1-VC@NF-60	1.48

31	Fe_1-VC@NF-80	1.47
32	Fe_1-VC@NF-120	1.49
33	Co_1-VC@NF-20	-
34	Co_1-VC@NF-40	-
35	Co_1-VC@NF-60	-
36	Pt_1-VC@NF-20	1.46
37	Pt_1-VC@NF-40	1.46
38	Pt_1-VC@NF-60	1.43
39	Ru_1-VC@NF-20	1.45
40	Ru_1-VC@NF-40	1.44
41	Ru_1-VC@NF-60	1.43
42	Ir_1-VC@NF-20	1.46
43	Ir_1-VC@NF-40	1.49
44	Ir_1-VC@NF-60	1.42

Table S8. Comparison of overpotentials at 100 mA cm^{-2} for HER catalysts screened from the clicking single-atom library with literature-reported catalysts.

Samples	Overpotential (mV at 100 mA cm^{-2})	Source
Pt_1CeO_2-VC@NF	48.39	This work
Pt@S–NiFe LDH	71	[9]
NiP_2/Ni_5P_4	76	[10]
P-MoO_2@CoNiP	80	[11]
eo-NiRu	88	[12]
$NiCo_2Se_4$ HUNSs/NF	92	[13]
W-$NiS_{0.5}Se_{0.5}$	106	[14]
V_2O_3/Ni/NF	107	[15]
Co_2P-Ni_3S_2/NF	110	[16]
Ru-Pt_{rich}Co NWs	112	[17]
NiSeP@NiCo/Cu	134	[18]
$NiCo_2N$	138	[19]
Pt-NiS@Ni-CNFs-2.5	142	[20]
Ni-$Ni(OH)_2$/NF	158	[21]
NiCoP	159	[22]
$NiCe_{0.05}$/Fe@NM	163	[23]
$Mo_{0.5}$-$NiSe_2$-$CoSe_2$	165	[24]
NiCoP@NiMoSe@NF	167	[25]
CeV-HNA/NF	170	[26]
FeCoNiP/NF	173	[27]
NiFeP@S-$NiFeO_x$/NF	187	[28]
$MnCo_2O_{4.5}$@NiS	187	[29]
cp-Ni_3N	188	[30]
Zn/aCMO	189	[31]
C@CoP-FeP/FF	192	[32]
S-doped Ni-P	196	[33]
Ni foam/CMP-350	197	[34]
(10CeCrP)CoO_x-NF-HER	245	[35]
FMO/NF	263.7	[36]
Ru@B–$Ti_3C_2T_x$	276.9	[37]

Table S9. Comparison of overpotentials at 100 mA cm^{-2} for OER catalysts screened from the clicking single-atom library with literature-reported catalysts.

Samples	Overpotential (mV at 100 mA cm^{-2})	Source
Fe_1CeO_2-VC@NF	306.7	This work
Ni/O-Cat-1/Ni	310	[38]
A-NiFeV/NF	313	[39]
g-C_3N_4-$CuCo_2O_4$	315	[40]
Cr-Ni_3N/NF-0.10	316	[41]
Mo-CoMOF@NF	324	[42]
Ni-Fe-Ce-P/CC	331	[43]
Co_2P-Ni_3S_2/NF	331.7	[16]
Ru/Ni_3Se_4/$Ni(OH)_2$/NF	334.5	[44]
$Ni_{0.2}Co_{2.8}O_4$/MWCNTs	340	[45]
NF/g-C_3N_4/NiFe-OH	342	[46]
3D Mo-NiCoP/NF	344	[47]
V/*meso*-Co/NF-5	344	[48]
N, P-Ni/Mo-TEC@NF	345	[49]
V_o-CuO(In)	350	[50]
Co_3Mo/Mo_2C@NC	355	[51]
Co/$Co_2Mo_3O_8$/NF	360	[52]
B-MOF-Zn-Co	362	[53]
$Ru_{0.27}Co_{2.73}O_4$	367	[54]
CoAl-LDH/rGO	368	[55]
2D-NGT_v	370	[56]
BP-Co/CNT@NC-2	370	[57]
Co_4S_3/Fe_3S_4	380	[58]
NiOOH–MnOOH/NF	391	[59]
$CoMoO_4$/GPLC	399	[60]
Co/Co_4N@NC	408	[61]
$Cr_{1.5}Co_{1.5}O_4$	413	[62]
$SrTi_{0.88}Mn_{0.12}O_3$	445	[63]
Ni-Mn-Co-Fe	447	[64]
P-Co_3O_4/Co_9S_8	450	[65]

Table S10. Comparison of potentials at 100 mA cm^{-2} for UOR catalysts screened from the clicking single-atom library with literature-reported catalysts.

Samples	Potential (mV at 100 mA cm^{-2})	Source
Ni_1CeO_2-VC@NF	1.37	This work
NiCoCr-LDH/NF	1.38	[66]
Ni-MoO_x/NF-3	1.38	[67]
Ir-NiFe-OH	1.38	[68]
P-MoO_2@CoNiP	1.38	[11]
Ce–Ni_3S_2/NF	1.39	[69]
Fe-Ni_2P/$NiSe_2$-12	1.39	[70]
N-C@CoN	1.39	[71]
V-Ni_3S_2	1.39	[72]
NiO/CuO@CuM	1.39	[73]
M/CM/Ni_3S_2/NF	1.392	[74]
Ni_3S_2/VS_2	1.396	[75]
S_v-CoNiS@NF	1.397	[76]
ZnCoFeS–LDH	1.398	[77]
NiB_x/NF	1.4	[78]
$(Ni_4Zn)_{0.8}$/NF	1.4	[79]
Cu_3P	1.4	[80]
Co-NiSMoO/NF	1.401	[81]
$V_{0.10}Ni_{0.90}O$@NF	1.418	[82]
Pt–$Ni(OH)_2$@Ni-CNFs	1.422	[83]
Mn-NiOOH	1.426	[84]
CFRO-7	1.43	[85]
Zr–MnS/Ni_3S_2@NF	1.43	[86]
NiFe-LDH/$NiMoO_4$/NF	1.45	[87]
$NiCoV_{1.0}$-LDH/NF-100	1.46	[88]
$Ni_{0.2}Mo_{0.8}N$/CeO_2-0.3/NF	1.462	[89]
SyA-Cu/CuO/NF	1.47	[90]
α-$Ni(OH)_2$–PNF-2	1.477	[91]
Ni-Te/NF	1.503	[92]
a-FeCoO	1.52	[93]

Table S11. EXAFS fitting parameters at the Cu K-edge for various samples.

Sample	Shell	*CN*[a]	*R*(Å)[b]	σ^2(Å^2)[c]	ΔE_0(eV)[d]	*R* factor
Cu foil	Cu-Cu	12*	2.54±0.02	0.0086	3.6	0.0020
Cu_2O	Cu-O	1.6±0.2	1.85±0.01	0.0023	6.7	0.0164
	Cu-O-Cu	19.2±3.7	3.05±0.01	0.0272	9.0	
CuO	Cu-O	4.0±0.4	1.95±0.01	0.0037	6.7	0.0145
	Cu-O-Cu1	1.7±0.8	2.87±0.01	0.0047	-2.6	
	Cu-O-Cu2	3.4±2.1	3.40±0.01	0.0071	-4.2	
Cu-doped CeO_2	Cu-O	4±0.3	1.91±0.01	0.0089	3.1	0.0115
	Cu-O-Cu	3.8±2.1	3.40±0.01	0.0067	-4.0	
Cu_1/CeO_2-(111)-L	Cu-O	3.0±0.6	2.01±0.01	0.0080	9.2	0.0172

[a]*CN*, coordination number; [b]*R*, distance between absorber and backscatter atoms; [c]σ^2, Debye-Waller factor to account for both thermal and structural disorders; [d]ΔE_0, inner potential correction; *R* factor indicates the goodness of the fit. S_0^2 was fixed to 0.82, according to the experimental EXAFS fit of Cu foil by fixing CN as the known crystallographic value. A reasonable range of EXAFS fitting parameters: $0.600 < S_0^2 < 1.000$; $CN > 0$; $\sigma^2 > 0$ Å^2; $|\Delta E_0| < 15$ eV; *R* factor < 0.02.

Table S12. Composition of C_4 fractions from Fushun Petrochemical Olefin Plant (weight percent, %). The feedstock primarily comprises olefins, including trans-butene, cis-butene, isobutene, and 1-butene.

Component	Content (%)
Isobutane	10.325
n-Butane	45.100
trans-Butene	22.178
1-Butene	14.249
Isobutene	3.466
cis-Butene	4.666
Butadiene	0.026

Supplementary References

1 Guinée, J. Handbook on life cycle assessment - Operational guide to the ISO standards. *Int. J. Life Cycle Assess.* **6**, 255-255 (2001).

2 f., S. I. O. Environmental management: life cycle assessment; requirements and guidelines. *ISO*.

3 Fivga, A. & Dimitriou, I. Pyrolysis of plastic waste for production of heavy fuel substitute: A techno-economic assessment. *Energy* **149**, 865-874 (2018).

4 Seider, W. D. *et al.* Product and process design principles: Synthesis, analysis and evaluation. *Wiley.com.*

5 Towler, G. & Sinnott, R. Chemical engineering design : Principles, practice, and economics of plant and process design. *(Mass: Butterworth-Heinemann, 2021)*.

6 Liu, C. *et al.* Fluorinated polyimide tunneling layer for efficient and stable perovskite photovoltaics. *Angew. Chem. Int. Ed.* **63**, e202402904 (2024).

7 Miao, K. H. *et al.* Phosphorus coordination in second shell of single-atom Cu catalyst toward acetate production in CO electroreduction. *Nano Lett.* **24**, 12849-12856 (2024).

8 Qin, J. D., Hu, X., Miao, K. H. & Kang, X. W. Oxygen coordinated Cu single atom catalysts: a superior catalyst towards electrochemical CO_2 reduction for methane production. *Microstructures* **5**, 13 (2025).

9 Lei, H., Wan, Q., Tan, S., Wang, Z. & Mai, W. Pt-quantum-dot-modified sulfur-doped NiFe layered double hydroxide for high-current-density alkaline water splitting at industrial temperature. *Adv. Mater.* **35**, 2208209 (2023).

10 zhou, q. *et al.* Engineering in-plane nickel phosphide heterointerfaces with interfacial sp H-P hybridization for highly efficient and durable hydrogen evolution at 2 A cm^{-2}. *Small* **18**, 2105642 (2022).

11 Yang, X. *et al.* Boosting urea-assisted water splitting over P-MoO_2@CoNiP through Mo leaching/reabsorption coupling CoNiP reconstruction. *J. Colloid Interface Sci.* **676**, 445-458 (2024).

12 Zhu, Y. a., Yao, J., Lu, T. & Pan, Y. In-situ constructing self-supported NiO/RuO_2 heterostructure for reinforced alkaline hydrogen evolution reaction. *J. Colloid Interface Sci.* **633**, 32-42 (2023).

13 Chen, H. *et al.* Hierarchical $NiCo_2Se_4$ arrays composed of atomically thin nanosheets: Simultaneous improvements in thermodynamics and kinetics for electrocatalytic water splitting in neutral media. *Adv. Sci.* **11**, 2402889 (2024).

14 Wang, Y. *et al.* Highly active and durable single-atom tungsten-doped $NiS_{0.5}Se_{0.5}$ nanosheet @ $NiS_{0.5}Se_{0.5}$ nanorod heterostructures for water splitting. *Adv. Mater.* **34**, 2107053 (2022).

15 Zhang, Q. *et al.* Maximized Schottky Effect: The ultrafine V_2O_3/Ni heterojunctions repeatedly arranging on monolayer nanosheets for efficient and stable water-to-hydrogen conversion. *Small* **17**, 2005769 (2021).

16 Li, H., Gao, X. & Li, G. Construction of Co_2P-Ni_3S_2/NF heterogeneous structural hollow nanowires as bifunctional electrocatalysts for efficient overall water splitting. *Small* **19**, 2304081 (2023).

17 Cao, X. *et al.* Modulating electronic structure of PtCo-ptrich nanowires with Ru atoms for boosted hydrogen evolution catalysis. *Small* **19**, 2302639 (2023).

18 Akbari Kenari, M., Sabour Rouhaghdam, A. & Barati Darband, G. Engineering superhydrophilic Ni-Se-P on Ni-Co nanosheets-nanocones arrays for enhanced hydrogen production assisted by hydrazine oxidation reaction. *J. Colloid Interface Sci.* **678**, 828-841

(2025).
19 Jiang, K. *et al.* Nickel-cobalt nitride nanoneedle supported on nickel foam as an efficient electrocatalyst for hydrogen generation from ammonia electrolysis. *Electrochim. Acta* **403**, 139700 (2022).
20 Zhong, M. *et al.* Significantly enhanced energy-saving H_2 production coupled with urea oxidation by low- and non-Pt anchored on NiS-based conductive nanofibers. *Small* **20**, 2304782 (2024).
21 Cheng, Y. *et al.* Accelerated water dissociation kinetics by nickel-nickelous hydroxide epitaxial interfaces for superior alkaline hydrogen generation. *J. Colloid Interface Sci.* **679**, 600-608 (2025).
22 Ding, X., Pei, L., Huang, Y., Chen, D. & Xie, Z. Hollow NiCoP nanoprisms derived from prussian blue analogues as bifunctional electrocatalysts for urea-assisted hydrogen production in alkaline media. *Small* **18**, 2205547 (2022).
23 Yaseen, W. *et al.* Anchoring $Ni(OH)_2$-CeO_x heterostructure on FeOOH-modified nickel-mesh for efficient alkaline water-splitting performance with improved stability under quasi-industrial conditions. *Small* **20**, 2403971 (2024).
24 Liu, H. *et al.* Interface and electronic structure regulation of Mo-doped $NiSe_2$-$CoSe_2$ heterostructure aerogel for efficient overall water splitting. *J. Colloid Interface Sci.* **640**, 1040-1051 (2023).
25 Feng, S., Liu, Q., Chen, T., Yang, S. & Shang, X. Simple fabrication of amorphous nanocomposite NiCoP@NiMoSe@NF nanospheres as a binder-free and high-performance electrocatalyst for alkaline hydrogen evolution reaction. *Surf. Interfaces* **42**, 103198 (2023).
26 Qin, Y. *et al.* Multiple-perspective design of hollow-structured cerium-vanadium-based nanopillar arrays for enhanced overall water electrolysis. *J. Colloid Interface Sci.* **674**, 1092-1102 (2024).
27 Sheng, W. *et al.* Dual-doped medium-entropy phosphides for complete urea electrolysis. *J. Colloid Interface Sci.* **678**, 1192-1202 (2025).
28 Xu, H. *et al.* Strain effects and crystalline-amorphous interface of NiFe-LDH@S-$NiFeO_x$/NF with heterogeneous structure for enhancing electrocatalytic oxygen evolution reaction of water-electrolysis. *Small* **21**, 2406071 (2024).
29 Zhu, X. *et al.* Vacancy-rich heterogeneous $MnCo_2O_{4.5}$@NiS electrocatalyst for highly efficient overall water splitting. *J. Colloid Interface Sci.* **678**, 878-884 (2025).
30 Ouyang, B. *et al.* Facet control of nickel nitride nano-framework for efficient hydrogen evolution electrocatalysis via auxiliary cooling assisted plasma engineering. *Small* **18**, 2204634 (2022).
31 Wang, M. *et al.* Heteroatom-doped amorphous cobalt–molybdenum oxides as a promising catalyst for robust hydrogen evolution. *Inorg. Chem.* **61**, 5033-5039 (2022).
32 Li, J., Hu, Y., Huang, X., Zhu, Y. & Wang, D. Bimetallic phosphide heterostructure coupled with ultrathin carbon layer boosting overall alkaline water and seawater splitting. *Small* **19**, 2206533 (2023).
33 Ashraf, M. A., Yang, Y., Zhang, D. & Pham, B. T. Bifunctional and binder-free S-doped Ni-P nanospheres electrocatalyst fabricated by pulse electrochemical deposition method for overall water splitting. *J. Colloid Interface Sci.* **577**, 265-278 (2020).
34 Zhao, S. *et al.* The role of phosphate group in doped cobalt molybdate: Improved electrocatalytic hydrogen evolution performance. *Adv. Sci.* **7**, 1903674 (2020).
35 Feng, J. *et al.* Nanocrystalline CoO_x glass for highly-efficient alkaline hydrogen evolution

reaction. *J. Mater. Chem. A* **11**, 316-329 (2022).
36 Sun, A., Qiu, Y., Zheng, X., Cui, L. & Liu, J. Construction of micro-nano hierarchical wing-like iron/molybdenum oxide heterojunction with synergistic effect for accelerated overall water splitting. *J. Colloid Interface Sci.* **632**, 108-116 (2023).
37 Bat-Erdene, M. *et al.* Highly dispersed Ru nanoparticles on boron-doped Ti_3C_2T (MXene) nanosheets for synergistic enhancement of electrocatalytic hydrogen evolution. *Small* **17**, 2102218 (2021).
38 Hou, Z. *et al.* Self-generated oxygen radical species accelerate the alkaline oxygen-evolving reaction. *Int. J. Hydrogen Energy* **71**, 196-204 (2024).
39 Yang, H. *et al.* Synergistic engineering of heteroatom doping and heterointerface construction in V-doped $Ni(OH)_2$/FeOOH to boost both oxygen evolution and urea oxidation reactions. *J. Colloid Interface Sci.* **653**, 721-729 (2024).
40 Jeghan, S. M. N. *et al.* Exfoliated defects-rich g-C_3N_4 nanosheets heterointerface engineering with $CuCo_2O_4$ as promising bifunctional electrocatalysts for seawater splitting. *Chem. Eng. J.* **487**, 150576 (2024).
41 Liao, X. *et al.* Cr-doping promoted surface reconstruction of NiN electrocatalysts toward efficient overall water splitting. *J. Colloid Interface Sci.* **674**, 1048-1057 (2024).
42 Sun, N. *et al.* Active site customizing of metal–organic materials for highly efficient oxygen evolution. *Small* **21**, 2407933
43 Zhao, H.-R. *et al.* Balancing electron transfer and intermediate adsorption ability of metallic Ni-Fe-RE-P bifunctional catalysts via 4*f*-2*p*-3*d* electron interaction for enhanced water splitting. *J. Energy Chem.* **94**, 458-465 (2024).
44 Guo, X. *et al.* Ru nanoparticles modified Ni_3Se_4/$Ni(OH)_2$ heterostructure nanosheets: A fast kinetics boosted bifunctional overall water splitting electrocatalyst. *J. Colloid Interface Sci.* **663**, 847-855 (2024).
45 Sabahat, S. *et al.* Exploration of anode candidacy of $Ni_{0.2}Co_{2.8}O_4$ and integrated $Ni_{0.2}Co_{2.8}O_4$/MWCNTs in supercapacitor and oxygen evolution reaction. *Heliyon* **10**, e24214 (2024).
46 Zhu, H. *et al.* Ultrathin graphitic carbon nitride interface layer regulated nickel-iron oxyhydroxide stabilized on nickel foam for efficient oxygen evolution reaction. *Colloids Surf., A* **688**, 133614 (2024).
47 Wang, F., Zhang, K., Zha, Q. & Ni, Y. Honeycomb-like Ni-Mo-S on Ni foam as superior bifunctional electrocatalyst for hydrogen evolution and urea oxidation. *J. Alloys Compd.* **899**, 163346 (2022).
48 Amer, M. S., Arunachalam, P., Al-Mayouf, A. M., AlSaleh, A. A. & Almutairi, Z. A. Bifunctional vanadium doped mesoporous Co_3O_4 on nickel foam towards highly efficient overall urea and water splitting in the alkaline electrolyte. *Environ. Res.* **236**, 116818 (2023).
49 Zuo, P. *et al.* N, P co-doped Ni/Mo-based multicomponent electrocatalysts in situ decorated on Ni foam for overall water splitting. *J. Colloid Interface Sci.* **645**, 895-905 (2023).
50 Bi, M., Guo, Z., He, H., Liu, Z. & Liu, Z. Vo-CuO(In) with super-hydrophilicity exhibits efficient electrocatalytic activity in alkaline media: Synergistic effect of In doping and oxygen vacancies. *Int. J. Hydrogen Energy* **59**, 507-515 (2024).
51 Wang, X.-L., Sun, L., Yang, L., Zhao, J. & Xu, Q. Hybrid zeolitic imidazolate framework-derived Co_3Mo/Mo_2C heterostructure for enhanced oxygen evolution reaction. *Adv. Funct. Mater.* **34**, 2314247 (2024).

52 Zhang, X. *et al.* Construction of heterogeneous interfaces for water activation and dissociation to synergistically boost overall water splitting. *J. Colloid Interface Sci.* **665**, 518-525 (2024).
53 Lin, X. *et al.* In situ electrochemical restructuring b-doped metal–organic frameworks as efficient OER electrocatalysts for stable anion exchange membrane water electrolysis. *Small* **20**, 2308517 (2024).
54 Wang, G., Zhang, G. & Chen, X. Ru single atoms integrated into cobalt oxide spinel structure with interstitial carbon for enhanced electrocatalytic water oxidation. *Small* **20**, 2310372 (2024).
55 Zhang, D. *et al.* Air-condition process for Constructing MeAl-LDHs/rGO (Me = Co, Ni, Fe) hybrids toward efficient oxygene evolution reaction. *J. Colloid Interface Sci.* **679**, 680-690 (2025).
56 Bo, G. *et al.* 2D Ferromagnetic M_3GeTe_2 (M = Ni/Fe) for boosting intermediates adsorption toward faster water oxidation. *Adv. Sci.* **11**, 2310115 (2024).
57 Han, D. *et al.* Three-dimensional carbon network-supported black phosphorus-cobalt heterojunctions: An efficient electrocatalyst for high-rate oxygen evolution. *J. Colloid Interface Sci.* **651**, 415-423 (2023).
58 Jin, S. *et al.* FeCo-MOF derived $Co_4S_3/Fe_3S_4/MoS_2$ nanosheet arrays on iron foam for overall water splitting in alkaline water /seawater at large-current density. *Int. J. Hydrogen Energy* **61**, 329-340 (2024).
59 Zhou, Y. *et al.* Boosting alkaline water splitting efficiency: NiOOH–MnOOH heterojunctions via in situ anodic oxidation. *Mater. Chem. Front.* **8**, 3290-3299 (2024).
60 Wang, B. *et al.* Biomass-derived-carbon-supported spinel cobalt molybdate as high-efficiency electrocatalyst for oxygen evolution reaction. *Molecules* **29**, 4953 (2024).
61 Choi, H. W. *et al.* Tracking accelerated oxygen evolution reaction enabled by explosive reconstruction of active species based on Co_xN@NC. *J. Mater. Chem. A* **12**, 7067-7079 (2024).
62 Mishra, P., Parihar, R., Singh, Y., Chaddha, A. S. & Singh, N. K. Finely tuning cobalt valence in Co_3O_4 lattice through chromium substitution: Regulating the charge transfer and oxygen vacancies for oxygen evolution and methanol oxidation reaction. *Mater. Today Sustainability* **27**, 100826 (2024).
63 Mylsamy, S., Karazhanov, S. & Subramanian, B. Lattice distortion-driven band gap engineering and enhanced electrocatalytic activity of Mn-substituted nanostructured $SrTiO_3$ materials: A comprehensive investigation. *Chemosphere* **346**, 140577 (2024).
64 Belhani, I. *et al.* Enhanced electrocatalytic activity of Ni-Mn-Co-Fe alloys for efficient hydrogen and oxygen evolution reactions: A study on the effects of electrodeposition parameters. *Renewable Energy* **237**, 121688 (2024).
65 Qiu, A. & Yu, Y. Phosphorus-doped cobalt oxide/cobalt sulfide heterostructure for enhanced oxygen evolution. *J. Alloys Compd.* **1002**, 175330 (2024).
66 Xu, S. *et al.* O-2p Hybridization Enhanced Transformation of Active γ-NiOOH by Chromium Doping for Efficient Urea Oxidation Reaction. *Adv. Funct. Mater.* **34** (2024).
67 Li, Z. *et al.* Synthesis of Ni decorated MoO_x nanorod catalysts for efficient overall urea–water splitting. *J. Chem. Phys.* **160**, 214703 (2024).
68 Chen, X. *et al.* Nickel-iron in the second coordination shell boost single-atomic-site iridium catalysts for high-performance urea electrooxidation. *Nano Res.* **17**, 3919-3926 (2024).
69 Zheng, W. *et al.* 4f–2p–3d Orbital coupling in Ce–Ni_3S_2 enhancing the urea oxidation

reaction. *Inorg. Chem.* **63**, 14602-14608 (2024).
70 Huang, C.-J. *et al.* Fe-Doped $Ni_2P/NiSe_2$ Composite catalysts for urea oxidation reaction (UOR) for energy-saving hydrogen production by UOR-assisted water splitting. *Inorg. Chem.* **63**, 8925-8937 (2024).
71 Tang, T. *et al.* One-step constructing advanced N-doped carbon@metal nitride as ultra-stable electrocatalysts *via* urea plasma under room temperature. *Chin. Chem. Lett.* **35**, 109887 (2024).
72 Sharma, P. J. *et al.* Vanadium-doped Ni_3S_2: Morphological evolution for enhanced industrial-scale water and urea electrolysis. *ChemSusChem* (2024).
73 Yang, L. *et al.* Self-supported NiO/CuO electrodes to boost urea oxidation in direct urea fuel cells. *Nano Energy* **115**, 108714 (2023).
74 Wang, H. *et al.* Nickel-constructing interfaces of multiheterostructure on self-supporting electrode for efficient overall urea-water splitting. *Appl. Surf. Sci.* **640**, 158288 (2023).
75 Huang, Y. *et al.* Hierarchical superhydrophilic/superaerophobic Ni_3S_2/VS_2 nanorod-based bifunctional electrocatalyst supported on nickel foam for overall urea electrolysis. *Inorg. Chem.* **63**, 19002-19010 (2024).
76 Li, H. *et al.* Sulfur-vacancy engineering accelerates rapid surface reconstruction in Ni-Co bimetal sulfide nanosheet for urea oxidation electrocatalysis. *Small* **20** (2024).
77 Li, R. *et al.* Morphological and electronic regulation of Zn,S-incorporated FeCo–LDH nanosheets for boosting the bi-electrocatalytic oxygen evolution and urea oxidation reactions. *ACS Sustainable Chem. Eng.* **11**, 16098-16107 (2023).
78 Hu, Y. *et al.* Unveiling the role of boron on nickel-based catalyst for efficient urea oxidation assisted hydrogen production. *Adv. Funct. Mater.* **34**, 2411011 (2024).
79 Li, H., Wang, S., Zhu, Q., Li, S. & Ni, Y. Freestanding $(Ni_4Zn)_{0.8}$ intermetallic nanosheets as bifunctional electrocatalysts for urea-assisted hydrogen production. *ACS Appl. Nano Mater.* **7**, 18861-18869 (2024).
80 Bandal, H. A. & Kim, H. In situ formed $Cu_3P@CuO_x$ as an efficient electrocatalyst for urea electrooxidation. *Appl. Surf. Sci.* **622**, 156925 (2023).
81 Lin, J. *et al.* Compositional and electronic reconstruction to co-incorporated $NiOSO_4$–$NiMoO_4$ for boosting electrocatalytic overall water splitting/overall urea splitting reactions. *J. Colloid Interface Sci.* **678**, 470-479 (2025).
82 Sharma, P. J. *et al.* Enhanced water and urea electrolysis at industrial scale current density using self-supported $V_xNi_{1-x}O$ trifunctional catalysts. *Int. J. Hydrogen Energy* **85**, 374-384 (2024).
83 Zhong, M. *et al.* Modulating the electronic structure of $Ni(OH)_2$ by coupling with low-content Pt for boosting the urea oxidation reaction enables significantly promoted energy-saving hydrogen production. *Energy Environ. Sci.* **17**, 1984-1996 (2024).
84 Duan, N. *et al.* Insight into the structure of Mn-NiS_2 during urea oxidation using combined in situ X-ray absorption spectroscopy and attenuated total reflectance surface-enhanced infrared absorption spectroscopy. *ACS Catal.* **14**, 1384-1393 (2024).
85 Liu, C. *et al.* Asymmetric configuration activating lattice oxygen via weakening *d-p* orbital hybridization for efficient C/N separation in urea overall electrolysis. *J. Energy Chem.* **92**, 233-239 (2024).
86 Zhao, Z., Zhao, H., Du, X. & Zhang, X. Controlled synthesis of M-MnS/Ni_3S_2（M=Zr, Ce, Bi and V）nanoarrays on nickel foam for overall urea splitting. *Int. J. Hydrogen Energy* **88**, 313-321 (2024).

87 Qiao, S. *et al.* Enhanced hydrogen production via catalytic water and urea oxidation in a hybrid acid-base electrolytic cell with NiFe-LDH/$NiMoO_4$/NF. *J. Alloys Compd.* **1004**, 175823 (2024).
88 Guo, J., Zhang, H., Yang, Y., Wei, M. & Zhang, H. V-Doping coupled H_2O_2 pre-oxidation synergistically promote NiCo-LDH for urea oxidation-assisted hydrogen production. *J. Mater. Chem. A* **12**, 16780-16792 (2024).
89 Meng, L., Zhang, L., Liu, S., Wang, F. & Wu, H. $Mo_{0.2}Ni_{0.8}N/CeO_2$ heterojunction as bifunctional electrocatalysts for overall urea-water electrolysis. *Int. J. Hydrogen Energy* **48**, 33383-33392 (2023).
90 Xu, G. *et al.* In situ electrochemical oxidation synthesis of SyA-Cu/CuO/NF heterostructure as trifunctional electrocatalyst for UOR, BOR, and HER at industrial-scale high current density. *Energy & Fuels* **38**, 19748-19757 (2024).
91 Li, Y. *et al.* Oxygen vacancies in α-$Ni(OH)_2$ porous nanoflowers promote urea oxidation. *Int. J. Hydrogen Energy* **48**, 9155-9162 (2023).
92 Yuan, S. *et al.* Defects engineering of nickel tellurium electrocatalyst to boost urea oxidation reaction: Electrodeposition mechanism and performance. *J. Alloys Compd.* **997**, 174944 (2024).
93 Wei, T. *et al.* Amorphous Fe–Co oxide as an active and durable bifunctional catalyst for the urea-assisted H_2 evolution reaction in seawater. *Chem. Commun.* **59**, 9992-9995 (2023).